

Electromagnetics in Biomedical Applications

Guest Editors: Soon Yim Tan, Andrea Borsic, Panagiotis Kosmas,
and Yifan Chen





Electromagnetics in Biomedical Applications

International Journal of Antennas and Propagation

Electromagnetics in Biomedical Applications

Guest Editors: Joon Yim Tan, Andrea Borsic,
Panagiotis Kosmas, and Yifan Chen



Copyright © 2014 Hindawi Publishing Corporation. All rights reserved.

This is a special issue published in "International Journal of Antennas and Propagation." All articles are open access articles distributed under the Creative Commons Attribution License, which permits unrestricted use, distribution, and reproduction in any medium, provided the original work is properly cited.

Editorial Board

M. Ali, USA
Charles Bunting, USA
Felipe Cátedra, Spain
Dau-Chyrh Chang, Taiwan
Deb Chatterjee, USA
Z. N. Chen, Singapore
Michael Yan Wah Chia, Singapore
Shyh-Jong Chung, Taiwan
Lorenzo Crocco, Italy
Tayeb A. Denidni, Canada
Antonije R. Djordjevic, Serbia
Karu P. Esselle, Australia
Francisco Falcone, Spain
Miguel Ferrando, Spain
Vincenzo Galdi, Italy
Wei Hong, China
Hon Tat Hui, Singapore
Tamer S. Ibrahim, USA
Mandeep Singh Jit Singh, Malaysia
Nemai Karmakar, Australia

Se-Yun Kim, Republic of Korea
Ahmed A. Kishk, Canada
Selvan T. Krishnasamy, India
Tribikram Kundu, USA
Ju-Hong Lee, Taiwan
Byungje Lee, Republic of Korea
L. Li, Singapore
Yilong Lu, Singapore
Atsushi Mase, Japan
Andrea Massa, Italy
Giuseppe Mazzarella, Italy
Derek McNamara, Canada
C. F. Mecklenbräuker, Austria
Michele Midrio, Italy
Mark Mirotznik, USA
Ananda S. Mohan, Australia
P. Mohanan, India
Pavel Nikitin, USA
A. D. Panagopoulos, Greece
Matteo Pastorino, Italy

Massimiliano Pieraccini, Italy
Sadasiva M. Rao, USA
Sembiam R. Rengarajan, USA
Ahmad Safaai-Jazi, USA
Safieddin Safavi-Naeini, Canada
Magdalena Salazar-Palma, Spain
Stefano Selleri, Italy
Zhongxiang Shen, Singapore
John J. Shynk, USA
Seong-Youp Suh, USA
Parveen Wahid, USA
Yuanxun Ethan Wang, USA
Daniel S. Weile, USA
Tat Soon Yeo, Singapore
Young J. Yoon, Republic of Korea
Jong-Won Yu, Republic of Korea
Wenhua Yu, USA
Anping Zhao, China

Contents

Electromagnetics in Biomedical Applications, Soon Yim Tan, Andrea Borsic, Panagiotis Kosmas, and Yifan Chen
Volume 2014, Article ID 613409, 1 page

Differential Microwave Imaging for Brain Stroke Followup, R. Scapatucci, O. M. Bucci, I. Catapano, and L. Crocco
Volume 2014, Article ID 312528, 11 pages

Evaluation of the Electromagnetic Power Absorption in Humans Exposed to Plane Waves: The Effect of Breathing Activity, Marta Cavagnaro, Erika Pittella, and Stefano Pisa
Volume 2013, Article ID 854901, 7 pages

Analysis and Design of Magnetic Shielding System for Breast Cancer Treatment with Hyperthermia Inductive Heating, Chanchai Thongsopa and Thanaset Thosdeekoraphat
Volume 2013, Article ID 163905, 12 pages

Dual-Band On-Body Repeater Antenna for In-on-On WBAN Applications, Jinpil Tak, Kyeol Kwon, Sunwoo Kim, and Jaehoon Choi
Volume 2013, Article ID 107251, 12 pages

Electric Field Measurement of the Living Human Body for Biomedical Applications: Phase Measurement of the Electric Field Intensity, Ichiro Hieda and Ki Chang Nam
Volume 2013, Article ID 305362, 6 pages

A Feasibility Study for Microwave Breast Cancer Detection Using Contrast-Agent-Loaded Bacterial Microbots, Yifan Chen, Panagiotis Kosmas, and Sylvain Martel
Volume 2013, Article ID 309703, 11 pages

Editorial

Electromagnetics in Biomedical Applications

Soon Yim Tan,¹ Andrea Borsic,² Panagiotis Kosmas,³ and Yifan Chen⁴

¹ *Division of Communication Engineering, School of Electrical and Electronic Engineering, Nanyang Technological University, Singapore 639798*

² *Thayer School of Engineering at Dartmouth, 800 Cummings Hall, Hanover, NH 03755, USA*

³ *School of Natural and Mathematical Sciences, King's College London, Strand, London WC2R 2LS, UK*

⁴ *South University of Science and Technology of China, 1088 Tangchang Road, Nanshan District, Shenzhen, Guangdong 518055, China*

Correspondence should be addressed to Soon Yim Tan; esytan@ntu.edu.sg

Received 2 January 2014; Accepted 2 January 2014; Published 4 February 2014

Copyright © 2014 Soon Yim Tan et al. This is an open access article distributed under the Creative Commons Attribution License, which permits unrestricted use, distribution, and reproduction in any medium, provided the original work is properly cited.

Advance research in electromagnetic theory has been a fundamental key driver to push the frontier of biomedical technology. These studies include evaluation of health hazards of microwave field emission by ubiquitous wireless communication systems, interaction of electromagnetic waves with biological tissues and living systems, and also the therapeutic, diagnostic, and imaging applications of electromagnetic. Cancer detection using ultra-wideband signal, hyperthermia of tumours, healthcare informatics, and wireless bioimplants are some for the research topics using electromagnetic waves. Out of the accepted papers of this special issue, four papers will be highlighted below.

“*Electric field measurement of the living human body for biomedical applications: phase measurement of the electric field intensity*” by I. Hieda and K. C. Nam illustrates a technique for conducting measurements inside the human body by applying a weak electric field at a radio frequency (RF). The method is simple, safe, cost-effective, and able to be used for biomedical applications.

Y. Chen et al. present “*A feasibility study for microwave breast cancer detection using contrast-agent-loaded bacterial microbots*.” The authors proposed a novel differential microwave imaging technique to simultaneously track multiple swarms of magnetotactic bacteria microbots that are injected into the breast to detect breast tumours.

“*Analysis and design of magnetic shielding system for breast cancer treatment with hyperthermia inductive heating*” by C. Thongsopa and T. Thosdeekoraphat provides an analysis and design of rectangular magnetic shielding aperture system for breast cancer treatment with hyperthermia inductive heating.

J. Tak et al. present “*Dual-band on-body repeater antenna for in-on-on WBAN applications*.” This paper investigates an antenna for in-on-on wireless body area network applications, which was designed to communicate with implanted devices in the 5.8 GHz ISM band and to transmit the biological information received from the implanted devices to other on-body devices in the 2.45 GHz ISM band.

Soon Yim Tan
Andrea Borsic
Panagiotis Kosmas
Yifan Chen

Research Article

Differential Microwave Imaging for Brain Stroke Followup

R. Scapaticci,^{1,2} O. M. Bucci,^{1,3} I. Catapano,¹ and L. Crocco¹

¹ IREA, National Research Council of Italy, Via Diocleziano 328, 80124 Napoli, Italy

² DIIES, University Mediterranea of Reggio Calabria, Via Graziella, Loc. Feo di Vito, 89124 Reggio Calabria, Italy

³ DIETI, Federico II University of Naples, Via Claudio 21, 80125 Napoli, Italy

Correspondence should be addressed to L. Crocco; crocco.l@irea.cnr.it

Received 2 July 2013; Revised 15 November 2013; Accepted 27 November 2013; Published 2 January 2014

Academic Editor: Andrea Borsic

Copyright © 2014 R. Scapaticci et al. This is an open access article distributed under the Creative Commons Attribution License, which permits unrestricted use, distribution, and reproduction in any medium, provided the original work is properly cited.

This paper deals with the possibility of adopting microwave imaging to continuously monitor a patient after the onset of a brain stroke, with the aim to follow the evolution of the disease, promptly counteract its uncontrolled growth, and possibly support decisions in the clinical treatment. In such a framework, the assessed techniques for brain stroke diagnosis are indeed not suitable to pursue this goal. Conversely, microwave imaging can provide a diagnostic tool able to follow up the disease's evolution, while relying on a relatively low cost and portable apparatus. The proposed imaging procedure is based on a differential approach which requires the processing of scattered field data measured at different time instants. By means of a numerical analysis dealing with synthetic data generated for realistic anthropomorphic phantoms, we address some crucial issues for the method's effectiveness. In particular, we discuss the role of patient-specific information and the effect of inaccuracies in the measurement procedure, such as an incorrect positioning of the probes between two different examinations. The observed results show that the proposed technique is indeed feasible, even when a simple, nonspecific model of the head is exploited and is robust against the above mentioned inaccuracies.

1. Introduction

A brain stroke occurs when cerebral blood circulation fails as a consequence of a blocked or burst blood vessel, causing an ischemia or a hemorrhage, respectively. Currently, stroke is the second cause of mortality worldwide and a major cause of permanent disability [1]. Moreover, because of the ageing population, such a burden is expected to increase in the future, with a significant, also economical, impact on health-care systems [2]. In such a framework, the most assessed diagnostic tools are magnetic resonance imaging (MRI) and computerized tomography (CT), which provide highly reliable images and indeed play a primary role in stroke management protocols [3].

In the recent years, with the aim to further enhance recovery rate and reduce consequences of strokes, continuous postevent monitoring of physiological parameters in the acute stage has gained an increasing importance [4, 5]. As a matter of fact, recovery and treatment depend on close clinical observation, especially during the first few hours after the onset of stroke [6]. However, CT and MRI cannot contribute to pursue this goal, because they are time

consuming, not portable, and cost-ineffective. Moreover, CT uses ionizing radiations, which are harmful for the patient's health and hence not suitable for continuous monitoring. For these reasons, there is an interest in developing cooperating techniques, capable of overcoming these limitations and increase the effectiveness of medical treatments.

Thanks to the evidence that an electric contrast exists between healthy and stroke tissues [7], microwave imaging (MWI) can be exploited in this framework. In addition, microwaves are nonionizing and the involved instrumentation is relatively low cost and portable if compared to CT or MRI. Hence, MWI devices can be safely adopted for repeated examinations and even deployed at the bed of the patient. Therefore, MWI may represent a valid complementary diagnostic tool for the follow-up stage of brain stroke. However, retrieving the map of the electromagnetic properties of brain tissues from the data gathered by a MWI device requires to tackle a nonlinear and ill-posed inverse scattering problem [8]. As well known, solution procedures for this class of problems are computationally demanding, thus being not suitable to provide the needed real-time or quasi-real-time results. Moreover, they are affected by the occurrence of false

solutions [9], that is, imaging results completely different from the ground truth that impair the reliability of the diagnosis.

The specific nature of the imaging task to be faced in stroke follow-up suggests that the above problems can be overcome. As a matter of fact, the actual target of such a monitoring is the (typically small) variation of the stroke region extent, with respect to the one imaged at the first diagnosis. From the point of view of the MWI processing, this circumstance is indeed a beneficial one, as it entails that the inverse problem to be solved can be well approximated with a linear one, which is free from false solutions and efficiently handled using reliable and assessed inversion strategies.

In this paper, we consider a differential imaging approach for brain stroke followup. In particular, the method provides an estimate of possible variations of the stroke region by processing the difference between monochromatic scattered field data collected at different time instants after stroke diagnosis. In particular, we adopt a Truncated Singular Value Decomposition (TSVD) scheme [10] and, motivated by the encouraging preliminary results [11], we investigate its performance against *a priori* information on the patient under examination and the presence of inaccuracies in the measurement process. As far as the first point is concerned, the aim is to assess the capability of the proposed method of monitoring the disease's evolution with minimal requirements in terms of patient-specific information. As a matter of fact, while such information could be obtained by converting a high resolution MRI or CT image of the patient's head into relative permittivity and conductivity maps, such a translation may be a difficult task, because of the need of coregistering the images and due to the variability of electric properties of human tissues from patient to patient. Moreover, minimizing patient-specific information allows image processing to be carried out in real time. As far as the second point is concerned, we have analyzed the effect of the presence of uncertainties on the measured data as well as of mismatches occurring in the probes positioning between two measurement stages. As a matter of fact, in follow-up applications data are gathered at different time instants and processed assuming that the overall conditions hold unchanged, so that it is important to consider the effect of such inaccuracies.

It is worth recalling that the concept of differential MWI for medical applications is not new in the literature [12, 13], and some example exists also in the case of brain stroke imaging [14, 15]. However, the approach presented herein is the first one that is explicitly meant for stroke followup. In addition, previous papers concerned with MWI for brain monitoring [8, 14, 15] assume the availability of an almost exact, patient-specific knowledge of the actual scenario before the stroke onset, which poses the above mentioned issues. Finally, as far as application of microwaves for brain stroke classification is concerned, the efforts of Fhager and colleagues which aimed at developing a system using microwave signals to discriminate between ischemic or hemorrhagic events are worth to be mentioned [16–18]. As a matter of fact, the kind of system they have developed, even though meant for a purpose different than imaging, is

consistent with the concept we are presenting in this paper, so that it represents in some sense a starting point for the development of a MWI device for brain stroke followup.

The paper is structured as follows. In Section 2, the mathematical background is given and the linear inverse scattering problem at hand is stated. In Section 3, the adopted TSVD inversion procedure is described, with a detail on the role of patient specific information. Section 4 reports a numerical analysis carried out against synthetic data generated for a 2D anthropomorphic head model, concerning the performance of the proposed method against uncertainties on the reference model and on the gathered data. In Section 5, a 3D validation with synthetic data of the overall concept is presented. Conclusions are drawn in Section 6. Throughout the paper a time factor $e^{j\omega t}$ is assumed and omitted.

2. Mathematical Background and Statement of the Problem

Let us suppose that a patient has to be monitored over time after the stroke onset by means of a MWI device. To this end, the scattered field data (encoding the variation with respect to an assumed reference scenario) is measured at different time instants. In particular, the data are collected by means of an array of P antennas located on a surface D surrounding the head and we assume that a single frequency multiview-multistatic measurement configuration is exploited. In such an arrangement, each antenna acts as both transmitter and receiver, and the field induced when the i th antenna is active is recorded at all the P probes positions. Notably, owing to reciprocity, it is not necessary to carry out P^2 measurements, since only $P(P + 1)/2$ are actually independent and therefore needed to build a complete data-set.

The choice of considering single frequency data is motivated by two reasons. First, our previous studies revealed that the useful bandwidth for microwave brain imaging applications is actually narrow [14], suggesting that processing of multifrequency data would not considerably improve the achievable results, as indeed indirectly confirmed by the fact that numerical simulations in [8] use monochromatic data and by the narrow frequency operation of the experimental device designed by Fhager and coworkers [18]. The second not less important motivation is that monochromatic data allows us to avoid the problem of modeling the frequency dependent electric behavior of tissues and to keep the complexity of the experimental apparatus as low as possible, the latter being an important point to speed-up data acquisition and henceforth the overall examination time.

Under the above assumptions, the time-harmonic scattered field measured at the generic time instant t_n by the receivers located in $\mathbf{r}_p \in D$ when the probe in $\mathbf{r}_q \in D$ is radiating can be expressed as

$$\mathbf{E}_s^n(\mathbf{r}_p, \mathbf{r}_q) = \int_{\Omega} \underline{\underline{\mathbf{G}_e}}(\mathbf{r}_p, \mathbf{r}) \cdot \mathbf{E}^n(\mathbf{r}, \mathbf{r}_q) \chi^n(\mathbf{r}) dr, \quad (1)$$

where Ω represents the investigated region, $\underline{\underline{\mathbf{G}_e}}$ represents the Green's function for the assumed reference scenario, and $\mathbf{E}^n(\mathbf{r}, \mathbf{r}_q)$ is the total field in the reference scenario at

the considered time instant. The function $\chi^n(\mathbf{r})$ is the electric contrast and accounts for the variation at the considered time instant of the electric properties of the imaged scenario, with respect to those of the reference one. For instance, assuming that the reference scenario is the healthy brain and that the instant t_n follows the stroke onset, the contrast χ^n represents the stroked area that is the portion of the brain wherein a change in the electric properties has occurred due to the presence of injured tissues.

To express the variation of the stroke region's extent, which is the actual target of followup, let us suppose to have gathered data at two different time instants: at the time of the first diagnosis, say t_0 , and after a certain time, say t_1 . Owing to the linearity of Maxwell's equations, the resulting *differential* field ΔE_s is given by

$$\Delta E_s(\mathbf{r}_p, \mathbf{r}_q) = \int_{\Omega} \left(\underline{\underline{\mathbf{G}_e}}(\mathbf{r}_p, \mathbf{r}) \cdot \mathbf{E}^1(\mathbf{r}, \mathbf{r}_q) \chi^1(\mathbf{r}) - \underline{\underline{\mathbf{G}_e}}(\mathbf{r}_p, \mathbf{r}) \cdot \mathbf{E}^0(\mathbf{r}, \mathbf{r}_q) \chi^0(\mathbf{r}) \right) d\mathbf{r} \quad (2)$$

Such an expression is a quite complex one, since, while the Green's function is the same at both instants (being the reference scenario unchanged), the total fields \mathbf{E}^1 and \mathbf{E}^0 are instead different, due to the fact that they implicitly depend on the contrast. However, in the framework we are considering that the variation between χ^0 and χ^1 can be assumed to be small (and in case of ischemic strokes also characterized by a weak contrast), so that one can reliably assume that the aforementioned changes in the total fields can be neglected. This corresponds to adopt the Distorted Born approximation and rewrite (2) as follows:

$$\begin{aligned} \Delta E_s(\mathbf{r}_p, \mathbf{r}_q) &= \int_{\Omega} \underline{\underline{\mathbf{G}_e}}(\mathbf{r}_p, \mathbf{r}) \cdot \mathbf{E}^0(\mathbf{r}, \mathbf{r}_q) \delta\chi_s(\mathbf{r}) d\mathbf{r} \\ &= \mathbf{L}_e \delta\chi_s, \end{aligned} \quad (3)$$

where assuming that the adopted reference model is the scenario at the first diagnosis, $\delta\chi_s$ expresses the variation of the stroke region with respect to the diagnosed one.

The imaging problem we have to face is hence cast as the reconstruction of the spatial map of $\delta\chi_s$, from the measured differential scattered field ΔE_s . Notably, thanks to the above considerations, this problem is a linear one, since the relationship between the data and the unknowns is expressed through the linear operator $\mathbf{L}_e^0 : \delta\chi_s \in L^2(\Omega) \rightarrow \Delta E_s \in L^2(D)$. This is an important circumstance, as the solution of linear ill-posed inverse problems is free from occurrence of false solutions. On the other hand, the operator \mathbf{L}_e^0 is compact, owing to the properties of its kernel [10]. As such, the imaging task, in order to provide reliable diagnostic results, has to be carried out adopting suitable regularization tools to counteract the ill-posedness.

In doing so, one has also to consider that a quasi-real-time follow-up monitoring is the ultimate goal, in order to promptly detect sudden changes, so that the adopted imaging procedure should rely on fast and simple methods, able to provide reliable images in a possibly short time. This issue is addressed in the next section.

3. Inversion Procedure: Exploiting an Approximated Reference Scenario

According to the formulation of the monitoring problem derived in the previous Section, the imaging problem at hand is cast through a linear and ill-posed inverse problem. As well known, for this class of problems, a reliable and flexible regularized inversion tool is the TSVD scheme [10]. In such noniterative scheme, the sought differential contrast is explicitly estimated through the inversion formula:

$$\delta\chi_s = \sum_{n=1}^N \frac{1}{\sigma_n} \langle \Delta E_s, U_n \rangle V_n, \quad (4)$$

where σ_n , U_n , and V_n denote the singular values and the left and right singular vectors of the linear operator \mathbf{L}_e^0 , respectively. In (4), the truncation index N acts as regularization parameter and its value has to meet the trade-off between stability of the reconstruction (with respect to noise on data and modeling errors arising from the adopted reference scenario) and accuracy of the resulting image (in terms of spatial resolution). If the noise level is known, a suitable value could be obtained by using the Morozov discrepancy principle or the L -curve method [10]. However, since in practice such a knowledge is not available, we set the truncation index to a value which is slightly lower than the one corresponding to the change of slope of the singular value's spectrum (theoretically foreseen by the analytic nature of the operator's kernel). It is also worth to note that, in the clinical problem we are considering that this issue could be less important than that in other contexts. As a matter of fact, when performing the examination, the user knows where the variation is expected to occur, so that she/he can discard possible artifacts arising in other areas of the brain (that may result from setting the threshold beyond the suitable value). Thus, one can think that in practice, thanks to the real time nature of the image formation procedure, the clinical operator can adaptively "fine tune" the threshold value with respect to the one provided by the algorithm.

The reference scenario is required in the inversion to build the kernel of the integral operator (through the Green's function and the corresponding total field). In the ideal case, the inner structure of the head at the time of the first diagnosis would be exploited to this end. Unfortunately, an *exact* knowledge of such a scenario is never available, so that some strategies have to be devised to overcome this drawback.

To this end, a first (optimistic) possibility is to assume that a not perfect, but at least accurate, description of the scenario at the time t_0 is available, for instance, via the conversion of a high resolution diagnostic image into relative permittivity and conductivity maps. However, such a translation would be unavoidably affected by uncertainties, as the actual electromagnetic properties of different human tissues change from patient to patient. Moreover, a proper exploitation of a diagnostic image provided by another technique requires to tackle the nontrivial image registration problem, that is, the process of transforming different sets of data into a unique coordinate system.

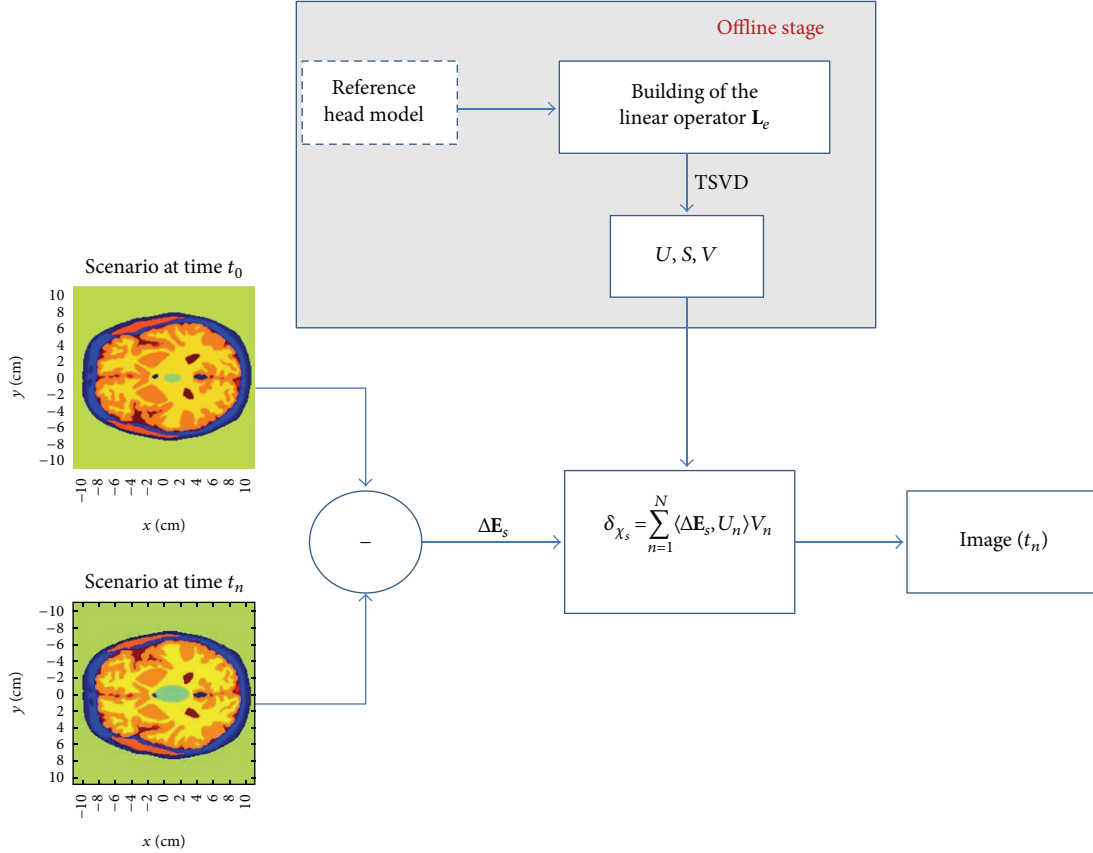


FIGURE 1: Flow chart of the proposed procedure for differential MWI followup of brain stroke.

An alternative, and much more simple solution is suggested by the linear nature of the imaging problem at hand. As a matter of fact, within a linear framework, the nature of the scattering phenomenon (i.e., the field's perturbation due to the contrast variation) is inherently local, so that the imaging performances are expected to be mostly influenced by the properties of the tissues surrounding the stroke, rather than those of the overall scenario (in our case the entire brain). Since the main kind of tissues constituting the brain (in the area where strokes typically occur) is white matter, a possible strategy amounts to build the required kernel using a simple reference model, in which the head is "filled" with a homogeneous medium having the average electric properties of white matter.

Accordingly, in the following numerical analysis, we have appraised the method's performance in both ideal conditions (i.e., when an almost exact map of the brain tissue electric properties is available) and for the simple, nonspecific, scenario described above. It is important to remark that a meaningful difference exists between the two cases from a computational point of view, since using the nonspecific scenario, allows us not only to overcome the aforementioned issues, but also to achieve images in real-time. As a matter of fact, the computationally intensive parts of the TSVD image formation procedure consist in the construction (through the solution of several forward scattering problems) of the matrix representing the discretized version of the operator

L_e^0 and the evaluation of its singular system. In principle, this matrix depends on the adopted electromagnetic scenario and therefore should change from patient to patient. Conversely, the possibility of performing this computation with respect to a non-patient-specific scenario allows moving this task to an offline stage, thus only limiting the actual image formation stage to the actual evaluation of (4). This latter is a computationally inexpensive task, as it requires to evaluate N scalar products involving vectors of size $P(P+1)/2$.

In the following numerical analysis, we will check the validity and the performance achieved when applying the proposed differential TSVD imaging scheme using this simplified scenario to build the inversion kernel.

In Figure 1, we report the flow chart of the proposed procedure, in which the role of the reference scenario is highlighted.

4. Numerical Analysis

To assess the achievable reconstruction capabilities of the proposed strategy, we have considered the 2D reference permittivity profile shown in Figure 2(a), which corresponds to the slice number 63 (in the z direction) of the Zubal anthropomorphic head phantom [19]. The dielectric properties of the involved biological tissues have been set according to [20]. An ischemic stroke has been simulated as an elliptic inclusion positioned at $x = 1$ cm and $y = 0$ cm with major and minor

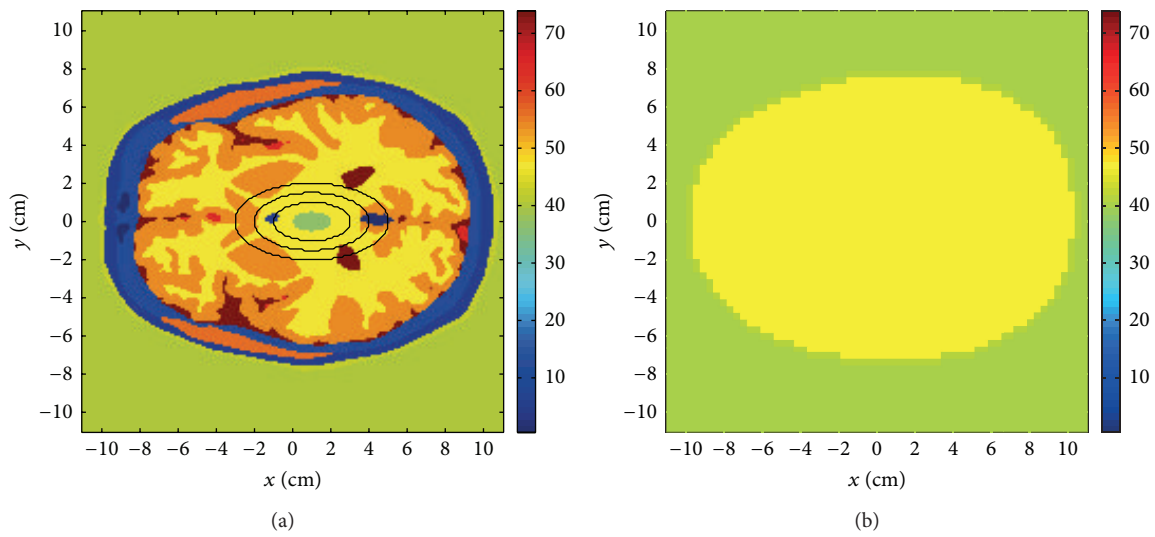


FIGURE 2: The 2D phantom: (a) scenario at the time t_0 : the stroke area is represented by the green ellipse at the center of the head, while the black contours represent its growth during the monitoring time, that is, the stroke's size at time instants t_1 , t_2 , and t_3 , respectively; (b) Nonspecific reference scenario used for the TSVD inversion scheme.

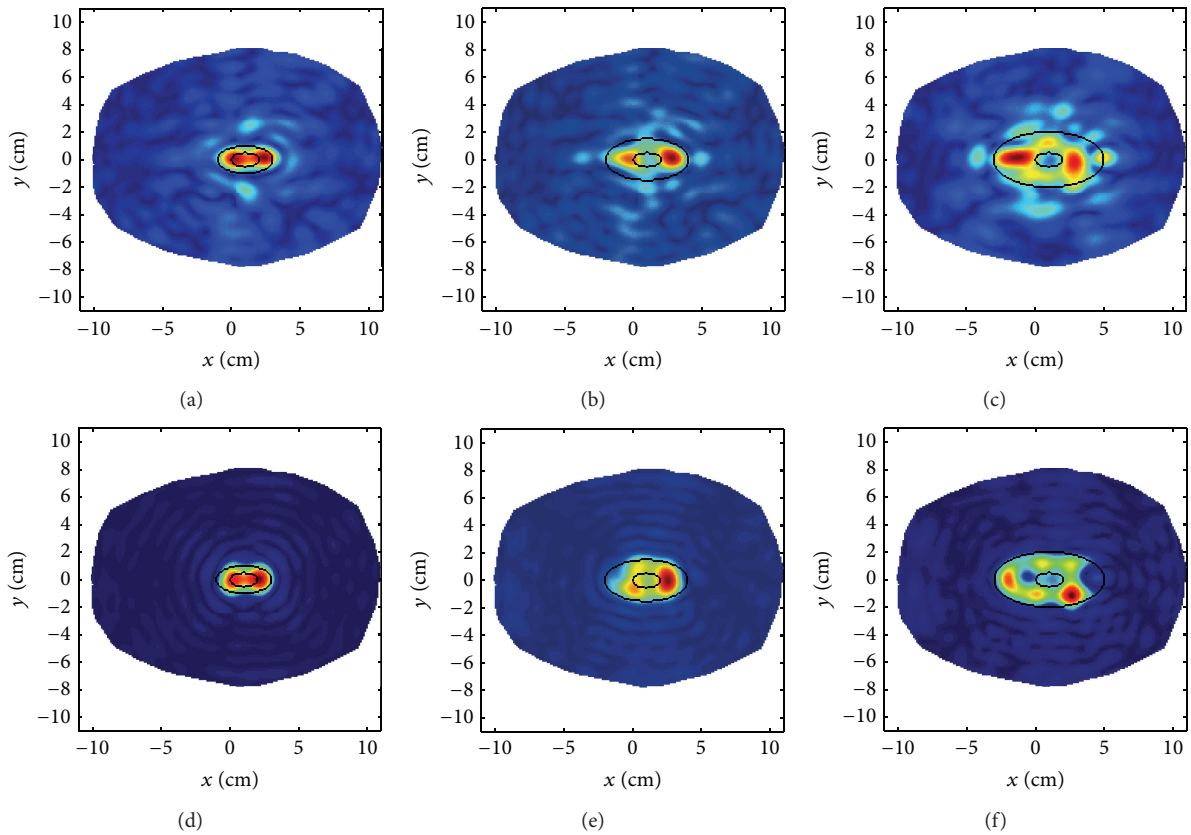


FIGURE 3: Assessment of the role played by patient specific information on the proposed TSVD imaging approach: (a)–(c) time evolution of an ischemic stroke when a nonspecific reference head model is adopted; (d)–(f) the same as (a)–(c) but using an accurate reference scenario in the inversion. The images report the normalized amplitude of the differential contrast as retrieved from (4), so that red areas mark the portion of the head where main changes are occurring. In all cases noiseless data have been processed.

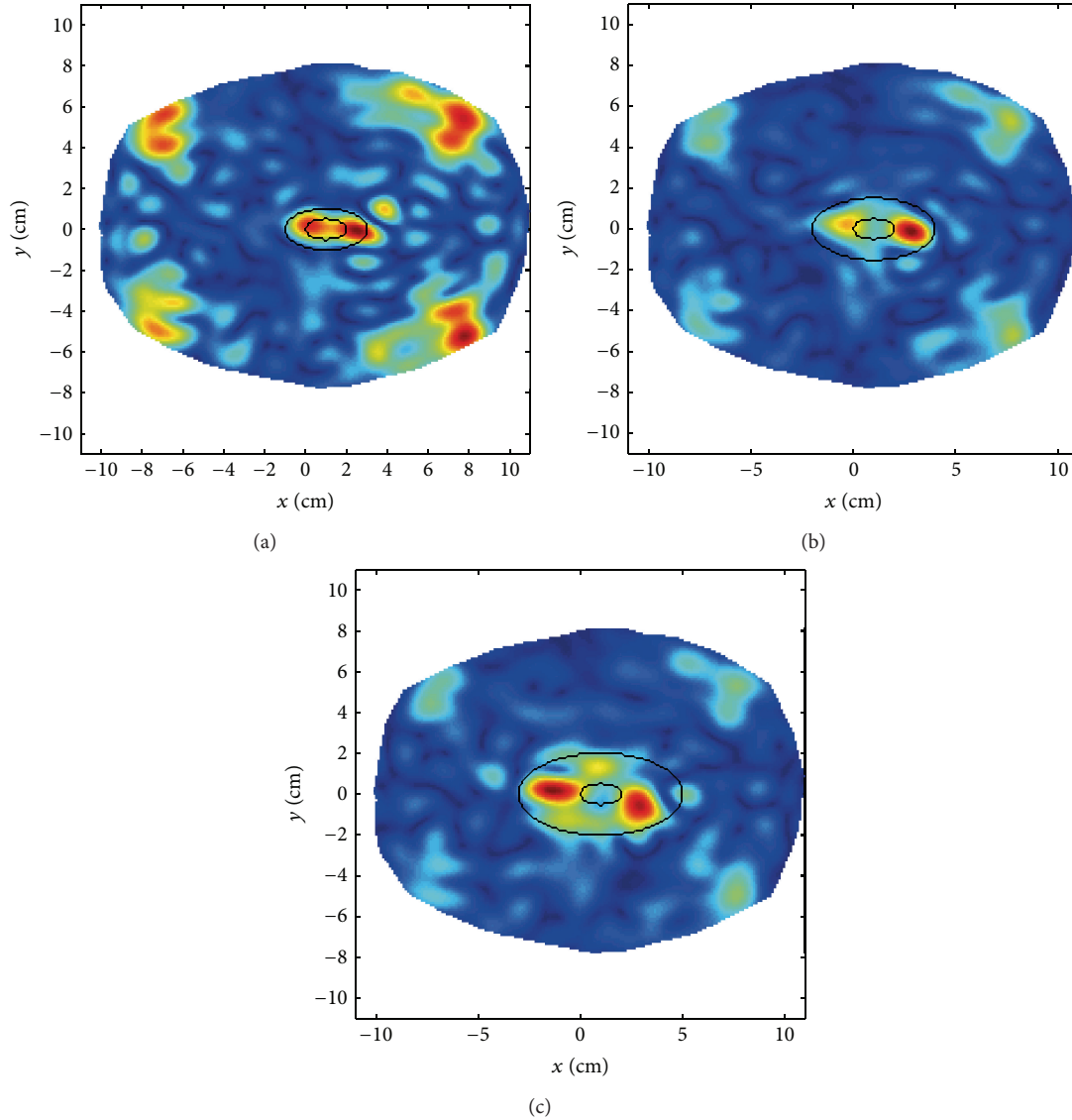


FIGURE 4: Assessment of the role played by the inaccurate positioning of the device between the two measurement time instants (noiseless data). The actual reference scenario is assumed to build the inversion kernel. The images report the normalized amplitude of the differential contrast as retrieved from (4), so that red areas mark the portion of the head where changes are occurring.

semiaxis of 1 cm and 0.5 cm, respectively, and having electric properties $\epsilon_s = 36$ and $\sigma_s = 0.72$ S/m.

The working conditions have been set according to the guidelines reported in our previous studies [14]. In particular, these results suggest that frequencies lower than 1 GHz represent a suitable choice. Hence, to accommodate the trade-off between wave penetration and achievable spatial resolution, we assume that probes work at 1 GHz and that the head is supposed to be surrounded by a matching medium having electric properties $\epsilon_b = 40$ and $\sigma_b = 0.4$ S/m, which can be for instance achieved through a proper mixture of water and Triton X100 [21]. Note that the use of a matching liquid requires the adoption of suitable solution when setting the device in practice, as done for instance in [18], where antennas are covered with plastic bags filled with the adopted matching medium.

In the simulations, the differential data have been gathered using 32 infinite length filamentary antennas oriented along the z -axis. Sources and measurement points are evenly spaced on a circumference having radius $r = 18$ cm surrounding the investigated domain, that is, a square of side 22 cm. Note that the number of probes herein considered is chosen in such a way to collect all the available information, according to the Degrees of Freedom (DOF) [22, 23].

The first reported example deals with the followup of an ischemic stroke. In particular, in Figure 2(a), the stroke in its initial stage is shown, that is, at the instant t_0 corresponding to the first diagnosis, while the black contours describe its evolution in time, at the instants t_1, t_2 , and t_3 . In Figure 2(b), it is shown the nonspecific reference model adopted to perform the inversion. For the sake of comparison, also an almost ideal case in which the reference model has been built by

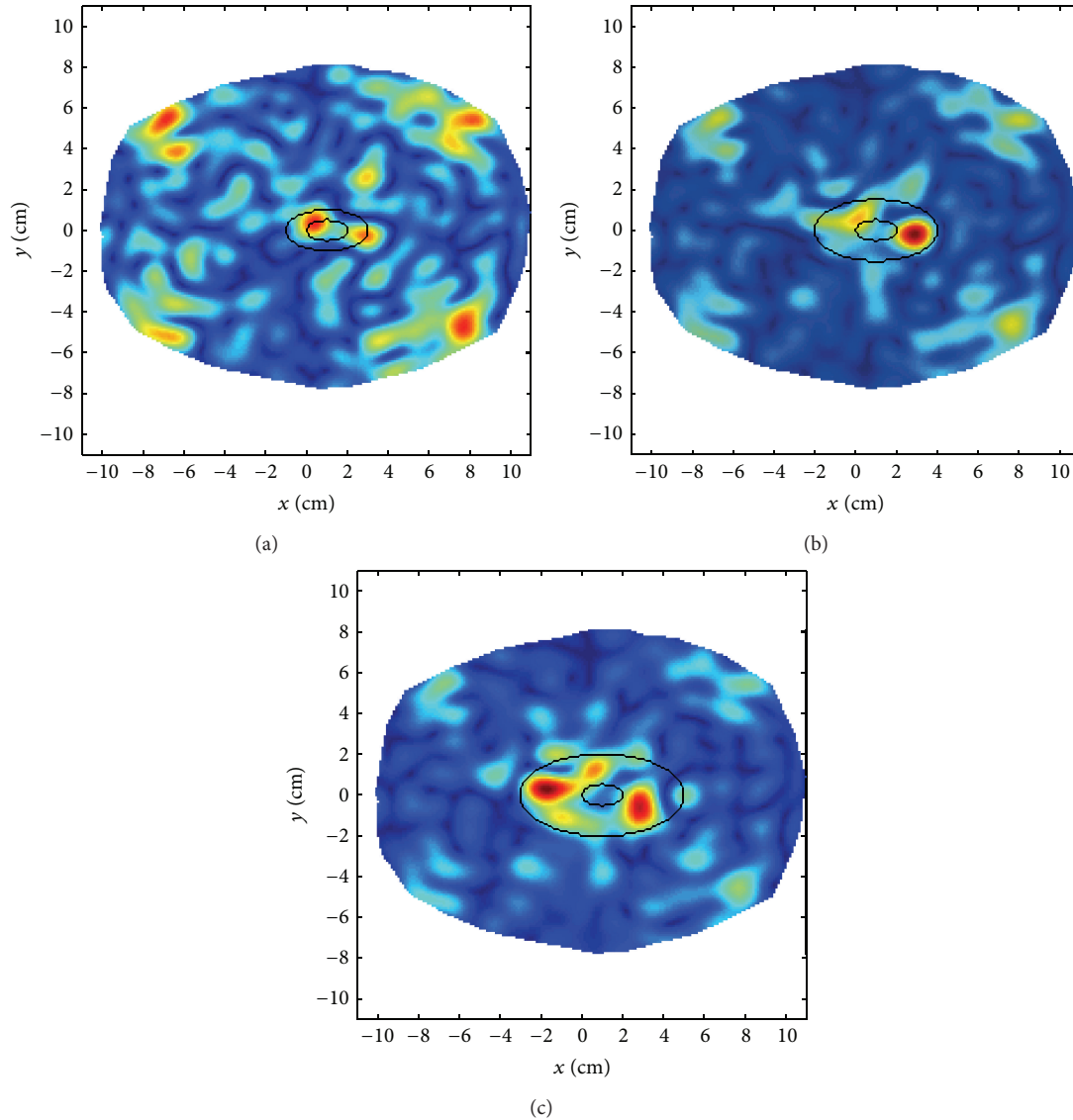


FIGURE 5: Followup of a postdiagnosis evolution of an ischemic brain stroke via the proposed differential TSVD imaging approach in realistic conditions. (a) t_1 ; (b) t_2 ; (c) t_3 . The images report the normalized amplitude of the differential contrast as retrieved from (4), so that red areas mark the portion of the head where changes are occurring. A gaussian noise with $\text{SNR} = 70$ dB and a 2° displacement of the probes have been assumed. The nonspecific reference head model is adopted in the TSVD algorithm.

corrupting the exact relative permittivity and conductivity maps shown in Figure 2(a) with a $\pm 5\%$ random error on each pixel. The results of this first comparison are shown in Figures 3(a)–3(f). As can be seen, the lack of patient specific information does not significantly affect the obtained images and, more importantly, still allows to follow the evolution of the stroke over time. In the ideal case, the TSVD truncation index has been set equal to 332, while in the simplified reference scenario it is 362.

The second example deals with the effect of a mismatch in the position of the probes between two consecutive measurement times. To this end, considering that the measurement apparatus is typically constituted by a fixed geometry array, so that probes can not change their relative position, a displacement of 2 degrees has been introduced. Note that in

this case the almost ideal reference scenario has been adopted ($N = 332$). As can be seen from Figure 4, in this situation, the adopted TSVD based approach still provides a reliable reconstruction. In particular, the inaccurate positioning of the device results in some artifacts located in the corners of the imaged domain. While this is of course a not desirable outcome, the fact that these inaccuracies exhibit symmetries entails the possibility of recognizing them as spurious artifacts, possibly suggesting the medical staff the repositioning of the apparatus.

The final assessment has been carried out in almost realistic conditions, that is, using the nonspecific reference scenario and assuming that data are affected by both an erroneous positioning of the probes (an offset of 2 degrees) and measurement noise. In particular, synthetic data have been

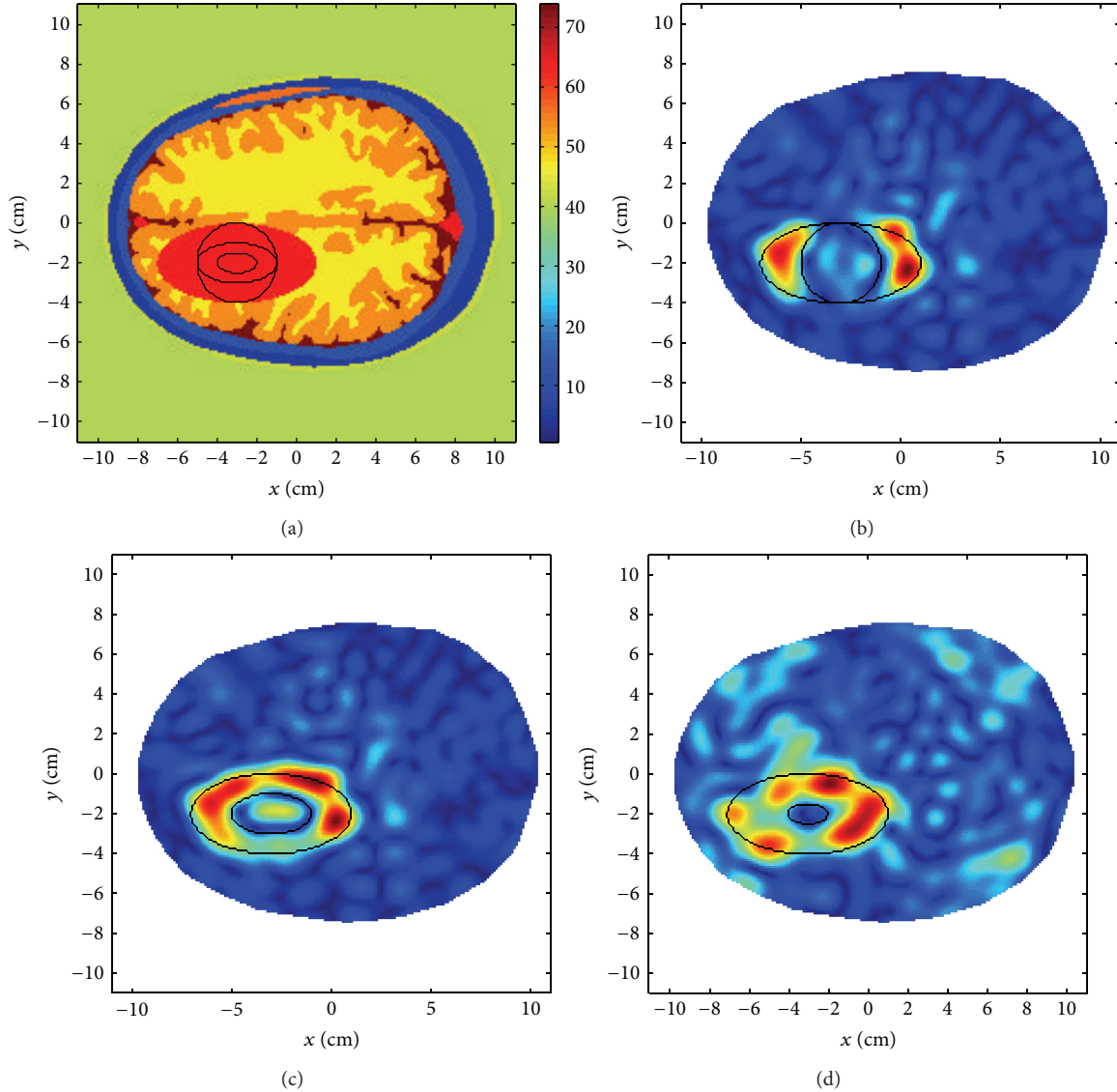


FIGURE 6: Followup of a postdiagnosis evolution of a hemorrhagic brain stroke via the proposed differential TSVD imaging approach in realistic conditions. (a) Scenario at the time t_0 (stroke diagnosis). The stroke is the red ellipse, while black contours represent its evolution at times t_1 , t_2 , and t_3 ; (b) normalized amplitude of the retrieved contrast at time t_1 ; (c) as (b) but at time t_2 ; (d) as (b) but at time t_3 . A gaussian noise with $\text{SNR} = 70$ dB and a 2° displacement of the probes has been assumed. The nonspecific reference head model is adopted in the inversion.

corrupted by a gaussian noise ($\text{SNR} = 70$ dB with respect to the total field). It is worth to note that such a noise level already entails that the useful signal (the differential scattered field) is almost overwhelmed by noise. This means that one has to take this circumstance into account in designing the device, as a constraint on the system's dynamic range. In this respect, it is certainly interesting that such a noise level is already achieved in MWI systems for other medical applications. Figures 5 shows the TSVD images (for $N = 327$) and confirm the capability of the proposed approach of correctly tracking the evolution of the stroke, even in the considered realistic conditions. This can be ascribed to the intrinsically low-pass nature of the TSVD procedure, which

is indeed robust against the presence of uncertainties on the reference scenario, as well as on the measured data.

In order to quantitatively appraise the above results, we have computed the relative root mean square (RMS) error of the normalized images in a region of interest surrounding the stroke. In particular, we have considered a rectangular area centered on the stroke $12 \text{ cm} \times 8 \text{ cm}$ wide. Table 1 summarizes the error values obtained in all cases, which fully confirm the conclusion that the approach is capable to provide accurate results without requiring patient-specific information.

As a further example, we have simulated the followup of a hemorrhagic stroke during the reabsorption stage, which is of interest to monitor the efficacy of drugs therapies. To

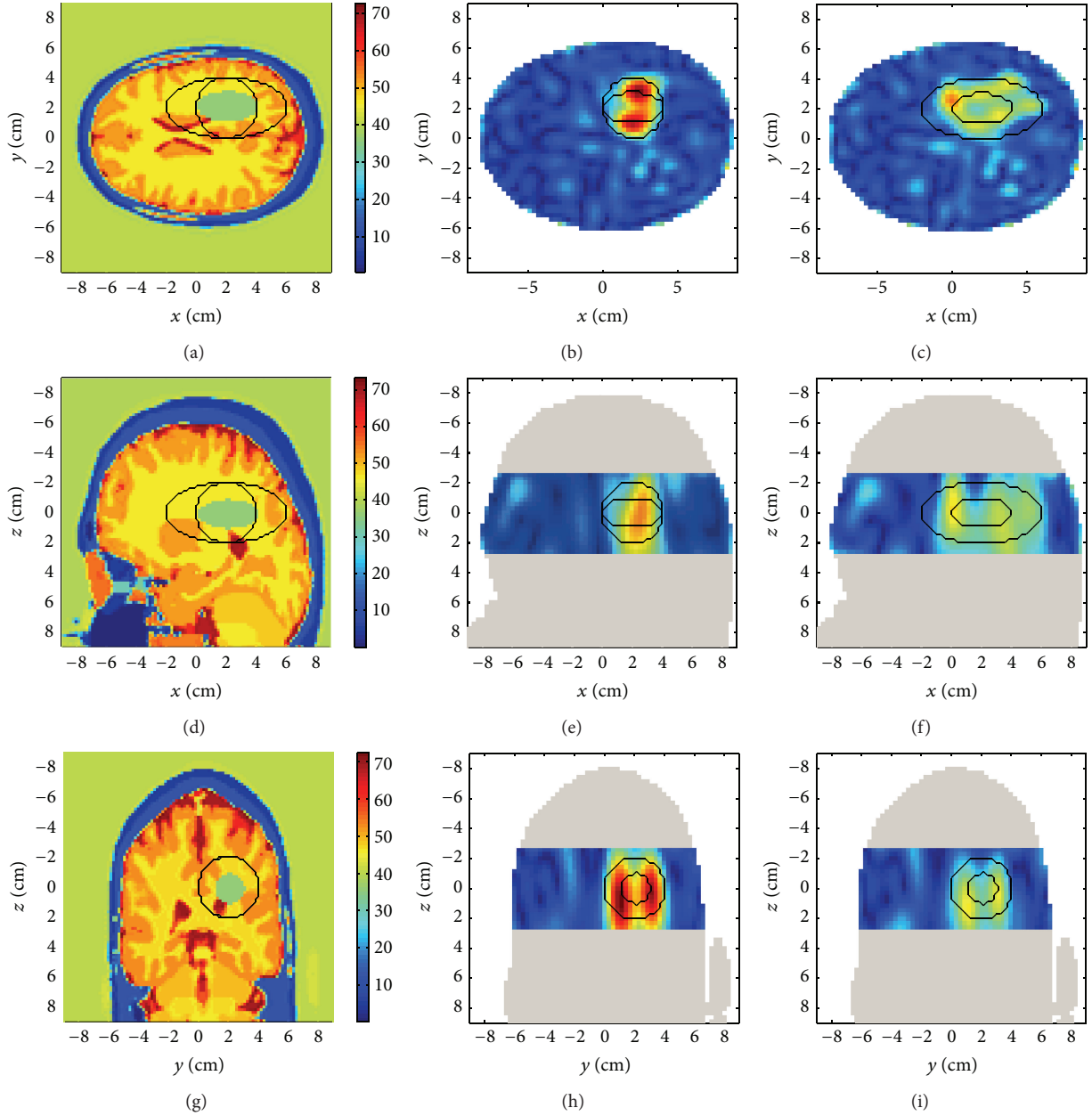


FIGURE 7: 3D validation of the followup of a postdiagnosis evolution of an ischemic brain stroke via the proposed differential TSVD imaging approach. (a) Scenario at the time T_0 (stroke diagnosis) with black contours referring to the stroke's position at times T_1 and T_2 ($x - y$ slice cutting the center of the stroke); (b) reconstruction at time T_1 : slice cutting the center of the stroke in the $x - y$ plane; (c) as (a) at time T_2 ; (d) reconstruction at time T_1 : slice cutting the center of the stroke in the $y - z$ plane; (e) as (c) at time T_2 ; (f) reconstruction at time T_1 : slice cutting the center of the stroke in the $x - z$ plane; (g) as (f) at time T_2 . A gaussian noise with SNR = 70 dB has been assumed and a simplified homogeneous reference head model is adopted.

this end, we have considered the phantom corresponding to slice 45 of the Zubal phantom [19] and the dimensions of the elliptic shaped stroke at times t_0 , t_1 , t_2 , and t_3 are, respectively, $a_0 = 2$ cm and $b_0 = 4$ cm, $a_1 = 2$ cm and $b_1 = 2$ cm, $a_2 = 1$ cm and $b_2 = 2$ cm, and $a_3 = 0.5$ cm and $b_3 = 1$ cm. In this case, the electric properties of the stroke are those of the blood at 1 GHz ($\epsilon_s = 61.1$, $\sigma_s = 1.6$ S/m). Corresponding permittivity profiles are shown in Figure 6(a), the obtained reconstructions (for $N = 335$) are reported in

Figures 6(b)–6(d). Again, the RMS error assumes quite low and stable values ($\text{RMS}(t_0) = 0.24$, $\text{RMS}(t_1) = 0.27$, and $\text{RMS}(t_2) = 0.28$).

5. A 3D Validation

The previous results were related to a 2D geometry. Clearly, such a schematization is only a simplification of the actual

TABLE 1: RMS error in the region of interest.

	t_1	t_2	t_3
Ideal conditions	0.16	0.21	0.31
Approximated scenario and ideal data	0.21	0.27	0.32
Probe's mismatch and exact reference scenario	0.25	0.24	0.32
Realistic conditions	0.30	0.30	0.34

scenario and cannot fully account for the complex (vectorial) interaction between electromagnetic waves and human tissues. Accordingly, in the following, we report a 3D first validation of the above concepts, in order to extend the findings achieved in 2D also in the 3D case.

When facing the 3D problem, the increase of the number of probes required to correctly acquire the information poses an issue concerned with the overall complexity of the apparatus and the required measurement time. For this reason and taking into account that DOF in the 3D case provides only an (loose) upper bound to the actually available information [23], the proof-of-concept reported in the following is aimed to show the feasibility of the proposed follow-up procedure, with respect to an apparatus whose overall number of antennas is in the same order as the “ideal” one adopted in the 2D case. Accordingly, we have considered a simple measurement configuration, in which 24 elementary electric dipoles are displaced on three circles of radius $r_m = 13$ cm. On each circle 8 evenly spaced dipoles are located, but the relative position of the probes between the circles is not the same, but shifted of $\pi/24$. As a matter of fact, such a staggering of the antennas allows us to increase the spatial diversity among the different measurements, thus increasing the amount of collectable information [24].

Another issue that has to be tackled in 3D is concerned with the required computational burden. In this respect, the above demonstrated capability of computing the inversion kernel with respect to a simplified nonspecific model is a crucial outcome, as it allows us to still build the image in real-time, performing the computationally intensive part of the algorithm offline, even before the measurement stage. On the other hand, this offline stage becomes obviously more demanding with respect to the 2D case, especially as far as the requirements of the computational facilities in terms of RAM are concerned. For this reason, to make the overall simulation feasible using a standard 8 GB RAM computer, but without affecting in any way the significance of the validation, we have considered a scaled version of the anthropomorphic Zubal phantom [19], in which the head has been reduced to 18 cm (instead of 22 cm), by scaling all the quantities.

The simulated ischemic stroke is supposed to lie at $x = 2$ cm, $y = 2$ cm, and $z = 0$ cm. At time t_0 its size is $a_0 = 1$ cm, $b_0 = 2$ cm, and $c_0 = 1$ cm; at time t_1 its size is $a_1 = 2$ cm, $b_1 = 2$ cm, and $c_1 = 2$ cm; at time t_2 its size is $a_2 = 2$ cm, $b_2 = 4$ cm, and $c_2 = 2$ cm. In Figure 7(a) the slice cutting the center of the stroke along the z -axis is shown, with the black contours indicating the evolution of the stroke area. The reference model has been built with respect to the portion

of the head enclosed by the probes and the synthetic data have been corrupted by a gaussian noise with SNR = 70 dB (with respect to the total field). The TSVD truncation index is $N = 210$. The $x - y$, $y - z$, and $x - z$ sections of the TSVD reconstructions across the stroke at time t_1 and t_2 are reported in Figures 7(b)–7(d) and Figures 7(c)–7(e), respectively. The RMS error as computed in a volume of size $8 \times 4 \times 5$ cm centered on the stroke is 0.24 at t_1 and 0.29 at t_2 . As can be seen, reliable images are still obtained using a simple measurement apparatus close to actually feasible systems [18].

6. Conclusions

We have proposed and assessed a robust procedure for brain stroke followup, which is an application of emerging clinical importance in stroke treatment [3]. In particular, we have shown that an inversion strategy based on a TSVD algorithm is capable of obtaining reliable and readable images of the stroke's evolution even without patient-specific information and in presence of inaccuracies in the measurement process, arising from positioning errors from one acquisition to the other and measurement noise.

In particular, the possibility of achieving the diagnostic image without translating MRI or CT images into electric maps of the brain, but rather exploiting a very simple nonspecific reference model, is crucial to have an actual possibility of practical exploitation. As a matter of fact, the computationally intensive part of the processing scheme is pursued offline, while the actual image formation is carried out in real time.

Finally, the preliminary assessment in the realistic 3D scenario has shown that the procedure can work even with very simple measurement configurations. Accordingly, ongoing efforts are focused on the optimization of the apparatus in order to obtain better images, while keeping the system as simple as possible. For example, an alternative way to exploit a simple measurement apparatus like the considered one is moving the system and collecting the scattered field at different quotas.

Conflict of Interests

The authors declare that there is no conflict of interests.

References

- [1] G. A. Donnan, M. Fisher, M. Macleod, and S. M. Davis, “Stroke,” *The Lancet*, vol. 371, no. 9624, pp. 1612–1623, 2008.
- [2] J. Olesen, A. Gustavsson, M. Svensson, H.-U. Wittchen, and B. Jönsson, “The economic cost of brain disorders in Europe,” *European Journal of Neurology*, vol. 19, no. 1, pp. 155–162, 2012.
- [3] E. C. Jauch, J. L. Saver, H. P. Adams et al., “Guidelines for the early management of patients with acute ischemic stroke: a guideline for healthcare professionals from the American Heart Association/American Stroke Association,” *Stroke*, vol. 44, no. 3, pp. 870–947, 2013.
- [4] A. Cavallini, G. Micieli, S. Marcheselli, and S. Quaglini, “Role of monitoring in management of acute ischemic stroke patients,”

- Stroke*, vol. 34, no. 11, pp. 2599–2603, 2003.
- [5] A. Rocco, M. Pasquini, E. Cecconi et al., “Monitoring after the acute stage of stroke: a prospective study,” *Stroke*, vol. 38, no. 4, pp. 1225–1228, 2007.
- [6] J. Gubbi, A. S. Rao, K. Fang, B. Yan, and M. Palaniswami, “Motor recovery monitoring using acceleration measurements in post acute stroke patients,” *BioMedical Engineering*, vol. 12, article 33, 2013.
- [7] S. Y. Semenov, R. H. Svenson, V. G. Posukh et al., “Dielectrical spectroscopy of canine myocardium during acute ischemia and hypoxia at frequency spectrum from 100 kHz to 6 GHz,” *IEEE Transactions on Medical Imaging*, vol. 21, no. 6, pp. 703–707, 2002.
- [8] S. Y. Semenov and D. R. Corfield, “Microwave tomography for brain imaging: feasibility assessment for stroke detection,” *International Journal of Antennas and Propagation*, vol. 2008, Article ID 254830, 8 pages, 2008.
- [9] T. Isernia, V. Pascazio, and R. Pierri, “On the local minima in a tomographic imaging technique,” *IEEE Transactions on Geoscience and Remote Sensing*, vol. 39, no. 7, pp. 1596–1607, 2001.
- [10] M. Bertero and P. Boccacci, *Introduction to Inverse Problems in Imaging*, Institute of Physics, Bristol, UK, 1998.
- [11] R. Scapaticci, O. M. Bucci, I. Catapano, and L. Crocco, “A robust Microwave Imaging for brain stroke monitoring,” in *Proceedings of the European Conference on Antennas and Propagation (EuCAP '13)*, Gothenburg, Sweden, 2013.
- [12] A. Broquetas, J. Romeu, J. M. Rius, A. R. Elias-Fuste, A. Cardama, and L. Jofre, “Cylindrical geometry: a further step in active microwave tomography,” *IEEE Transactions on Microwave Theory and Techniques*, vol. 39, no. 5, pp. 836–844, 1991.
- [13] P. M. Meaney, T. Zhou, M. W. Fanning, S. D. Geimer, and K. D. Paulsen, “Microwave thermal imaging of scanned focused ultrasound heating: phantom results,” *International Journal of Hyperthermia*, vol. 24, no. 7, pp. 523–536, 2008.
- [14] R. Scapaticci, L. di Donato, I. Catapano, and L. Crocco, “A feasibility study on Microwave Imaging for brain stroke monitoring,” *Progress in Electromagnetics Research B*, vol. 40, pp. 305–324, 2012.
- [15] M. Guardiola, L. Jofre, S. Capdevila, S. Blanch, and J. Romeu, “UWB brain differential imaging capabilities,” in *Proceedings of the European Conference on Antennas and Propagation (EuCAP '12)*, Prague, Czech Republic, 2012.
- [16] A. Fhager and M. Persson, “A microwave measurement system for stroke detection,” in *Proceedings of the 7th Loughborough Antennas and Propagation Conference (LAPC '11)*, pp. 1–2, Loughborough, UK, November 2011.
- [17] A. Fhager and M. Persson, “Stroke detection and diagnosis with a microwave helmet,” in *Proceedings of the 6th European Conference on Antennas and Propagation (EuCAP '12)*, pp. 1796–1798, 2012.
- [18] A. Fhager, Y. Yinan, T. McKelvey, and M. Persson, “Stroke diagnostics with a microwave helmet,” in *Proceedings of the 7th European Conference on Antennas and Propagation (EuCAP '13)*, pp. 845–846, 2013.
- [19] I. G. Zubal, C. R. Harrell, E. O. Smith, Z. Rattner, G. Gindi, and P. B. Hoffer, “Computerized three-dimensional segmented human anatomy,” *Medical Physics*, vol. 21, no. 2, pp. 299–302, 1994.
- [20] “Dielectric properties of body tissues in the frequency range 10 Hz–100 GHz,” <http://niremf.ifac.cnr.it/tissprop/>.
- [21] S. Romeo, L. di Donato, O. M. Bucci et al., “Dielectric characterization study of liquid-based materials for mimicking breast tissues,” *Microwave and Optical Technology Letters*, vol. 53, no. 6, pp. 1276–1280, 2011.
- [22] O. M. Bucci, C. Gennarelli, and C. Savarese, “Representation of electromagnetic fields over arbitrary surfaces by a finite and nonredundant number of samples,” *IEEE Transactions on Antennas and Propagation*, vol. 46, no. 3, pp. 351–359, 1998.
- [23] O. M. Bucci and T. Isernia, “Electromagnetic inverse scattering: retrievable information and measurement strategies,” *Radio Science*, vol. 32, no. 6, pp. 2123–2137, 1997.
- [24] O. M. Bucci, L. Crocco, and R. Scapaticci, “On the optimal measurement configuration for magnetic nanoparticles enhanced breast cancer microwave imaging,” submitted.

Research Article

Evaluation of the Electromagnetic Power Absorption in Humans Exposed to Plane Waves: The Effect of Breathing Activity

Marta Cavagnaro, Erika Pittella, and Stefano Pisa

Department of Information Engineering, Electronics and Telecommunications, Sapienza University of Rome, 00184 Rome, Italy

Correspondence should be addressed to Erika Pittella; pittella@diet.uniroma1.it

Received 28 June 2013; Accepted 27 November 2013

Academic Editor: Andrea Borsic

Copyright © 2013 Marta Cavagnaro et al. This is an open access article distributed under the Creative Commons Attribution License, which permits unrestricted use, distribution, and reproduction in any medium, provided the original work is properly cited.

The safety aspects of the exposure of people to uniform plane waves in the frequency range from 900 MHz to 5 GHz are analyzed. Starting from a human body model available in the literature, representing a man in resting state, two new anatomical models are considered, representing different phases of the respiratory activity: tidal breath and deep breath. These models have been used to evaluate the whole body Specific Absorption Rate (SAR) and the 10-g averaged and 1-g averaged SAR. The analysis is performed using a parallel implementation of the finite difference time domain method. A uniform plane wave, with vertical polarization, is used as an incident field since this is the canonical exposure situation used in safety guidelines. Results show that if the incident electromagnetic field is compliant with the reference levels promulgated by the International Commission on Non-Ionizing Radiation Protection and by IEEE, the computed SAR values are lower than the corresponding basic restrictions, as expected. On the other side, when the Federal Communications Commission reference levels are considered, 1-g SAR values exceeding the basic restrictions for exposure at 4 GHz and above are obtained. Furthermore, results show that the whole body SAR values increase passing from the resting state model to the deep breath model, for all the considered frequencies.

1. Introduction

The fast developments of wireless communications systems, such as Universal Mobile Telecommunications System (UMTS), WiFi, and Worldwide Interoperability for Microwave Access (WiMAX), have increased the spectrum of fields radiated by the fixed stations of these systems to frequencies up to 5 GHz [1]. Moreover, biomedical applications of electromagnetic fields at microwave frequencies, as the remote monitoring of vital signs, are gaining increasing attention [2, 3]. Therefore, the study of human exposure at frequencies between 900 MHz and 5 GHz is an up-to-date topic in order to assess the compliance of the electromagnetic field with exposure guidelines [4–7].

Exposure guidelines are defined in terms of basic restrictions, which are maximum values directly linked to health effects, and in terms of reference levels, which are values related to the incident electromagnetic fields more easily measurable in actual applications [4–7]. In the considered frequency range the basic restrictions are defined in terms

of the Specific Absorption Rate (SAR) as averaged over the whole body or over a local mass [4–7]. From the exposure guideline point of view, an important change has occurred within the 2005 version of the IEEE exposure standard [6] with respect to the previous versions [8]. In particular, for local exposure evaluation, the IEEE 2005 has adopted a limit on the 10-g averaged SAR, similarly to the ICNIRP basic restriction, in place of the limit on the 1-g averaged SAR present in the preceding versions of the Standard [8]. Moreover, the ICNIRP reference levels for the unperturbed incident field have been also adopted [6]. However the 1-g averaged SAR is still implemented by the Federal Communications Commission (FCC) regulation [7].

In the last decade the progress in computer resources has made the numerical studies of human exposure to electromagnetic fields feasible for anatomically realistic body models and for frequencies up to 1 GHz and above [9–12]. Moreover several numerical models of the human body have been developed and studied [13–17]. However, all the reported studies have considered human models with

the lung at resting state. On the other side, the development of anatomical models of breathing subjects could be very helpful to evaluate safety issues related to newly developed diagnostic techniques. As an example, Ultra Wideband Radars for the remote monitoring of the human respiratory activity are spreading in recent years.

In this paper, three human body models have been considered. Starting from Duke of the Virtual Family [13], two new anatomical models have been developed taking into account the respiration physiology and the pulmonary mechanics. These new models, representing a tidal and a deep breath, have been obtained through an automatic procedure [18]. The exposure of these three different breathing adult models to an incident electromagnetic field with frequencies in the range 900 MHz–5 GHz is studied by using a parallel implementation of the finite difference time domain (FDTD) method. The whole body SAR, the SAR as averaged on 10-g mass and 1-g mass (SAR_{WB} , SAR_{10-g} , and SAR_{1-g}) are computed, taking into account the frequency dependence of the dielectric properties of biological tissues, and also the variations of the dielectric properties and mass density of the lungs during respiration.

The paper is organized as follows: in Section 2, the numerical method and the human anatomical models are presented; in Section 3 results of dosimetry studies for the three breathing subject models are shown in terms of SAR. Eventually, in Section 4 conclusions are drawn.

2. Methods and Models

2.1. FDTD Method. The SAR computations are performed by using a self-developed code [19]. This code applies the FDTD method that divides the domain under study in elementary cells. To excite the impinging plane wave the whole volume is divided into a total-field and a scattered-field region by means of a Huygens' surface [20, 21]. The scattered-field region is closed by applying a uniaxial perfectly matched layer (UPML) absorbing boundary condition made by 5 cells with a parabolic spatial dependence for the electric and magnetic conductivities, and whose maximum values give a theoretical reflection coefficient lower than 0.01% [21]. A spatial resolution of 1 mm was chosen for the simulations. At the highest frequency of interest (5 GHz) this resolution corresponds to less than 1/8 of the wavelength for all body tissues and it is almost equal to 1/10 of the penetration depth of the electromagnetic field. In [12] an expanded uncertainty of 0.2 dB on the SAR_{WB} and of 0.51 dB for the SAR_{10-g} was evaluated for 1-mm FDTD simulations taking into account grid resolution, absorbing boundary conditions, and steady-state convergence.

With reference to the source, a plane wave with sinusoidal time dependence propagating along the y -axis (front-back of the body model) and with the electric field polarized along the z -axis (feet-head direction of the body model) has been excited with an electric field amplitude corresponding to the ICNIRP and IEEE 2005 reference levels for general public at the different frequencies. For the 1-g averaged SAR

the reference levels for general public of FCC have been considered instead.

The 1-mm resolution of the human body model requires a huge amount of memory (higher than 15 GB) and computational time (several days). For this reason, a parallel implementation of the FDTD scheme based on the message passing interface (MPI) paradigm was used. Simulations were run on a cluster with a total of fifteen CPUs and about 26 GB of RAM. Execution time is about 8 hours for each considered model. The SAR_{10-g} and SAR_{1-g} have been computed by considering cubic volumes, whose sides are expanded until the desired mass is obtained, allowing a maximum 10% of air inclusion.

2.2. Human Breathing Models. As regards the human body models, the FDTD method requires an anatomical model divided into cells with different properties (voxel). Starting from an anatomical model available in the literature, new models of the human anatomy have been developed to represent different phases of the respiratory activity, taking into account the respiration physiology and the pulmonary mechanics [22]. In particular, the body models usually considered in dosimetry studies represent a resting state body (RS), that is a body at the end of the respiration phase, when little air is present into the lungs. In [18], through an automatic procedure, two new models have been developed from Duke of the Virtual Family. In brief, starting from the RS human model, constituted by a three-dimensional matrix of integer numbers representing the various tissues (77 tissues), lung cells have been added simulating both a diaphragm displacement and an enlargement of the rib cage. Changing the entity of the diaphragm displacement and of the rib cage enlargement, two respiration phases have been modelled: the tidal breath (TB), corresponding to a state of normal inspiration with an inhaled volume of air equal to about 500 mL, and the deep breath (DB), corresponding to a state in which the volume of inhaled air is increased by 860 mL. It is important to note that the DB case refers to a deeper respiration with respect to the tidal one, as expected for a subject during normal daily activities [22], and it does not correspond with the Inspiration Reserve Volume that is more than two times the RS.

Figure 1 shows the number of lung cells in each horizontal section of the human body, as a function of the height from the feet, for the three human body models considered: resting state, that is the original model, tidal breath, and deep breath. From the figure, an overall view of the levels where the lung expansion occurred is obtained. In particular, it can be noted that the rib cage expansion in the TB and DB models follows the behavior of the RS model in the higher sections (from 140 cm to 150 cm in Figure 1). Then the expansion becomes more irregular; this is due to the drop in the diaphragm of 2 cm and 4 cm for the TB model and DB model, respectively.

The two new lung models are anatomically consistent. Moreover, they have a final volume of 4262 mL and 4530 mL, for TB and DB, respectively. Since the initial volume was 3849 mL (RS), an increase in volume of about 413 mL and 681 mL has been found for TB and DB, respectively, in agreement with [22]. Figure 2 shows a 2D axial section at

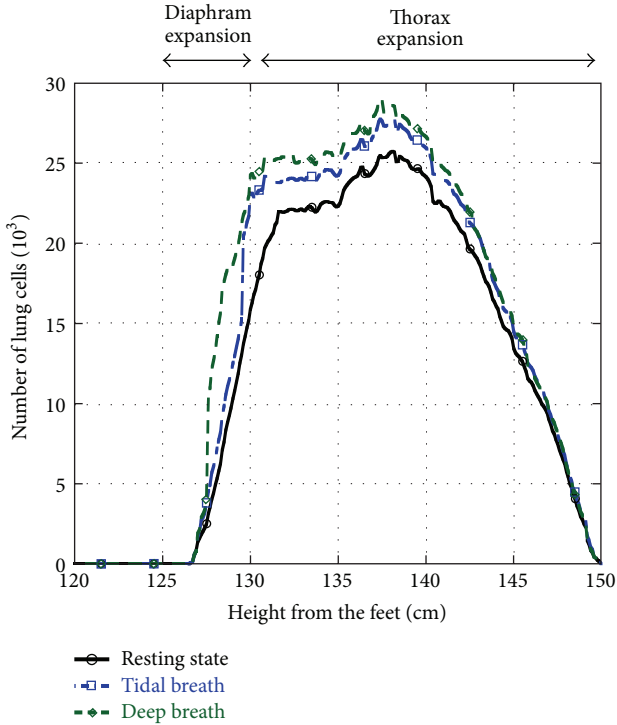


FIGURE 1: Number of lung cells, in the transversal plane, for the RS, TB, and DB models, as a function of the height from the feet.

the level of the diaphragm, for the RS and DB model. The figure evidences that in the DB model the diaphragm is not present anymore at this level due to its downward displacement.

In the simulations the values reported in the data base, available online [23], have been assigned to the dielectric parameters of the 77 tissues comprising the body models, taking into account the frequency dependence.

With reference to the lung, for the breathing models (TB and DB models), the mass density has been assumed equal to that of inflated lung ($\rho_{LI} = 394 \text{ kg/m}^3$) [23], while for the RS model (man at the end of the expiration phase) an average value between the inflated lung (ρ_{LI}) and deflated lung mass density ($\rho_{LD} = 1050 \text{ kg/m}^3$) has been used, since the lung is never totally deflated because of the dead space. As concerns the dielectric properties, the values for inflated lungs have been used for TB and DB models. At resting state, an average value between those of inflated and deflated lung has been used, according to the linear dependence of lung dielectric properties from the air volume filling factor [24].

3. Results

The obtained models have been exposed to a plane wave with frequencies between 900 MHz and 5 GHz.

When the SAR_{WB} and SAR_{10-g} have been evaluated, the incident power was defined equal to the ICNIRP and IEEE-2005 reference levels for general public; when the SAR_{1-g} has been considered, the incident power was settled equal to the FCC reference levels.

3.1. SAR Whole Body. SAR_{WB} values obtained in the Duke's breathing models as a function of frequency are depicted in Figure 3, together with the power density reference level allowed for general public in ICNIRP and IEEE 2005 guidelines [4, 6]. Results point out an increase in the SAR_{WB} with the frequency up to 2 GHz and a decrease above this frequency value.

However it is worth noting that this behavior is strictly due to the limits on the power density settled in the guidelines, which increase with the frequency up to 2 GHz and are maintained constant for higher frequencies, as clearly shown in Figure 3. Indeed a SAR_{WB} linearly decreasing with the frequency would be obtained if the power density is maintained constant for all the frequencies. From Figure 3 it can be noted that all the considered models lead to SAR_{WB} values compliant with the basic restrictions for all the considered frequencies. In particular, a very little difference is obtained in the values of the SAR_{WB} for the three anatomical breathing models at all the considered frequencies, with increasing values of the absorbed power passing from the resting state model to the deep breath model. However, increasing the frequency, the difference in the whole body SAR for the three considered models decreases (SAR_{WB} @900 MHz: $6.50 \cdot 10^{-2} \text{ W/kg}$ (RS), $6.54 \cdot 10^{-2} \text{ W/kg}$ (TB), $6.55 \cdot 10^{-2} \text{ W/kg}$ (DB); SAR_{WB} @5 GHz: $3.59 \cdot 10^{-2} \text{ W/kg}$ (RS), $3.71 \cdot 10^{-2} \text{ W/kg}$ (TB), $3.74 \cdot 10^{-2} \text{ W/kg}$ (DB)).

Figure 4 shows the SAR distribution in a coronal plane for the resting state model at two different frequencies (900 MHz and 5000 MHz). The figure evidences that the power absorption is strictly dependent on the frequency and that it remains superficially confined at the higher one.

3.2. SAR_{10-g} . Figure 5 shows the peak values of the SAR_{10-g} obtained in the head and trunk for the three considered body models, together with the corresponding ICNIRP and IEEE 2005 basic restriction. In the figure the incident power density allowed in ICNIRP and IEEE 2005 is also reported.

The figure shows an increase with the frequency of the obtained values up to 2.4 GHz, followed by a linear decrease. However, all the SAR_{10-g} values are well below the corresponding basic restriction (2 W/kg). It has to be noted here that the position where the maximum SAR_{10-g} is obtained changes with the frequency, from nose (for all the three models at 900 MHz) to genital organs (for RS at 1800 MHz and for all the three models at 2000 MHz and 5000 MHz), thorax (for TB and DB at 1800 MHz), chin (RS and DB at 2400 MHz), and neck (for TB at 2400 MHz).

With reference to the different anatomical models, no meaningful differences have been obtained in the SAR_{10-g} values. This is because these values are obtained mainly in the head and in the genital organs outside the area anatomically affected by the respiration. However, it is interesting to note that, at 1800 MHz, while the head-trunk maximum SAR_{10-g} is found in the genital organs of the RS models, it is found in the breast in the other two body models. This result could be linked to the wider thorax of the TB and DB models, with respect to the RS one, obtained as a consequence of the expansion of the lung volumes.

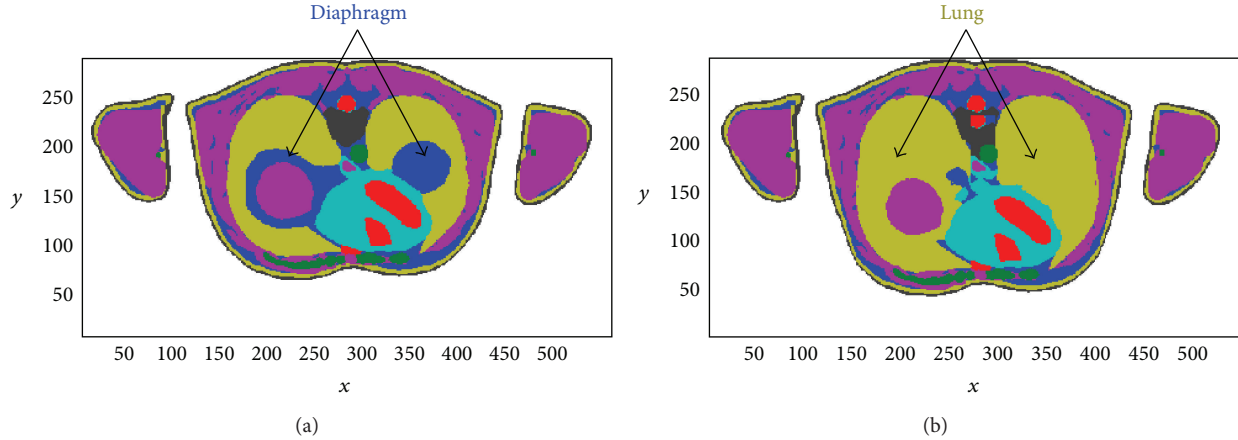


FIGURE 2: Bidimensional representation of an axial section ($z = 130$ cm) for the RS (a) and DB (b) model.

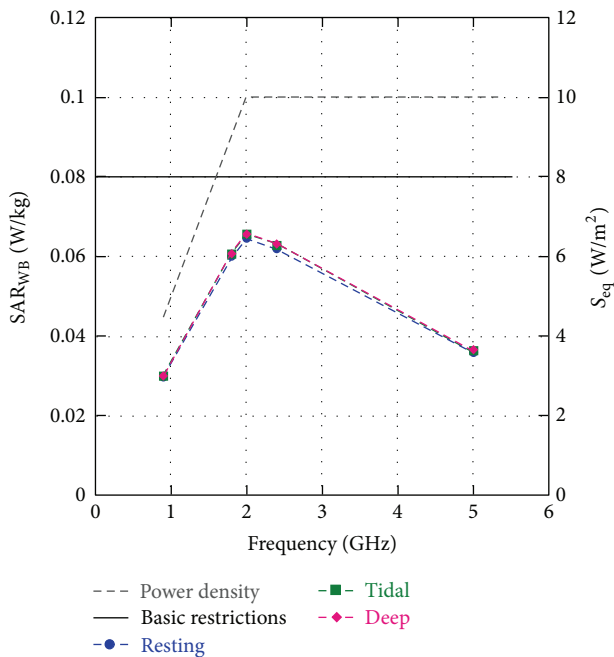


FIGURE 3: Whole body SAR for the RS, TB, and DB models and the input power density reference level allowed for general public in ICNIRP and IEEE 2005 guidelines.

3.3. SAR_{10-g} in the Lung. With reference to the lungs, the SAR_{10-g} values obtained for this particular tissue have been drawn in Figure 6 as a function of the frequency, for the three considered models. In the figure the power density reference levels, allowed for general public in ICNIRP and IEEE 2005 guidelines and used for the incident plane wave, are also reported.

From the figure it is clearly visible that the absorbed power increases passing from the resting state model to the deep model and that the higher difference occurs at 900 MHz (with a percentage variation of 76.77%), where the SAR_{10-g} moves from the value of 0.063 W/kg for the resting state to 0.110 W/kg for the deep breath model. This effect is due to

the decrease of the lung mass density from the deflated model (RS) to inflated ones (TB and DB).

3.4. SAR_{1-g} . Figure 7 shows the results related to the maximum SAR_{1-g} in the head and trunk. The position of the maximum SAR_{1-g} changes with the frequency, from the nose (for all the three models at 900 MHz, 1800 MHz, and 2000 MHz) to the neck (for all the three models at 2400 MHz) and genital organs (for all the three models at 5000 MHz). From the figure it is interesting to note the differences in the maximum SAR_{1-g} for the different body models. Moreover, it can be noted that the SAR_{1-g} increases with the frequency above 2.4 GHz, even if the incident power does not increase any more, contrary to the other SAR results. This increase leads to a local SAR exceeding the basic restriction level of 1.6 W/kg of the FCC regulation for frequencies above 4 GHz for all the considered models. Similar results have been obtained in [12], where the computed SAR_{1-g} values exceeded the basic restrictions of 1.6 W/kg at frequencies above 1.5 GHz, both for IEEE-1999 and FCC reference levels, for different models of adult and child.

With reference to the lungs, the SAR_{1-g} values obtained for this tissue have been drawn in Figure 8 as a function of the frequency, for the three considered models, together with the power density reference level allowed for general public in ICNIRP and IEEE 2005 guidelines.

From the figure it is clearly visible that the SAR_{1-g} increases passing from the resting state model to the deep breath model.

4. Conclusions

This paper addresses the safety aspects of people exposed to uniform plane waves in the frequency range from 900 MHz to 5 GHz. The problem has been analyzed using a parallel numerical code and considering three accurate models of breathing humans. These models have been developed through an automatic procedure starting from Duke's model available in the Virtual Family dataset. The human body models have been exposed to a plane wave with vertical

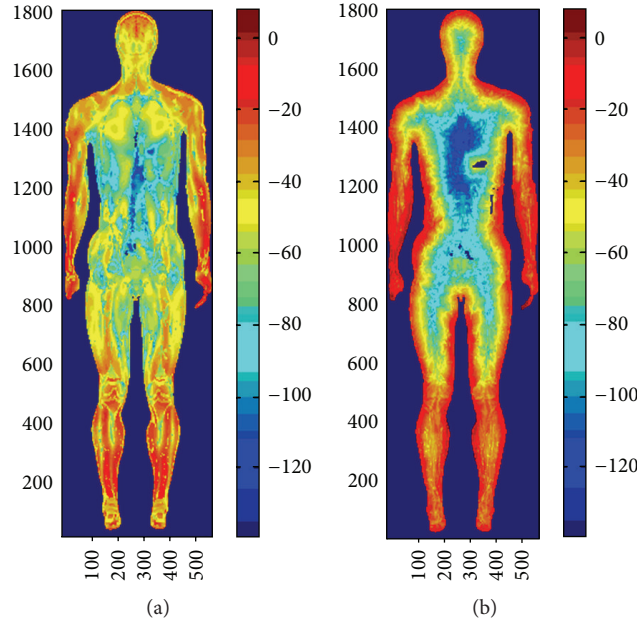


FIGURE 4: Whole body SAR (dB_{W/kg}) for the RS model at 900 MHz (a) and at 5000 MHz (b).

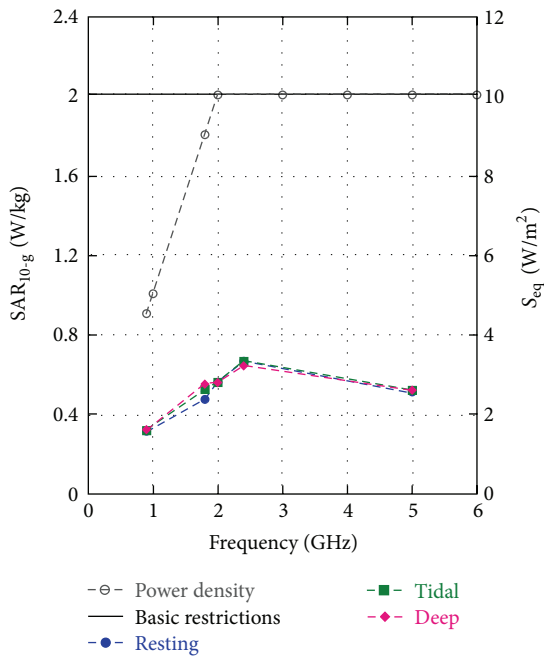


FIGURE 5: SAR_{10-g} for the RS, TB, and DB models and the power density reference level allowed for general public in ICNIRP and IEEE 2005 guidelines.

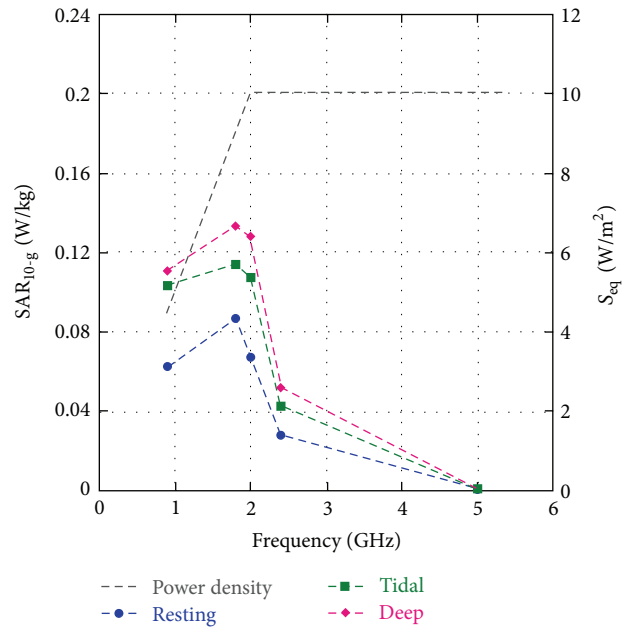


FIGURE 6: SAR_{10-g} in the lungs for the RS, TB, and DB models and the power density reference level allowed for general public in ICNIRP and IEEE 2005 guidelines.

polarization and with incident power densities equal to those settled by the safety guidelines for the different frequencies considered.

Results show that for all the considered frequencies and body models the SAR_{WB} and SAR_{10-g} do not exceed the 0.08 W/kg and 2 W/kg basic restrictions. Moreover, SAR_{WB} decreases with the frequency if the incident power density is

maintained constant and it is the most stringent parameter compared to SAR_{10-g}, for assessing the exposure compliance. On the other side, the SAR_{1-g} increases with the frequency and local SAR_{1-g} values exceeding the basic restriction of 1.6 W/kg are obtained above 4 GHz when the incident power density is settled at the FCC reference levels. From Figures 3, 5, and 7 it is interesting to note that the SAR_{WB} shows

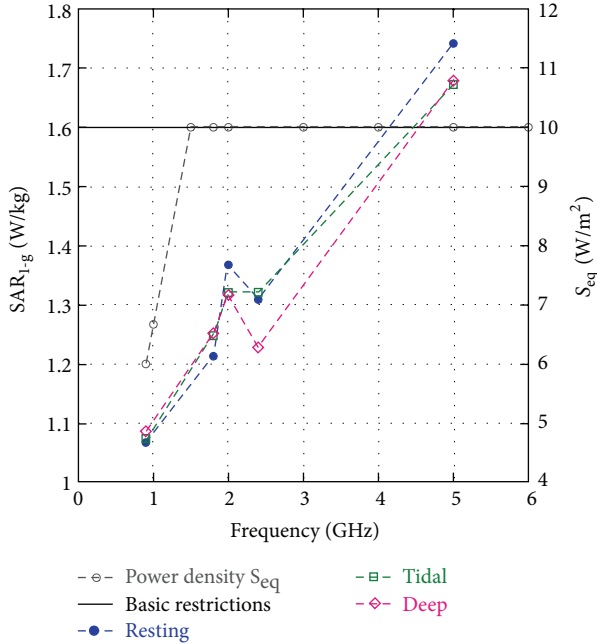


FIGURE 7: SAR_{1-g} for the RS, TB, and DB models for FCC reference levels. The FCC power density reference level allowed for general population is also reported.

the maximum value in correspondence of the frequency in which the maximum incident power density is allowed by the safety guidelines, while the SAR_{10-g} and the SAR_{1-g} maximum are obtained at higher frequencies. This different behavior is due to the fact that while the SAR_{WB} is directly linked to the total power impinging on the whole body model, the local SARs have different averaging volumes and are influenced by the field penetration depth that in turn depends on the electrical properties of the different tissues involved. Comparing the three body models, for all the considered frequencies, the SAR values are higher in the body model representing a deep respiration with respect to the model representing a resting state for the SAR_{WB} and SAR_{10-g}.

To conclude it is worth mentioning that the obtained results are based on specific body models developed from an adult male model and considering the dielectric properties values available in the literature [23]. With reference to the influence of the uncertainty of the dielectric properties values on the obtained SAR results, in [25] an extensive analysis has been conducted changing the dielectric properties values of the 39 tissues comprising a 3-mm resolution human body model and considering plane-wave irradiation at the frequencies of 200, 400, 918, and 2060 MHz. They found that the changing values did not substantially influence the SAR_{WB}, while a higher influence was obtained on localized SAR values for the individual tissues where the properties were changed. Finally, in [26, 27] a marginal effect of the variation of dielectric properties on the SAR_{10-g} was obtained (less than 10%). With reference to the body models used, further studies should be performed in order to confirm the obtained results considering different subject anatomies,

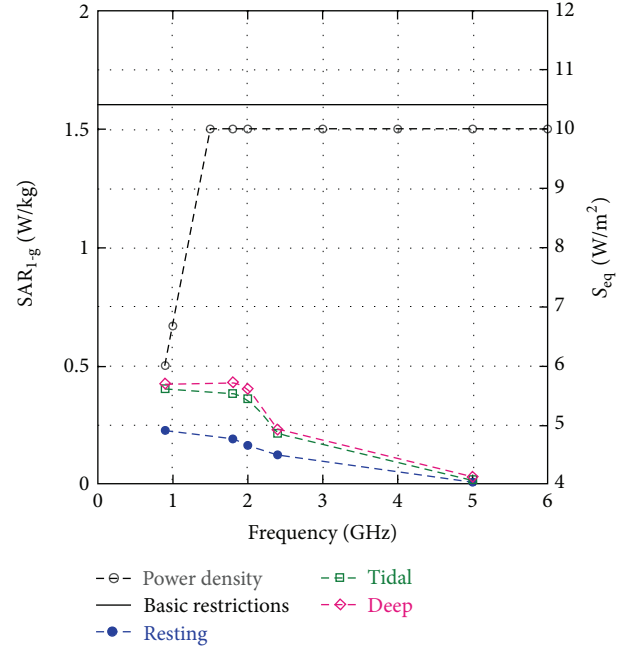


FIGURE 8: SAR_{1-g} in the lungs for the RS, TB, and DB models obtained for FCC reference levels. The FCC power density reference level allowed for general population is also reported.

women, and children as, for example, those developed by IT'IS Foundation. In particular, the automatic procedure used to develop the TB and DB body models could be applied to obtain breathing women and children. These models can be used both to study the absorption associated to exposure to the electromagnetic field emitted by communication systems and by biomedical applications of electromagnetic fields [28] and to characterize the human anatomy to be used in the development of new biomedical systems [29]. Furthermore, these models can be used to compute the Radar Cross Section (RCS) of man during respiration; this information is of great importance for ultrawideband radar design.

References

- [1] S. Allen, J. C. Lin, J. Bach Anderson et al., "ICNIRP statement on EMF-emitting new technologies," *Health Physics*, vol. 94, no. 4, pp. 376–392, 2008.
- [2] E. M. Staderini, "UWB radars in medicine," *IEEE Aerospace and Electronic Systems Magazine*, vol. 17, no. 1, pp. 13–18, 2002.
- [3] E. Pittella, P. Bernardi, M. Cavagnaro, S. Pisa, and E. Piuzei, "Design of UWB antennas to monitor cardiac activity," *Applied Computational Electromagnetics Society Journal*, vol. 26, no. 4, pp. 267–274, 2011.
- [4] ICNIRP, "ICNIRP statement on the guidelines for limiting exposure to time-varying electric, magnetic, and electromagnetic fields (UP to 300 GHz)," *Health Physics*, vol. 97, no. 3, pp. 257–258, 2009.
- [5] Commission of European Communities, Ed., *Council Recommendation on Limits For Exposure of the General Public To Electromagnetic Fields: 0 Hz-300 GHz*, EC, Brussels, Belgium, 1998.

- [6] IEEE Standard for Safety Levels with Respect to Human Exposure to Radio Frequency Electromagnetic Fields, 3 kHz to 300 GHz, IEEE Standard C95. 1, 2005.
- [7] Federal Communications Commission Office of Engineering & Technology, "Evaluating compliance with FCC guidelines for human exposure to radiofrequency electromagnetic fields," OET Bulletin 65, Washington, DC, 1997.
- [8] IEEE Standard for Safety Levels with Respect to Human Exposure to Radio Frequency Electromagnetic Fields, 3 kHz to 300 GHz, IEEE Standard C95. 1, 1999.
- [9] P. Bernardi, M. Cavagnaro, S. Pisa, and E. Piuze, "SAR distribution and temperature increase in an anatomical model of the human eye exposed to the field radiated by the user antenna in a wireless LAN," *IEEE Transactions on Microwave Theory and Techniques*, vol. 46, no. 12, pp. 2074–2082, 1998.
- [10] L. Sandrini, A. Vaccari, C. Malacarne, L. Cristoforetti, and R. Pontalti, "RF dosimetry: a comparison between power absorption of female and male numerical models from 0.1 to 4 GHz," *Physics in Medicine and Biology*, vol. 49, no. 22, pp. 5185–5201, 2004.
- [11] P. Bernardi, M. Cavagnaro, S. Pisa, and E. Piuze, "Specific absorption rate and temperature elevation in a subject exposed in the far-field of radio-frequency sources operating in the 10–900-MHz range," *IEEE Transactions on Biomedical Engineering*, vol. 50, no. 3, pp. 295–304, 2003.
- [12] E. Piuze, P. Bernardi, M. Cavagnaro, S. Pisa, and J. C. Lin, "Analysis of adult and child exposure to uniform plane waves at mobile communication systems frequencies (900 MHz–3 GHz)," *IEEE Transactions on Electromagnetic Compatibility*, vol. 53, no. 1, pp. 38–47, 2011.
- [13] A. Christ, W. Kainz, E. G. Hahn et al., "The virtual family—development of surface-based anatomical models of two adults and two children for dosimetric simulations," *Physics in Medicine and Biology*, vol. 55, no. 2, pp. N23–N38, 2010.
- [14] T. Nagaoka, S. Watanabe, K. Sakurai et al., "Development of realistic high-resolution whole-body voxel models of Japanese adult males and females of average height and weight, and application of models to radio-frequency electromagnetic-field dosimetry," *Physics in Medicine and Biology*, vol. 49, no. 1, pp. 1–15, 2004.
- [15] P. Dimbylow and W. Bolch, "Whole-body-averaged SAR from 50 MHz to 4 GHz in the University of Florida child voxel phantoms," *Physics in Medicine and Biology*, vol. 52, no. 22, pp. 6639–6649, 2007.
- [16] E. Conil, A. Hadjem, F. Lacroux, M. F. Wong, and J. Wiart, "Variability analysis of SAR from 20 MHz to 2.4 GHz for different adult and child models using finite-difference time-domain," *Physics in Medicine and Biology*, vol. 53, no. 6, pp. 1511–1525, 2008.
- [17] A. Hirata, I. Laakso, T. Oizumi, R. Hanatani, K. H. Chan, and J. Wiart, "The relationship between specific absorption rate and temperature elevation in anatomically based human body models for plane wave exposure from 30 MHz to 6 GHz," *Physics in Medicine and Biology*, vol. 58, pp. 903–921, 2013.
- [18] M. Cavagnaro, E. Pittella, and S. Pisa, "Anatomical models of breathing subjects for absorption and scattering analysis," in *Proceedings of the International Symposium on Electromagnetic Compatibility*, pp. 149–153, September 2013.
- [19] K. S. Nikita, M. Cavagnaro, G. Cerri, S. Chiarandini, R. De Leo, and P. Russo, "A study of uncertainties in modeling antenna performance and power absorption in the head of a cellular phone user," *IEEE Transactions on Microwave Theory and Techniques*, vol. 48, no. 12, pp. 2676–2685, 2000.
- [20] K. S. Kunz and R. J. Luebbers, *The Finite Difference Time Domain Method For Electromagnetics*, CRC Press, Boca Raton, Fla, USA, 1993.
- [21] A. Taflove, *Computational Electrodynamics: the Finite-Difference Time-Domain Method*, Artech House, Norwood, Mass, USA, 1995.
- [22] E. N. Marieb and K. Hoehn, *Human Anatomy & Physiology*, Pearson International Edition, 2007.
- [23] <http://www.itis.ethz.ch/itis-for-health/tissue-properties/database/database-summary>.
- [24] A. Kraszewski and G. W. Hartsgrrove, "A macroscopic model of lungs and a material simulating their properties at radio and microwave frequencies," *Journal of Microwave Power and Electromagnetic Energy*, vol. 21, no. 4, pp. 233–240, 1986.
- [25] P. Gajšek, W. D. Hurt, J. M. Ziriach, and P. A. Mason, "Parametric dependence of SAR on permittivity values in a man model," *IEEE Transactions on Biomedical Engineering*, vol. 48, no. 10, pp. 1169–1177, 2001.
- [26] A. Peyman, C. Gabriel, E. H. Grant, G. Vermeeren, and L. Martens, "Variation of the dielectric properties of tissues with age: the effect on the values of SAR in children when exposed to walkie-talkie devices," *Physics in Medicine and Biology*, vol. 54, no. 2, pp. 227–241, 2009.
- [27] A. Christ, M. C. Gosselin, M. Murbach et al., "Age dependent changes in SAR and temperature distribution induced in the user's head by cellular phones," in *BEMS Annual Meeting*, p. 131, San Diego, Calif, USA, 2008.
- [28] M. Cavagnaro, S. Pisa, and E. Pittella, "Safety aspects of people exposed to ultra wideband radar fields," *International Journal of Antennas and Propagation*, vol. 2013, Article ID 291064, 7 pages, 2013.
- [29] S. Pisa, P. Bernardi, M. Cavagnaro, E. Pittella, and E. Piuze, "A circuit model of an ultra wideband impulse radar system for breath-activity monitoring," *International Journal of Numerical Modelling: Electronic Networks, Devices and Fields*, vol. 25, no. 1, pp. 46–63, 2012.

Research Article

Analysis and Design of Magnetic Shielding System for Breast Cancer Treatment with Hyperthermia Inductive Heating

Chanchai Thongsopa and Thanaset Thosdeekoraphat

School of Telecommunication Engineering, Suranaree University of Technology, Thailand

Correspondence should be addressed to Chanchai Thongsopa; chan@sut.ac.th and Thanaset Thosdeekoraphat; thanaset@sut.ac.th

Received 27 June 2013; Revised 21 September 2013; Accepted 25 September 2013

Academic Editor: Soon Yim Tan

Copyright © 2013 C. Thongsopa and T. Thosdeekoraphat. This is an open access article distributed under the Creative Commons Attribution License, which permits unrestricted use, distribution, and reproduction in any medium, provided the original work is properly cited.

An analysis and design of magnetic shielding system are presented for breast cancer treatment with hyperthermia inductive heating. It is a technique to control magnetic field intensity and relocate the heating area by using a rectangular shielding with aperture. The distribution of the lossy medium was analyzed using the finite difference time domain method. Theoretical analyses investigate whether a novel shielded system is effective for controlling the magnetic field distribution or heating position. Theoretical and experimental investigations were carried out using a lossy medium. The inductive applicator is a ferrite core with diameter of 7 cm, excited by 4 MHz signal and a maximum output power of 750 W. The results show that size of heating region can be controlled by varying the aperture size. Moreover, the investigation result revealed that the position of heating region can be relocated by changing the orientation of the ferrite core with shielded system in x -axis direction. The advantage of the magnetic shielding system is that it can be applied to prevent the side effects of hyperthermia cancer treatment by inductive heating.

1. Introduction

At present, cancer is one of leading causes of population death worldwide. Cancer is the uncontrolled growth and spread of cells. It can affect almost any part of the body, especially breast cancer because breast cancer has been increasing worldwide every year. Therefore, it is desirable to remove the cancer from the human body as soon as possible. Cancer can be treated effectively by various methods such as surgical excision, chemotherapy, and radiotherapy including hyperthermia [1–5] which is one of noninvasive techniques. The demands for noninvasive cancer treatment by hyperthermia heating are rapidly growing [6–13]. There are few techniques for noninvasive deep hyperthermia [14–17]. Most of microwave heating methods could not be used for deep hyperthermia due to skin depth effect. Low frequency technique is possible for deep treatment, though. The temperature in a cancer cell can be increased by induction [18–26]. To induce heat in the cancer cell, strong magnetic field has to penetrate the cancer cell to generate eddy current in the cell which can be visualized as electric loss. The eddy current will increase the cell temperature. The temperature of normal

cells due to eddy current is constant since the cancer cell is lower than conductive than normal cell. Nevertheless, the direction of magnetic field is important for localizing the heating region. Because of high intensity magnetic field will have side effects on neighbouring normal cells, which can be devastating to normal cells [27, 28]. A magnetic shielded system has become an important topic for hyperthermia inductive heating because it can reduce the side effects on neighbouring normal cells from magnetic field.

Moreover, the magnetic field intensity is crucial for hyperthermia treatment since it controls tissue temperature. It has been shown that magnetic core orientation and position can control the field distribution in both horizontal and vertical directions [29]. To concentrate magnetic field in a specific region, a shielding system was installed at the magnetic core. The location of heating can be controlled by moving the ferrite core. The shielding system in [29] utilizing two metal plates to control the vertical magnetic field to controlling heating position. One metal plate was placed between two ferrite cores, and the other two metal plates were placed close to the ferrite cores. This configuration provides control over the vertical field, and hence, the heating location

can be determined by the ferrite cores location. However, the magnetic field will leak through the unshielded side of the ferrite cores. The leakage of magnetic field results in difficulty of controlling the heating area and also affects normal cells nearby. Radiotherapy for breast cancer requires regional heating with specific temperature [30]. The temperature is directly proportional to magnetic field intensity.

In this paper, we presented an analysis and design of magnetic shielding system for breast cancer treatment with hyperthermia inductive heating. This paper will analyze the effects of magnetic shielded system on heating area and location of induction heating for breast cancer hyperthermia treatment; what the articles presented here consists of numerical simulations and experiments. The distribution of the lossy medium was analyzed using the finite difference time domain method. The inductive applicator is a ferrite core with diameter of 7 cm, excited by 4 MHz signal and a maximum output power of 750 W. These theoretical and experimental investigations were carried out using an agar phantom. It is difficult to limit heating area when the applicator's ferrite cores are unshielded. The results show that the size of heating region can be controlled by varying the aperture size of the shielded system. However, the heating efficiency is reduced as the aperture size decreases. If the small heating area is needed, it may require longer treatment time. In addition, the heating location can be varied by changing ferrite core orientation. By moving the orientation of the ferrite core in x -axis direction, the heating location and area were altered dramatically for unshielded ferrite cores, whereas the heating position and area are slightly different for shielded cores. The results show that the heating position can be relocated from the left to the right of the agar phantom by changing the orientation of the ferrite core with shielded system. The cores' vertical position has almost no effect on the heating area and position for shielded cores. In contrast, heating area and position are difficult to predict when unshielded cores are used. The proposed magnetic field shielding system is suitable for preventing the side effects of hyperthermia cancer treatment by induction heating.

2. Concept and Construction of Shielding System

The proposed magnetic shielding system consists of two rectangular shielding plates as shown in Figure 1. The shielding system in [29] consists of a metal plate to control the magnetic field from a single side of the core. Unlike the regional heating system in [29], the proposed shielding system controls the vertical by enclosing the ferrite core with a rectangular shield with aperture. Since placing the shielding plate at only one side of the ferrite core in [29] can control the magnetic field of only one side, it will cause magnetic field leak in the opposite side of the shielding plate. Thus, it is difficult to control the heating area. This magnetic field leakage results in spreading of the heating region that has an effect on other nearby tissues.

In this figure, a two-dimension cross-section of the analytic region is represented in order to easily understand the configuration of the shielding system analysis. The proposed

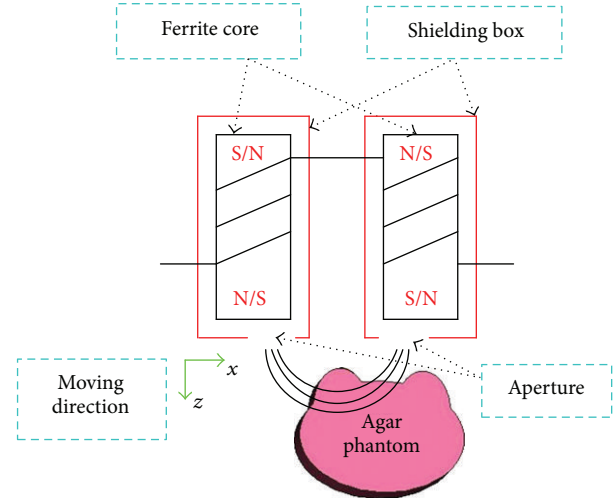


FIGURE 1: Schematic of shielding system. The shielding system consists of two rectangular shielding plates and controls the vertical by enclosing the ferrite core with a rectangular shield with aperture.

shielding system limits the magnetic field around the ferrite cores to confine the field in the horizontal direction. Most of the vertical magnetic field will penetrate into the heating body via the aperture, and hence the heating region size can be determined by the aperture size. Moreover, the heating position which can be relocated from the top to the bottom and the left to the right of the breast by moving the orientation of the ferrite core with rectangular shield in x -axis direction is illustrated in Figure 1. In addition, the design of magnetic field shielding system is necessary to take into consideration the attenuation of the magnetic field properties of the various materials used in order to spread the magnetic field over the specific area and leakage of magnetic field to the nearby areas to the fewest.

A major shielding technique used to reduce the magnetic field was divided into two ways as follows. Ferromagnetic shields give good results for small and closed shields, and they also give large field attenuation at close range to the source for open shield geometries. Highly conductive materials, on the other hand, are found to be suitable for large shield sizes. The attenuation is, however, reduced in the close vicinity of the source. In this investigation, we have selected a highly conductive material to studies, and their different materials are shown. We can regard the magnetic field as a result of the electric current flow and the magnetization of surrounding materials. The magnetic field is excited by source currents carried by conductors of various geometries. With a highly conductive shield, eddy currents arise in the metal. These currents create a field opposing the incident field. The magnetic field is in this way repulsed by the metal and forced to run parallel to the surface of the shield, yielding a low flux density outside the metal [31, 32]. Therefore, we have to consider effects of magnetic field shielding of various materials that were tested, such as copper (Cu), lead (Pb), steel (Fe), and transformer steel (Ck-37), which have

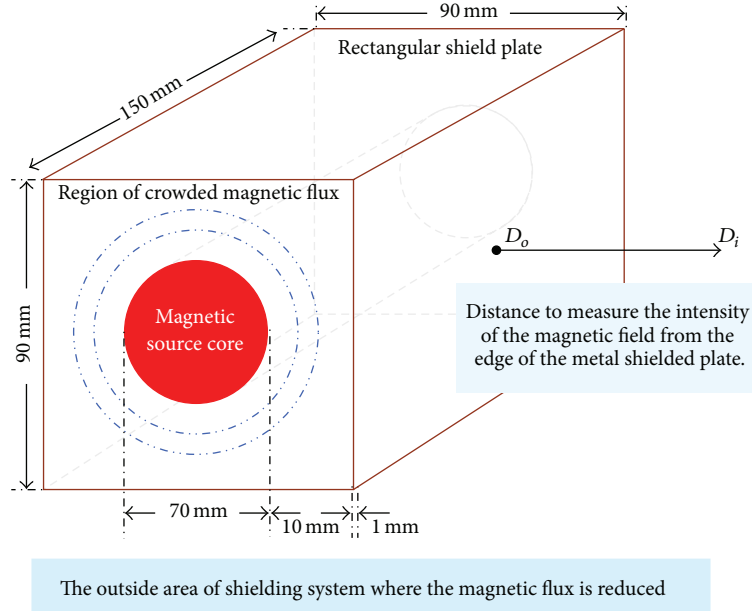


FIGURE 2: Schematic of rectangular shield plate and distance to measure the intensity of the magnetic field. The material used in the analyses consists of copper, lead, steel, and transformer steel (D_o is the edge of metal shield plate, and D_i is the distance of magnetic field which is reduced).

TABLE 1: Properties of various materials.

Materials	Conductivity (S/m)	Permeability
Copper (Cu)	59.6×10^6	1
Steel (Fe)	7.14×10^6	700
Lead (Pb)	4.55×10^6	1
Transformer steel (Ck-37)	2.17×10^5	4000

conductivity, relative permeability, and relative permittivity and are illustrated in Table 1.

The investigation of the effective reduction of the magnetic field for various materials was carried out in the study. To analyse the effectiveness of magnetic field shielding of materials, we specify a current source of the magnetic field (J_s) of 1 A/m^2 . The dimensions and schematic details of the shielding plate for analyzing the magnetic field intensity of various materials are shown in Figure 2.

Figure 2 represents the model of rectangular shield plate and distance to measure the intensity of the magnetic field [31, 33]. After that, we analyzed the effectiveness of magnetic field shielding (SE) of various materials in the following equation [34]. The shielding results are all given for a shield thickness of 1 mm at the frequency of 4 MHz. Consider,

$$SE \text{ (dB)} = 20 \log \left[\frac{H_{\text{unshield}}}{H_{\text{shield}}} \right], \quad (1)$$

where H_{unshield} is the rms flux density without shield plate and H_{shield} is the rms flux density with shield plate. Analysis of the effective shielding of magnetic field in our study is illustrated in Figure 3. The material used in the analyses consists of copper, lead, steel, and transformer steel, as mentioned above.

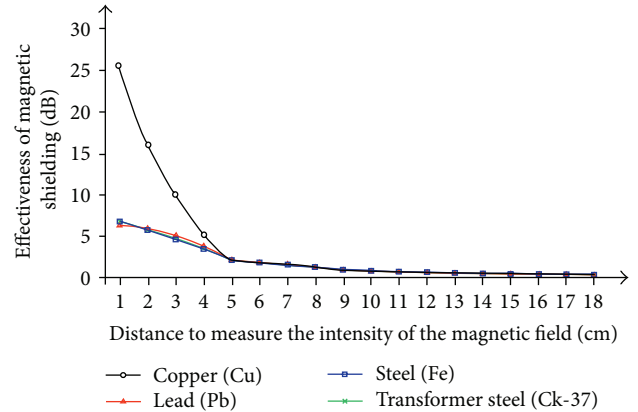


FIGURE 3: The effectiveness of magnetic field shielding of various materials that were tested. The horizontal axis represents the distance of the rectangular shielding plate, and the vertical axis shows the effectiveness of the shielding for various materials.

Figure 3 represents the effectiveness of magnetic field shielding of various materials that were tested. The horizontal axis represents the distance from the edge of the rectangular shielding plate, and the vertical axis shows the effectiveness of the shielding for various materials. The analysis found that the copper materials will be provided the most effective shield of approximately 25.47 dB. Therefore, we chose copper as the material used for the analysis and design of magnetic shielding system. Copper is a material that can be reduced to a maximum magnetic field in order to study the characteristics of magnetic field shielding system which are applied with various aperture sizes to control the magnetic field density

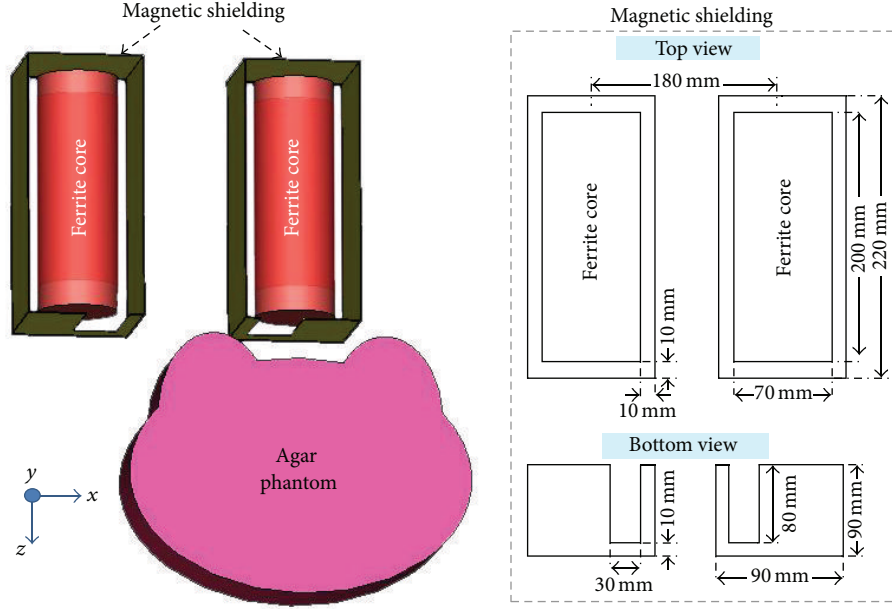


FIGURE 4: Analytical model of magnetic field shielding system, which represented the parameter details of the ferrite core and magnetic shielding plate for an analysis of electric loss density and temperature distribution.

and heating position appropriately. The schematic of the analytical model of magnetic field shielding system is shown in Figure 4.

Figure 4 represents the heating model which is made from agar phantom (the phantom model size is equal to 25 × 20 cm) with conductivity, relative permeability, and relative permittivity of 0.62 S/m, 1, and 130, respectively. A phantom simulating a human breast was placed between a pair of ferrite cores with magnetic shield (the parameter details of ferrite cores and shielding plate are shown in Figure 4). The distance between both ferrite cores is equal to 18 cm, by selected from a distance at the magnetic field were reduced the most from consideration of shielding plate design in Figure 3 mentioned above. The magnetic shield plate is a rectangular metal with conductivity of 59.6e6 S/m. The ferrite core is a highly magnetic material with 0.001 S/m conductivity and relative permeability at 200.

3. Analysis of Temperature Distribution

To determine a method of heating induction and controlling heating position, we solved Maxwell's equation and analyzed by using the three-dimensional finite difference time domain method [35–40] the following equations [41–46]:

$$\begin{aligned}\nabla \times E &= -j\omega\mu H, \\ \nabla \times H &= J_0 + j\omega\epsilon E + \sigma E,\end{aligned}\quad (2)$$

where E is the electric field, H is the magnetic field (A/m), ω is the radian frequency, μ is the permeability, J_0 is the forced current density (A/m²), ϵ is the permittivity, and σ is the electrical conductivity (S/m). In this analysis, the following fundamental equation for vector potential A , which takes the

eddy current into consideration, is used [28, 45]. Solving the following equation for A , the magnetic field and eddy current distribution are calculated as follows:

$$\begin{aligned}\nabla \times (\nu \nabla \times A) &= J_0 - J, \\ \nabla \times (\nu \nabla \times A) &= J_0 - \sigma \frac{\partial A}{\partial t} - \sigma \nabla \phi,\end{aligned}\quad (3)$$

where ν , J , and ϕ represent the magnetic reluctance, and the current density (A/m²) can be calculated from magnetic field and the electric potential (V), respectively. In the electromagnetic analysis, we derive the lowest resonant frequency of the applicator. Subsequently, the temperature distributions are observed. The temperature changes depend on the output power from the high power oscillator into the applicator systems and treatment time. The power losses in the lossy medium can be calculated from the relationship of the magnetic field and current density. Moreover, we can control the heating temperature from the external power into the applicator systems. The temperature distribution in lossy media can be calculated from bioheat transfer equation by assuming that the lossy media is human tissue or breast replica. It can be expressed as [25, 47–54]

$$\frac{\partial T}{\partial t} = R_T \nabla^2 T + \frac{\epsilon_v}{C_p} L_h \left(\frac{\partial M_l}{\partial t} \right) + \frac{P}{\rho C_p}, \quad (4)$$

$$P = J \cdot J^*, \quad (5)$$

$$J = -\sigma \frac{\partial A}{\partial t} - \sigma \nabla \phi, \quad (6)$$

$$R_T = \frac{k_t}{\rho C_p}, \quad (7)$$

TABLE 2: Evaluating the electric loss density from changing the aperture sizes.

Aperture sizes of shield plate (cm)	Electric loss density (W/m^3)	Temp. ($^{\circ}C$)	Magnetic flux density (A/m)	Effectiveness of magnetic field shielding (dB)
Without shielding	295	70.5	433	—
10	174	41.6	309	2.93
9	169	40.4	295	3.33
8	154	36.8	279	3.82
7	148	35.4	278	3.84
6	134	32.0	276	3.91
5	132	31.5	275	3.94
4	129	30.8	273	4.00
3	108	25.8	271	4.07

where T is the temperature ($^{\circ}C$), t is the heating time (s), R_T is the distribution temperature ($m^2 \cdot s^{-1}$), ε_v is the liquid water flow ratio to the moisture transfer (kg^{-1}), C_p is the specific heat capacity of an object ($4.18 J \cdot kg^{-1} \cdot ^{\circ}C^{-1}$), L_h is the latent heat of vaporization ($kJ \cdot kg^{-1}$), M_l is the mass of liquid (kg), P is the heat source of distribution ($W \cdot m^{-3}$) calculated from current density of magnetic field, and ρ is the local physical density of tissue ($1000 g \cdot m^{-3}$). The simulation of induction heating was conducted by analyzing eddy current distribution of the inductive applicator which is a ferrite core, and it will be discussed in the next section.

4. Numerical Results

In this section, we investigate the magnetic flux density, which can be controlled by varying the aperture size. In order to resolve the problem of heating region local heating can be controlled by varying the aperture size of the shielded system. Moreover, the investigation showed that the position of heating region can be relocated by changing the orientation of the ferrite core with shielded system in x -axis direction. For the construction of magnetic shielding system to verify the field distribution on the heating model, full wave 3D numerical simulation was performed using finite difference time domain method.

4.1. Evaluating Electric Loss Density. To find out how to control the magnetic flux and heating region, we will change aperture size to get the most excellent heating efficiency, while causing smallest magnetic flux leakage to another nearby tissue. The proposed shielding system limits the magnetic flux around the ferrite cores to confine the field between two ferrite cores. It is a technique to control magnetic field intensity and relocate the heating area by using a rectangular metal shielding with aperture. The demonstration shows that the magnetic field intensity can be regulated by varying the aperture size.

From these theoretical investigations, one effective method to control a heating region in the breast was found. Hence, the temperature in the heating body can be controlled by the size of shielding aperture. Electric loss density for the heating model was evaluated. The ferrite core is excited

by 4 MHz signal. The aperture sizes in the simulation are 5 cm, 7 cm, and 8 cm. Electric loss density images for heating region of the ferrite core without shield and with rectangular shield with all aperture sizes are shown in Figure 5.

Figure 5 represents the heating region of the ferrite cores with and without rectangular shield. The heating region has spread over the large area when the ferrite core is unshielded with rectangularly shield as shown in Figure 5(a). When the ferrite core is rectangularly shielded with various aperture sizes, the heating region size is confined in smaller area as shown in Figures 5(b)–5(d), but in Figures 5(e) and 5(f) the heating region size began to spread in wide area. It is difficult to limit or control heating area when the ferrite cores with shielding plate have the large aperture size. The heating region size is reduced when the aperture size is smaller. It can be seen that the heating region is controlled by varying the aperture size as illustrated in Table 2. The results in Table 2 are expressed in terms of the electric loss density. However, replacing the electric loss density mentioned above into the last term of (4), the heating temperature in Celsius degrees unit per time will be obtained. For example, the aperture size of 8 cm when changing the value of electric loss density from $154 W/m^3$ to the form of temperature will be equal to 36.84 Celsius degrees. Nevertheless, in experiment and measurement result if the small heating area is needed, it may require longer treatment time. More treatment time may be required to heat the cancer cell to the desired temperature.

The simulations show that the heating area can be effectively controlled by using the rectangular shield with adjustable aperture size as mentioned above in Table 2. The heating area was determined by the aperture size of the rectangular shield because the heating area is proportional to the aperture size. In unshielded cores, the heating area spreads unpredictably, and, hence, it is difficult to limit the heating area when the cores are unshielded. Simulations show that the heating area can be controlled by the aperture size of rectangular shield. In contrast, heating area is difficult to predict when unshielded cores are used. From Table 2, we found that the aperture size of 8 centimeters can perform the best results because the electric loss density is high. Furthermore, it can control the leakage of the magnetic field or the effectiveness of magnetic field shielding (SE) more effectively [33]. Considering the results of Table 2 shows that

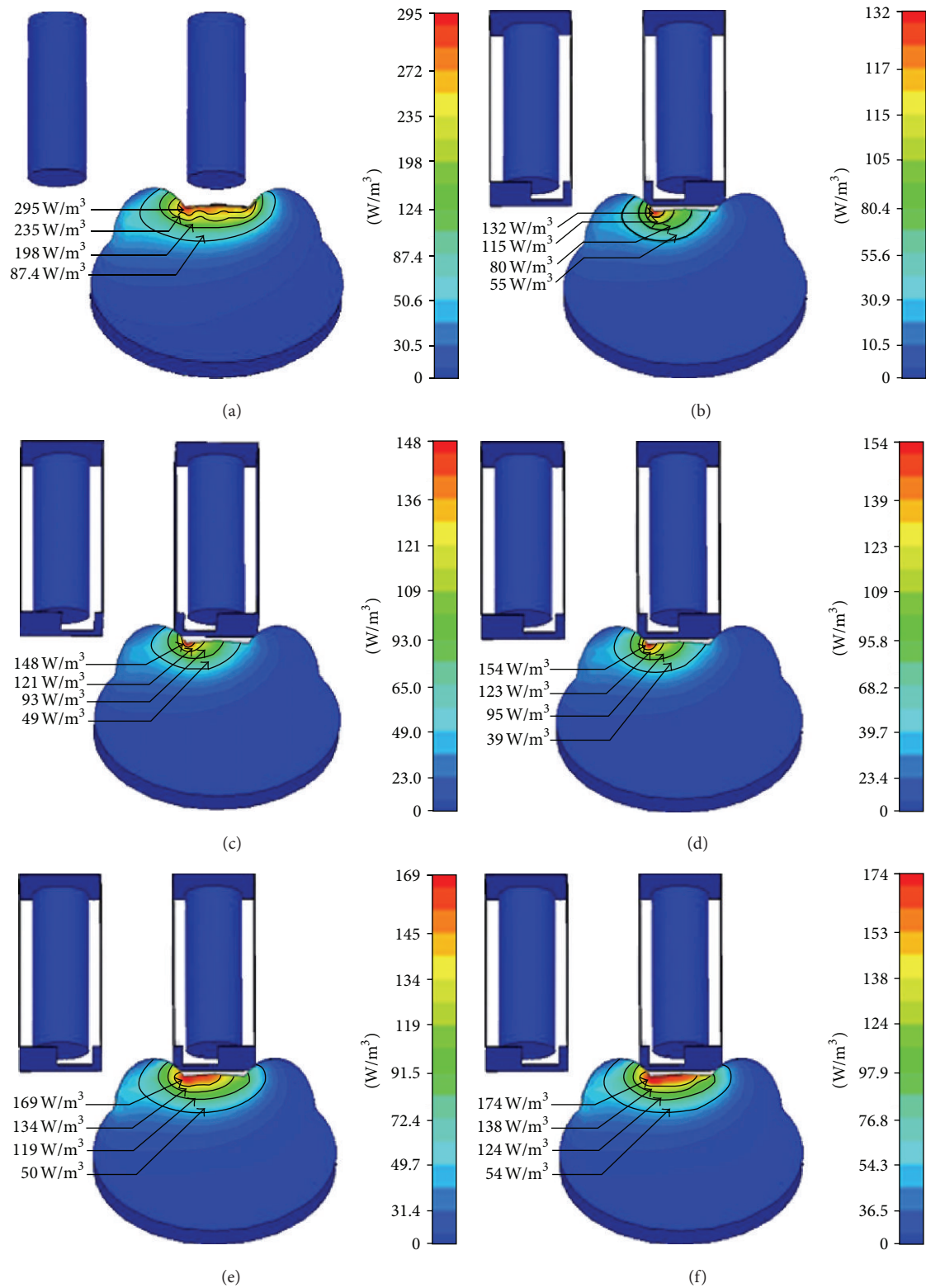


FIGURE 5: Electric loss density of the heating model for (a) ferrite core without shielding, (b) rectangular shielding with 5 cm aperture, (c) rectangular shielding with 7 cm aperture, (d) rectangular shielding with 8 cm aperture, (e) rectangular shielding with 9 cm aperture, and (f) rectangular shielding with 10 cm aperture.

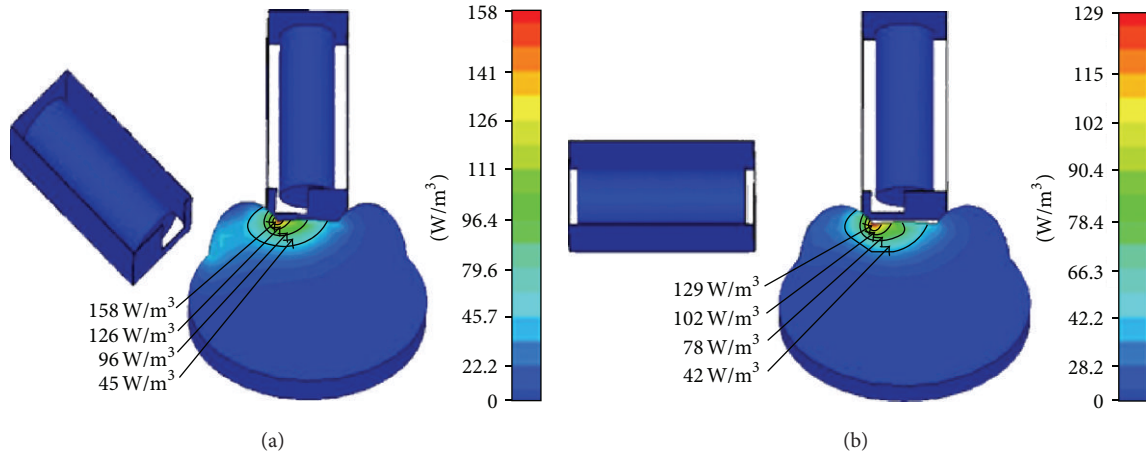


FIGURE 6: Electric loss density of the heating model for ferrite cores orientations (a) 45 degrees (b) 90 degrees.

the aperture sizes of 9 and 10 centimeters the electric loss density are having highly values. But it is difficult to limit or control heating area when the ferrite cores with shielding plate have the large aperture size. So we selected the aperture size of 8 cm which can perform the best results because the electric loss density is high. Furthermore, it can control the leakage of the magnetic field or the effectiveness of magnetic field shielding (SE) more effectively.

4.2. Investigating the Heating Orientation. We further investigated the heating location by changing shielded ferrite cores orientation. The ferrite cores changing the angle orientation are investigated as shown in Figure 6. For investigated the heating location by changing shielded ferrite cores orientation from original cores orientation (0-degree) to 90-degree. By investigated the electric loss density or heating distribution, it will be changing the angle orientation of the ferrite core in the left hand each once equal to 5 degrees. Which in Figure 6, we have shown only two positions is 45 degrees and 90 degrees. From changing the angle orientation of the ferrite core with shielding system at 45 degrees it was found that the electric loss density is the most valuable. Furthermore, the effect of distance of the ferrite core was investigated in x -direction to the heating location. The result shows that the heating location can be relocated by changing the position of the ferrite core with rectangular metal shield as shown in Figure 7.

Figure 6 shows the heating region for the ferrite 45-degree and 90-degree core orientation. In the shielded cores, the aperture size is 3×8 cm in the simulation for both orientations. The maximum electric loss densities for the 45-degree and 90-degree orientation are 158 W/m^3 and 129 W/m^3 , respectively. The maximum electric loss density for the 45-degree orientation is more than that for the parallel ferrite core configuration. In contrast, the electric loss density is lower for the parallel ferrite core configuration with 90-degree orientation. Moreover, the simulation results in Figure 7 show that the heating locations can be relocated from the left to the right of the breast model by

changing the orientation of the ferrite core with rectangular shields in x -direction. The maximum electric loss density for the orientation of the both ferrite cores with rectangular shields which changed from original position to the 8 cm is 150 W/m^3 . Further, the maximum electric loss density for the orientation of both ferrite cores with rectangular shields which changed from original position to 16 cm is 155 W/m^3 . In this case, the heating efficiency is similar for both positions and for the original position in Figure 5(d) since the aperture size is identical.

5. The Heating Experiment and Measurement Results

To control the heating area and heating position, the magnetic field distributions near the breast were analyzed using the full wave 3D numerical simulation. Magnetic shielding systems with a rectangular shield with aperture were introduced to control the magnetic field and examine its shield effect. The proposed shielding system limits the magnetic field around the ferrite cores to confine the field in horizontal direction. Most of the vertical magnetic field will penetrate into the heated breast via the aperture. The construction of applicator and shielding system for verifying the numerical and simulation results is illustrated in Figure 8.

Figure 8 shows the construction of magnetic shielding system to verify the field distribution on the heating model. Shield effect of the magnetic flux density was investigated. The proposed magnetic shielding system analysis consists of high power oscillator, applicator, and agar phantom. The first part is a high power oscillator, which consists of source excited by 4 MHz signal and power amplifier. The second part is the applicators, which includes Ni-Zn type ferrite cores covered with rectangular shielding box with aperture sizes in the examination of 8 cm system model. The demonstration revealed that we can control the magnetic flux intensity and relocate the heating area by using a rectangular metal shielding with aperture. The third part is the agar phantom; it has an elliptic cylinder-like shape with a pair

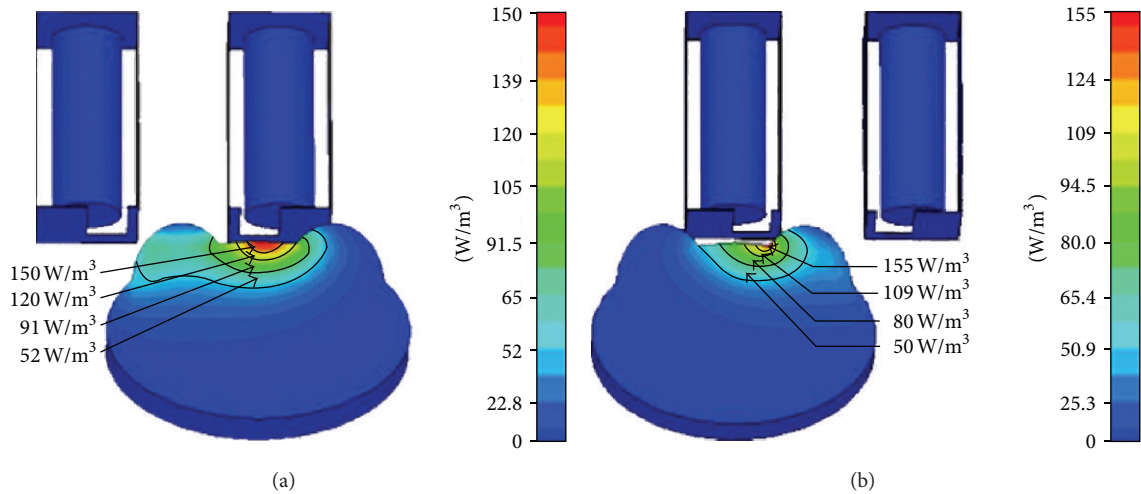


FIGURE 7: Electric loss density of the heating model for changing both ferrite cores with rectangular shields in x -direction. (a) The orientation of both ferrite cores with rectangular shields changed from original position to the 8 cm and (b) the orientation of both ferrite cores changed from the original position to 16 cm.

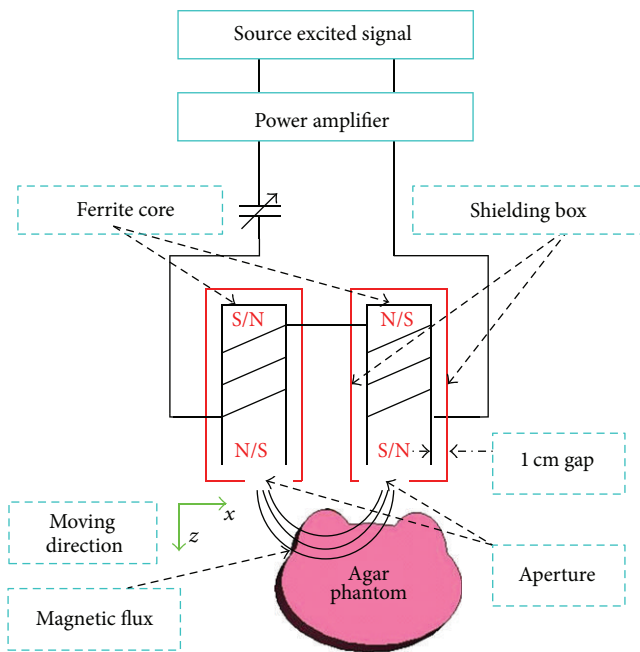


FIGURE 8: The construction of applicator and shielding system for verifying the numerical and simulation results.

of protuberances for the breasts model. The dimensions of the longer and shorter axes of the elliptic cylinder are 30 and 20 cm, respectively. The properties of the agar phantom or artificial breasts are presented in Section 2, as already mentioned above. An agar phantom subject to the guideline assigned by the Quality Assurance Committee, Japanese Society of Hyperthermia Oncology (QAC, JASHO) was used instead of the breast. During the inductive heating, it is obviously defined according to the heating principle that only a conductive material with loss is well heated.

For the treatment of cancer by using magnetic fields, the applicator must be designed for use in spreading or induction of magnetic field. Because the cancer treatment is performed with hyperthermia inductive heating, a coil applicator is needed. A ferrite core applicator system for hyperthermia was first proposed by one of the authors to achieve effective heating and to solve irradiation problems. Since then, several kinds of ferrite core applicators have been studied and developed [11–15]. By introducing a ferrite core for the inductive applicator, a magnetic field can be concentrated between a pair of poles. Accordingly, local or regional heating becomes possible with a relatively low input power, and irradiation around the applicator is decreased, compared to the same kind of inductive applicator, which is also agreeable from the viewpoint of electromagnetic compatibility (EMC).

In this paper, the design of the induction coil or an applicator, which the applicator above mentioned is ferrite core types of 2 poles. The equation could be good series resonance in order to determine the answer by the frequency of 4 MHz. The basic principle of the series inductor, which is the total value of inductor, is equal to the sum of both inductors as shown in Figure 9.

Figure 9 shows that a typical series inductance of the inductor value is equal to the sum of the total values of each inductor. The resonance frequency is $L_t = L_1 + L_2$. The winding number of each pole coil is N turns and adjusts the value of the capacitor to be in good resonance, in which the capacitor value is C . The resistance is approximately 0 ohms so that the resonant circuit gets the most excellent efficiency. Furthermore, it helps in easily understanding analysis and design of the induction coil or an applicator. The induction coils as above will spread the magnetic field between both poles. The magnetic flux moves back and forth alternately between the two poles, in which the abovementioned spread is the alternating magnetic field. In this paper we define resonance frequency of 4 MHz and the number of pole coils

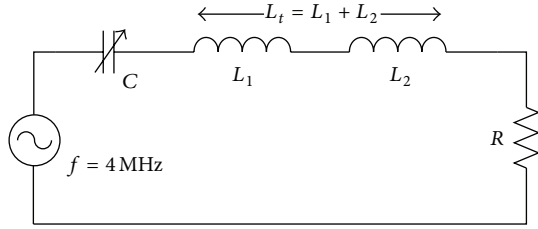


FIGURE 9: The RLC resonance equivalent circuits with the two inductors being connected in series. The resonance frequency is 4 MHz and the two pole coils are connected in series in conditions of resonance, it will have a total inductance is $L_t = L_1 + L_2 = 1918.96 \mu\text{H}$ and adjusts the value of the capacitor to be in good resonance, in which the capacitor value is $C = 0.825 \text{ pF}$.

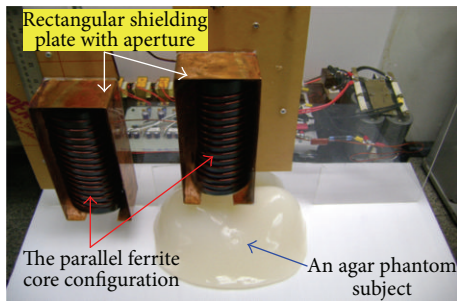


FIGURE 10: Constructions of shielding system for verifying the numerical and simulation results, in which the experiment of proposed system consists of high power oscillator, induction coils applicator with shielding plates, and agar phantom. The distance between both ferrite cores is equal to 18 cm from consideration of shielding plate design mentioned above.

in two series, in which the resonance frequency of the total inductor coil value is $L_t = L_1 + L_2 = 1918.96 \mu\text{H}$. The copper wire for inductive coil applicator design is number 13-SWG, which has cross-sectional area equal to 4.15 mm.

The winding number of each pole coil is 14 turns and adjusts the value of the capacitor to be in good resonance, in which the capacitor value is $C = 0.825 \text{ pF}$ as shown in Figure 10. The construction of parallel ferrite cores and rectangular shielding plates with aperture is shown. To examine these theoretical results of heating characteristics, a heating experiment was conducted. The magnetic field intensity around the ferrite cores will be limited by shielding system to confine the field in horizontal direction. Most of the vertical magnetic field will penetrate into the heating agar phantom via the aperture. The experiment of proposed system consists of high power oscillator, induction coils applicator with shielding plates, and agar phantom. The agar phantom used for the experiment is the same substance.

Figure 10 shows the construction of magnetic shielding system for breast cancer treatment with hyperthermia inductive heating. The paper experiments presented here consist of high power oscillator, induction coil applicator with shielding plates, and agar phantom. It is the experimental construction of magnetic shielding system that verifies the field distribution on the heating model. These theoretical

and experimental investigations were carried out using an agar phantom. The magnetic flux density and its shield effect were investigated. The inductive applicator is a ferrite core with diameter of 7 cm and length of 20 cm, excited by 4 MHz signal, and high power oscillator has maximum output power of 750 W (input voltage is 50 V and input current is 15 A). The distance between both ferrite cores is equal to 18 cm, considering the shielding plate design in Section 2.

To examine these heating characteristics, a heating experiment was conducted. The experimental method is the same as the case mentioned above in numerical section. Figure 11 shows an experimental result of the temperature characteristics for heating region and changing distance from the initial positions of the ferrite cores. It is suggested that the magnetic shield plate plays an important role in controlling the heating region and heating position. In this experiment, the temperature distribution or the distribution of heat in the breast model can be measured by using thermograph to measure the heat value inside the breast model. After magnetic field energy flows through the lossy medium or breast model for 20 minutes, we will stop generating magnetic field (in order to prevent the magnetic field from the excited source to disturb with the thermograph used for thermal imaging). Subsequently, the temperature distribution was observed by using a thermograph (FLIR SYSTEMS Model T360).

The experiment results of the temperature distributions when the ferrite cores applicator is without shielding plates are shown in Figure 11(a). The temperature distributions at the starting position when the ferrite cores applicator is with shielding plates at the original position and the temperature distributions in the cross-section are illustrated in Figures 11(b) and 11(c), respectively. The experiment results of the temperature distributions when ferrite cores applicator with shielding plates offsets from original position in the x -direction by a value equal to 16 cm are illustrated in Figure 11(d).

Figure 11(a) shows the temperature distributions of the ferrite cores' applicator without shielding plate. Figures 11(b) and 11(c) represent the experimental result of the temperature distributions at the initial positions of the ferrite cores with shielded plates and the temperature distributions of the ferrite cores with shielded plates in the cross-section, respectively. Further, Figure 11(d) represents the temperature distributions when the ferrite cores applicator offsets from initial positions in the x -direction by a value equal to 16 cm. The maximum value of temperature of 45.5°C , 45.1°C , 44.9°C , and 45.8°C is shown in Figures 11(a)–11(d), respectively; it is the temperature at the cursor position. The temperature of the thermograph imaging camera setting at the starting position is in the range of 20°C to 46°C , in which the magnetic energy was generated by the high power oscillator of 750 W, excited by 4 MHz signal. The white portion near the breast in these figures represents the highest temperature. It was found that these heating characteristics demonstrate the theoretical results. The experimental result of the temperature distributions observed by using a thermograph which is consistent with the numerical calculations results. The electric loss density of the heating model is a part of the magnetic

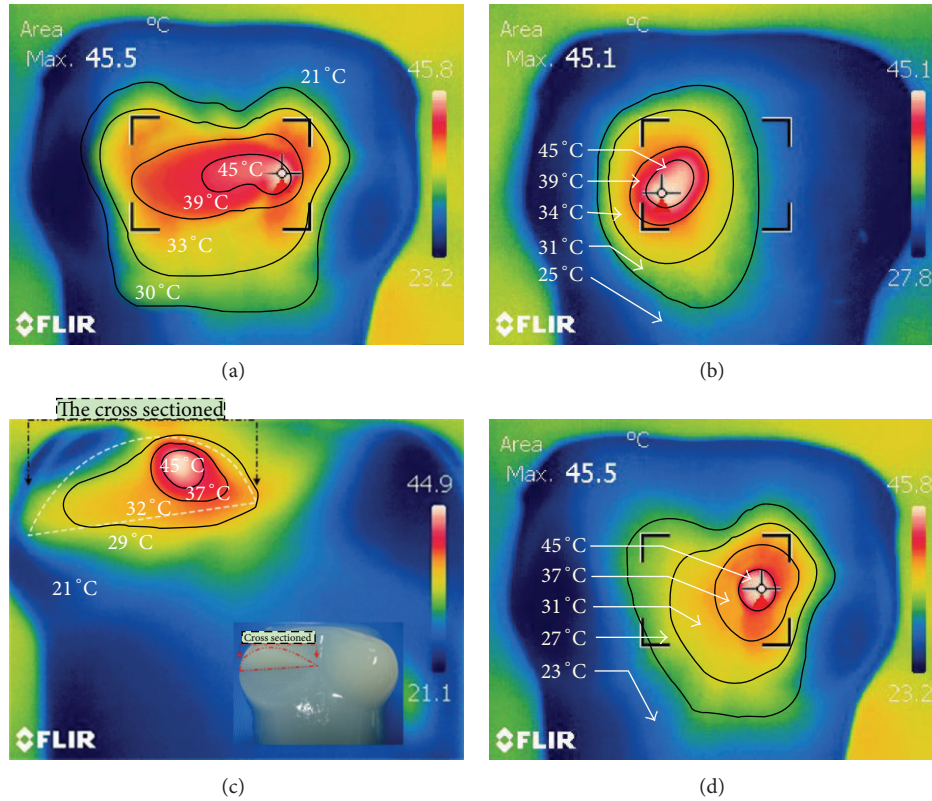


FIGURE 11: The temperature of the agar phantom: (a) the temperature distributions for the ferrite cores applicator without shielding plates, (b) the temperature distributions with shielding plates at the original position, (c) the temperature distributions in the cross-section, and (d) the temperature when the ferrite cores applicator offsets from original position in the x -direction by a value equal to 16 cm.

field energy from the external source excited by 4 MHz signal because the energy of the external electromagnetic field is directly proportional to the internal temperature of the breast model obtained from the thermograph imaging camera.

6. Conclusion

The effect of magnetic shielding system on heating area and the location for breast cancer treatment with hyperthermia inductive heating are presented. It is a novel technique to control magnetic field intensity and relocate the heating area by using a rectangular shielding with aperture. The distribution of the lossy medium was analyzed using the FDTD. From these investigations, we found that the aperture size of 8×3 centimeters could perform the best results because the electric loss density is high to equal, 154 W/m^3 . Furthermore, it can control the leakage of the magnetic field more effectively. In addition, the heating location can be varied by changing ferrite core orientation. The results show that the heating position can be relocated from the left to the right of the agar. Subsequently, the heating experiment was conducted. The inductive applicator is a ferrite core with diameter of 7 cm and length of 20 cm, excited by 4 MHz signal, and a maximum output power of 750 W. From heating experiment by using a thermograph, we found that the value of the temperature distribution in the breast model is approximately 45°C . The proposed magnetic field shielding

system is suitable to prevent the side effects of hyperthermia cancer treatment by inductive heating.

Acknowledgments

This work was supported by Suranaree University of Technology (SUT) and by the Office of the Higher Education under NRU project of Thailand. The authors deeply appreciate the valuable comments of the reviewers and recommends to be advantageous for revisions this paper.

References

- [1] E. Ben Hur, M. M. Elkind, and B. V. Bronk, "Thermally enhanced radiosensitivity of cultured Chinese hamster cells: inhibition of repair of sublethal damage and enhancement of lethal damage," *Radiation Research*, vol. 58, no. 1, pp. 38–51, 1974.
- [2] P. P. Antichi, N. Tokita, J. H. Kim et al., "Selective heating of coetaneous human tumors at 27.12 MHz," *IEEE Transactions on Microwave Theory and Techniques*, vol. 26, no. 8, pp. 569–572, 1978.
- [3] J. R. Oleson, "A review of magnetic induction methods for hyperthermia treatment of cancer," *IEEE Transactions on Biomedical Engineering*, vol. 31, no. 1, pp. 98–105, 1984.
- [4] I. Kimura and T. Katsuki, "VLF induction heating for clinical hyperthermia," *IEEE Transactions on Magnetics*, vol. 22, no. 6, pp. 1897–1900, 1986.

- [5] P. Charles and P. Elliot, *Handbook of Biological Effects of Electromagnetic Fields*, CRC Press, New York, NY, USA, 1995.
- [6] F. K. Storm, R. S. Elliott, W. H. Harrison, and D. L. Morton, "Clinical RF hyperthermia by magnetic-loop induction: a new approach to human cancer therapy," *IEEE Transactions on Microwave Theory and Techniques*, vol. 30, no. 8, pp. 1149–1158, 1982.
- [7] H. Kato and T. Ishida, "New inductive applicator for hyperthermia," *Journal of Microwave Power*, vol. 18, no. 4, pp. 331–336, 1983.
- [8] A. Rosen, M. A. Stuchly, and A. Vander Vorst, "Applications of RF/microwaves in medicine," *IEEE Transactions on Microwave Theory and Techniques*, vol. 50, no. 3, pp. 963–974, 2002.
- [9] V. A. Vander, A. Rosen, and Y. Kotsuka, *RF/Microwave Interaction With Biological Tissues*, Wiley-IEEE, New York, NY, USA, 2006.
- [10] P. R. Stauffer and S. N. Goldberg, "Introduction: thermal ablation therapy," *International Journal of Hyperthermia*, vol. 20, no. 7, pp. 671–677, 2004.
- [11] M. Hiraoka, M. Mitsumori, N. Hiroi et al., "Development of RF and microwave heating equipment and clinical applications to cancer treatment in Japan," *IEEE Transactions on Microwave Theory and Techniques*, vol. 48, no. 1, pp. 1789–1799, 2000.
- [12] Y. Kotsuka, E. Hankui, M. Hashimoto, and M. Miura, "Development of double-electrode applicator for localized thermal therapy," *IEEE Transactions on Microwave Theory and Techniques*, vol. 48, no. 1, pp. 1906–1908, 2000.
- [13] P. S. Ruggera and G. Kantor, "Development of a family of RF helical coil applicators which produce transversely uniform axially distributed heating in cylindrical fat-muscle phantoms," *IEEE Transactions on Biomedical Engineering*, vol. 31, no. 1, pp. 98–106, 1984.
- [14] Y. Kotsuka, "Development of ferrite core applicator system for deep-induction hyperthermia," *IEEE Transactions on Microwave Theory and Techniques*, vol. 44, no. 10, pp. 1803–1810, 1996.
- [15] Y. Kotsuka and H. Okada, "Development of small and high efficiency implant for deep local hyperthermia," *Japanese Journal of Hyperthermic Oncology*, vol. 19, no. 1, pp. 11–22, 2003.
- [16] V. D'Ambrosio and F. Dughiero, "Numerical model for RF capacitive regional deep hyperthermia in pelvic tumors," *Medical and Biological Engineering and Computing*, vol. 45, no. 5, pp. 459–466, 2007.
- [17] S. Kuroda, N. Uchida, K. Sugimura, and H. Kato, "Thermal distribution of radio-frequency inductive hyperthermia using an inductive aperture-type applicator: evaluation of the effect of tumour size and depth," *Medical and Biological Engineering and Computing*, vol. 37, no. 3, pp. 285–290, 1999.
- [18] J. H. Kim, E. W. Hahn, N. Tokita, and L. Z. Nisce, "Local tumor hyperthermia in combination with radiation therapy. I. Malignant cutaneous lesions," *Cancer*, vol. 40, no. 1, pp. 161–169, 1977.
- [19] R. S. Elliott, W. H. Harrison, and F. K. Storm, "Hyperthermia: electromagnetic heating of deep-seated tumors," *IEEE Transactions on Biomedical Engineering*, vol. 29, no. 1, pp. 61–64, 1982.
- [20] M. J. Hagmann and R. L. Levin, "Coupling efficiency of helical coil hyperthermia applications," *IEEE Transactions on Biomedical Engineering*, vol. 32, no. 7, pp. 539–540, 1985.
- [21] J.-L. Guerquin-Kern, M. J. Hagmann, and R. L. Levin, "Experimental characterization of helical coils as hyperthermia applicators," *IEEE Transactions on Biomedical Engineering*, vol. 35, no. 1, pp. 46–52, 1988.
- [22] P. Raskmark and J. B. Andersen, "Focused electromagnetic heating of muscle tissue," *IEEE Transactions on Microwave Theory and Techniques*, vol. 32, no. 8, pp. 887–888, 1984.
- [23] C. A. Tiberio, L. Raganella, G. Banci, and C. Franconi, "The RF toroidal transformer as a heat delivery system for regional and focused hyperthermia," *IEEE Transactions on Biomedical Engineering*, vol. 35, no. 12, pp. 1077–1085, 1988.
- [24] J. B. Anderson, A. Baun, K. Harmark et al., "A hyperthermia system using a new type of inductive applicator," *IEEE Transactions on Biomedical Engineering*, vol. 31, no. 1, pp. 212–227, 1984.
- [25] F. Dughiero and S. Corazza, "Numerical simulation of thermal disposition with induction heating used for oncological hyperthermic treatment," *Medical and Biological Engineering and Computing*, vol. 43, no. 1, pp. 40–46, 2005.
- [26] H. Rahn, S. Schenk, H. Engler et al., "Tissue model for the study of heat transition during magnetic heating treatment," *IEEE Transactions on Magnetics*, vol. 49, no. 1, pp. 244–249, 2013.
- [27] C. Polk and E. Postow, *Handbook of Biological Effects of Electromagnetic Fields*, CRC Press, Boca Raton, Fla, USA, 1996.
- [28] S. L. Ho, S. Niu, W. N. Fu et al., "Design and analysis of novel focused hyperthermia devices," *IEEE Transactions on Magnetics*, vol. 48, no. 11, pp. 3254–3257, 2012.
- [29] Y. Kotsuka, M. Watanabe, M. Hosoi, I. Isono, and M. Izumi, "Development of inductive regional heating system for breast hyperthermia," *IEEE Transactions on Microwave Theory and Techniques*, vol. 48, no. 1, pp. 1807–1814, 2000.
- [30] C. Thongsopa, A. Intarapanich, and S. Tangwachirapan, "Shielding system for breast hyperthermia inductive heating," in *Proceedings of the ISEF-XIV International Symposium on Electromagnetic Fields in Mechatronics, Electrical and Electronic Engineering*, Arras, France, September 2009.
- [31] L. Hasselgren and J. Luomi, "Geometrical aspects of magnetic shielding at extremely low frequencies," *IEEE Transactions on Electromagnetic Compatibility*, vol. 37, no. 3, pp. 409–420, 1995.
- [32] Y. Du, T. C. Cheng, and A. S. Farag, "Principles of power-frequency magnetic field shielding with flat sheets in a source of long conductors," *IEEE Transactions on Electromagnetic Compatibility*, vol. 38, no. 3, pp. 450–459, 1996.
- [33] Y. Kotsuka, H. Kayahara, K. Murano, H. Matsui, and M. Hamuro, "Local inductive heating method using novel high-temperature implant for thermal treatment of luminal organs," *IEEE Transactions on Microwave Theory and Techniques*, vol. 57, no. 10, pp. 2574–2580, 2009.
- [34] L. Hasselgren and J. Luomi, "Geometrical aspects of magnetic shielding at extremely low frequencies," *IEEE Transactions on Electromagnetic Compatibility*, vol. 37, no. 3, pp. 409–420, 1995.
- [35] D. Sullivan, "Three-dimensional computer simulation in deep regional hyperthermia using the finite-difference time-domain method," *IEEE Transactions on Microwave Theory and Techniques*, vol. 38, no. 2, pp. 204–211, 1990.
- [36] K. S. Kunz and R. J. Luebbers, *The Finite Difference Time Domain for Electromagnetics*, CRC Press, New York, NY, USA, 1993.
- [37] D. M. Sullivan, "A frequency-dependent FDTD method for biological applications," *IEEE Transactions on Microwave Theory and Techniques*, vol. 40, no. 3, pp. 532–539, 1992.
- [38] C. Thongsopa, M. Krairiksh, A. Mearnchu, and D.-A. Srimoon, "Analysis and design of injection-locking steerable active array applicator," *IEICE Transactions on Communications*, vol. E85-B, no. 10, pp. 2327–2337, 2002.
- [39] D. C. Dibben and A. C. Metaxas, "Finite element time domain analysis of multimode applicators using edge elements," *Journal*

- of *Microwave Power and Electromagnetic Energy*, vol. 29, no. 4, pp. 242–251, 1994.
- [40] S. Bharoti and S. Ramesh, “Simulation of specific absorption rate of electromagnetic energy radiated by mobile handset in human head using FDTD method,” *WSEAS Transactions on Communications*, vol. 2, pp. 174–180, 2003.
- [41] W. Renhart, C. A. Magele, K. R. Richter, P. Wach, and R. Stollberger, “Application of eddy current formulations to magnetic resonance imaging,” *IEEE Transactions on Magnetics*, vol. 28, no. 2, pp. 1517–1520, 1992.
- [42] A. Boadi, Y. Tsuchida, T. Todaka, and M. Enokizono, “Designing of suitable construction of high-frequency induction heating coil by using finite-element method,” *IEEE Transactions on Magnetics*, vol. 41, no. 10, pp. 4048–4050, 2005.
- [43] P. A. Bottomley and E. R. Andrew, “RF magnetic field penetration, phase shift and power dissipation in biological tissue: implications for NMR imaging,” *Physics in Medicine and Biology*, vol. 23, no. 4, pp. 630–643, 1978.
- [44] N. Kuster and Q. Balzano, “Energy absorption mechanism by biological bodies in the near field of dipole antennas above 300 MHz,” *IEEE Transactions on Vehicular Technology*, vol. 41, no. 1, pp. 17–23, 1992.
- [45] C. A. Balanis, *Advanced Engineering Electromagnetic*, Wiley, New York, NY, USA, 1989.
- [46] K. S. Yee, “Numerical solution of initial boundary value problems involving Maxwell’s equations in isotropic media,” *IEEE Transactions on Antennas and Propagation*, vol. 14, no. 3, pp. 302–307, 1966.
- [47] V. Mateev, I. Marinova, Y. Saito et al., “Coupled field modeling of Ferrofluid heating in tumor tissue,” *IEEE Transactions on Magnetics*, vol. 49, no. 5, pp. 1793–1796, 2013.
- [48] V. D’Ambrosio and F. Dughiero, “Numerical model for RF capacitive regional deep hyperthermia in pelvic tumors,” *Medical and Biological Engineering and Computing*, vol. 45, no. 5, pp. 459–466, 2007.
- [49] R. B. Roemer and T. C. Cetas, “Applications of bioheat transfer simulations in hyperthermia,” *Cancer Research*, vol. 44, no. 10, supplement, pp. 4788s–4798s, 1984.
- [50] S. M. Mimoune, J. Fouladgar, A. Chentouf, and G. Develey, “A 3D impedance calculation for an induction heating system for materials with poor conductivity,” *IEEE Transactions on Magnetics*, vol. 32, no. 3, pp. 1605–1608, 1996.
- [51] N. S. Doncov and B. D. Milovanovic, “TLM modeling of the circular cylindrical cavity loaded by lossy dielectric sample of various geometric shapes,” *Journal of Microwave Power and Electromagnetic Energy*, vol. 37, no. 4, pp. 237–247, 2002.
- [52] O. P. Gandhi and J.-Y. Chen, “Electromagnetic absorption in the human head from experimental 6-GHz handheld transceivers,” *IEEE Transactions on Electromagnetic Compatibility*, vol. 37, no. 4, pp. 547–558, 1995.
- [53] A. Hadjem, D. Lautru, C. Dale, M. F. Wong, V. F. Hanna, and J. Wiart, “Study of specific absorption rate (SAR) induced in two child head models and in adult heads using mobile phones,” *IEEE Transactions on Microwave Theory and Techniques*, vol. 53, no. 1, pp. 4–11, 2005.
- [54] S. C. Gnyawali, Y. Chen, F. Wu et al., “Temperature measurement on tissue surface during laser irradiation,” *Medical and Biological Engineering and Computing*, vol. 46, no. 2, pp. 159–168, 2008.

Research Article

Dual-Band On-Body Repeater Antenna for In-on-On WBAN Applications

Jinpil Tak, Kyeol Kwon, Sunwoo Kim, and Jaehoon Choi

Department of Electronics and Communications Engineering, Hanyang University, 17 Haengdang-dong, Seongdong-gu, Seoul 133-791, Republic of Korea

Correspondence should be addressed to Jaehoon Choi; choijh@hanyang.ac.kr

Received 24 June 2013; Revised 4 October 2013; Accepted 7 October 2013

Academic Editor: Panagiotis Kosmas

Copyright © 2013 Jinpil Tak et al. This is an open access article distributed under the Creative Commons Attribution License, which permits unrestricted use, distribution, and reproduction in any medium, provided the original work is properly cited.

A dual-band on-body repeater antenna for in-on-on wireless body area network applications is proposed. The proposed antenna has a maximum radiation normal to the human-body surface for communication with implanted devices in the 5.8 GHz industrial, scientific, and medical (ISM) band. In addition, to transmit the biological information received from the implanted devices to other on-body devices, the proposed antenna was designed to have a monopole-like radiation pattern along the surface of the human body for communication in the 2.45 GHz ISM band. The antenna was fabricated, and its performance was measured by attaching it to a human-equivalent semisolid phantom. In addition, the human-body effect was studied to ensure antenna performance under an actual situation.

1. Introduction

Owing to their variety of potential medical applications, wireless body area networks (WBAN) have received much attention. Medical implants for treatment, diagnosis, and monitoring have been studied in conjunction with the WBAN. For example, a biomedical self-monitoring system for implanted devices can be designed using the WBAN concept. For WBAN communication, the transmitter and receiver can be located in three regions: in-body, on-body, and off-body [1, 2]. However, the antennas of implanted devices usually have extremely low radiation efficiency because of the body effect. Therefore, establishing a direct communication link between the implanted antennas and antennas for on-body self-monitoring is difficult. To communicate effectively, the signals must be collected from the implanted devices and transmitted to the on-body self-monitoring devices using repeater systems, as shown in Figure 1. Therefore, the radiation characteristic of a WBAN antenna is an important factor that determines the overall performance of a system [3]. To achieve adequate performance, the field distribution of an antenna for a repeater system must be concentrated toward the human body to collect signals from the implanted devices at one frequency

and along the human-body surface to transmit these signals to the self-monitoring devices at another frequency. Thus, a directional radiation pattern toward the in-body direction is essential for on-body to in-body communication link. On the other hand, for proper communication link between two on-body transceivers, the antenna should generate omnidirectional field propagation along the body surface like a vertical monopole [4, 5]. However, a vertical monopole antenna is not suitable for on-body application because of the height. Therefore, the on-body to on-body communication requires a low-profile antenna with a monopole-like radiation pattern. To generate this monopole-like radiation pattern, various antenna types have been proposed [6–14]. A compact patch antenna with a vertical ground wall and a shorting wall was proposed in [6]. A planar inverted-F antenna using a shorting wall on a two-third muscle-equivalent arm phantom was published in [7]. Inspired by the design in [8], a higher mode (TM_{21}) microstrip patch antenna (HMMPA) was introduced in [9]. Further, other higher mode (TM_{01} and TM_{02}) circular patch antennas using shorting vias and coupled annular-ring patch were proposed in [10, 11]. To achieve broadband monopole-type radiation, a half-hemispherical dielectric resonator was suggested in [12]. Surface-wave antennas using via-less electromagnetic

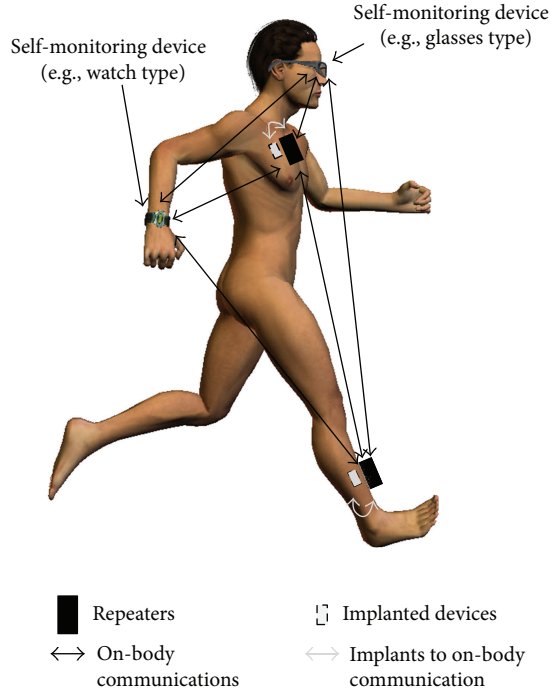


FIGURE 1: Configuration of the proposed antenna.

band-gap materials were introduced for low vertical size in [13, 14]. However, these antennas still have large horizontal size and are not suitable as repeater antennas because they do not provide the dual radiation performance required in the repeater system. Dual-band or dual-mode antennas for WBAN application were proposed in [15–17]. In [15], a dual-band antenna with a dual radiation pattern was proposed. A monoband antenna with a dual pattern was proposed in [16]. However, these antennas have dual- and triple-port systems. The dual-port system antenna for the dual mode or the triple-port system antenna for the triple mode has less novelty in terms of antenna design architecture. In addition, the multiport system is not suitable for miniaturization and integration with the devices. The proposed antenna in [17] has a broadside radiation characteristic, which is not suitable for on-body communication, including the on-body sensor network.

In this paper, a dual-band on-body repeater antenna for in-on-on WBAN applications is proposed. This proposed antenna operates in the 2.45 GHz industrial, scientific, and medical (ISM) band and the 5.8 GHz ISM band. For a one-port repeater system, the proposed antenna has a monopole-like radiation characteristic for on-on communication in the 2.45 GHz ISM band and a broadside radiation for in-on communication in the 5.8 GHz ISM band with a low profile. Although the use of the 5.8 GHz ISM band for in-on communication is unconventional by generally considering skin depth and attenuation, this frequency can be used to communicate with a low-depth implantable device such as a pacemaker implanted in the subcutaneous fat (in the near-field region). An implanted microstrip patch antenna is adopted for verification of the in-on communication in the

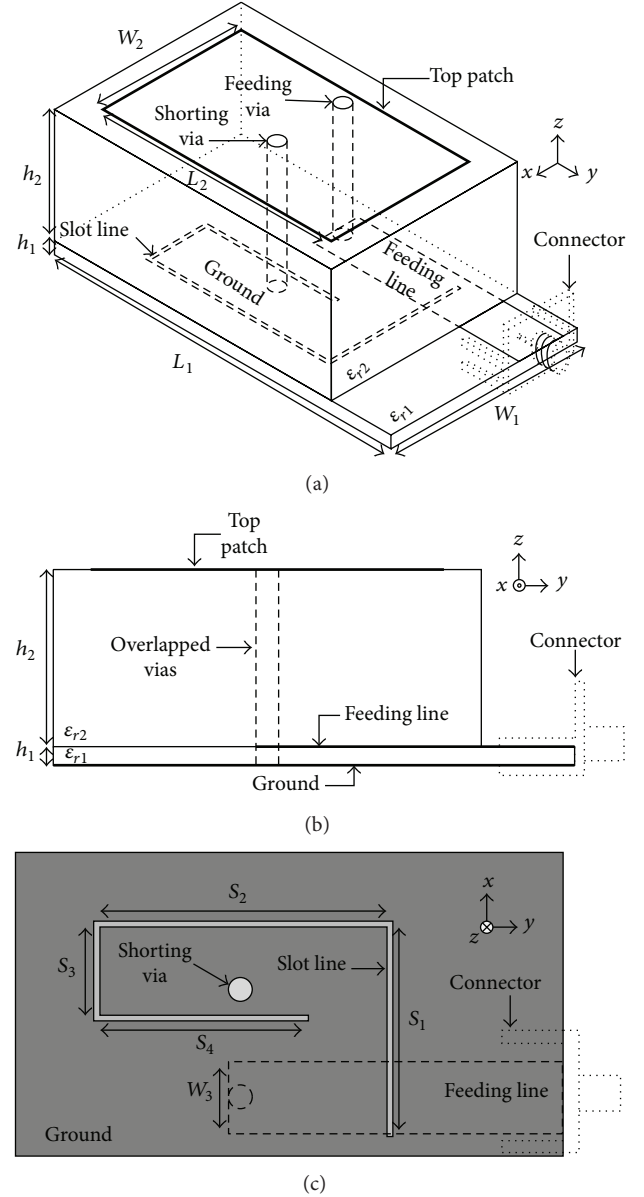


FIGURE 2: Geometry of the repeater antenna. (a) Isometric view. (b) Side view. (c) Bottom view. The parameters of the proposed antenna are $W_1 = 15.5$ mm, $W_2 = 11.5$ mm, $W_3 = 3.7$ mm, $L_1 = 28$ mm, $L_2 = 19$ mm, $h_1 = 1$ mm, $h_2 = 9.5$ mm, $\epsilon_{r1} = 2.33$, $\epsilon_{r2} = 2.33$, $S_1 = 11$ mm, $S_2 = 15.3$ mm, $S_3 = 5.1$ mm, and $S_4 = 11$ mm.

5.8 GHz ISM band. Moreover, a two-third muscle-equivalent human-body phantom is used to analyze the antenna performance.

2. Antenna Design and Simulation Result

The geometry of the repeater antenna for the in-on-on WBAN application is shown in Figures 2(a)–2(c). The proposed antenna has a dimension of $L_1 \times W_1 \times [h_1 + h_2]$ (10.5 mm) and consists of a top patch fed through a 9.5 mm

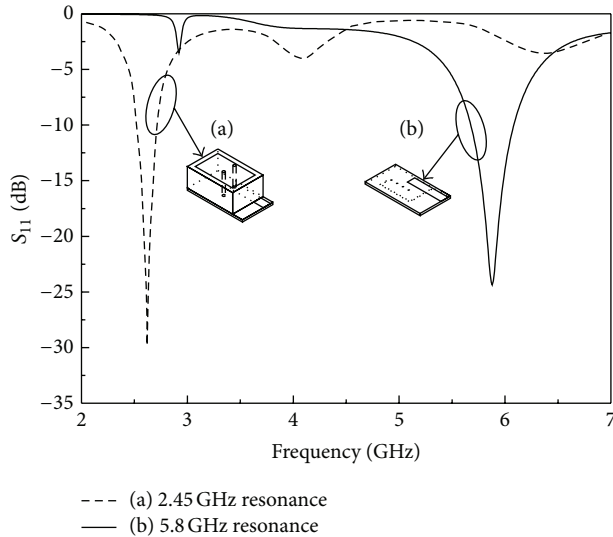


FIGURE 6: Radiating mechanism of the proposed antenna on the phantom. (a) 2.45 GHz ISM band. (b) 5.8 GHz ISM band.

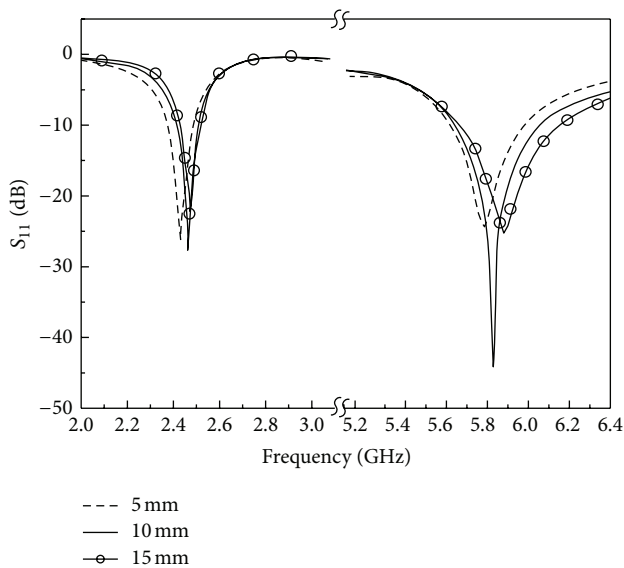


FIGURE 7: Comparison of the simulated S_{11} for various gap distances between the antenna and the phantom.

of the slot antenna, as shown in Figure 5. Therefore, achieving impedance matching is possible by controlling the overall slot length ($S_1 + S_2 + S_3 + S_4$) [20]. In our design, the slot line is optimized as a P-shape to miniaturize the antenna.

Figure 6 shows the radiation mechanism of the proposed antenna. The proposed antenna has only a single radiator. The radiating mechanism of this antenna is described as follows. (a) At 2.45 GHz, the top patch is excited by a via connected to the microstrip feeding line. This shorted top patch operates in the half- TM_{21} mode. (b) At 5.8 GHz, the slot line in the ground plane is excited by the microstrip

feeding line, and the radiating element is coupled to the slot line.

Figure 7 shows the simulated S_{11} characteristics of the proposed antenna for various gap distances (d) between the antenna and the phantom. The simulated 10 dB impedance bandwidths of the antenna at $d = 10$ mm were 4.5% (2.4–2.51 GHz) at the 2.45 GHz ISM band and 7.2% (5.62–6.04 GHz) at the 5.8 GHz ISM band.

In this research, we adopted the two-third muscle-equivalent phantom, which is simple, while having the same human-body effects as the three-layer phantom. Figure 8(a) shows that the permittivity and conductivity values of the six-sided two-third muscle-equivalent phantom are two-thirds those of the dispersive muscle; meanwhile, the three-layer phantom is composed of dispersive skin, fat, and muscle according to [18]. Figure 8(b) shows that the two results are almost the same.

Figures 9(a) and 9(b) show the simulated electric-field distributions in the yz -plane at $d = 10$ mm. The proposed antenna has a monopole-like electric-field distribution, which is desirable for on-body surface communication at the 2.45 GHz ISM band (Figure 9(a)), whereas the electric fields are strongly distributed toward the phantom surface at the 5.8 GHz ISM band (Figure 9(b)), which is a desirable property for implants for on-body communication.

Figure 10 shows the simulated current distribution on the top patch of the proposed antenna at 2.45 GHz. Assuming that no variation occurs along the z -axis, the current varies by one cycle along the x -direction and by one-half cycle along the y -direction, showing that the mode excitation on the patch is in a higher order mode (TM_{21}) at 2.45 GHz.

The simulated far-field radiation patterns of the proposed antenna for various gap distances (d) in the xz - and yz -planes are shown in Figure 11. As the gap increases (as d increases), the radiated field becomes slightly stronger because of the decreasing absorption into the phantom. In the yz -plane, the maximum simulated gain is 2 dBi. The radiation pattern of the proposed antenna is similar to that of a monopole in the 2.45 GHz ISM band.

Figures 12 and 13, respectively, show the isometric view of the simulation setup and the S-parameter characteristics of the in-on communication between the implanted microstrip patch antenna in the phantom and the proposed antenna on the phantom. The implanted microstrip patch antenna is designed with a patch size of 12 mm \times 12 mm on an FR-4 epoxy substrate with a dimension of 40 mm \times 40 mm \times 1 mm ($\epsilon_r = 4.4$ and $\tan\delta = 0.02$) and to operate in the 5.8 GHz ISM band. Considering practical implanted applications such as pacemakers, the implanted depth from the phantom surface (i) is 5 mm, and the gap between the proposed antenna and the phantom surface (d) is 10 mm. To prevent direct contact between the patch and the phantom, an air-gap insulation of 1 mm is adopted. Figure 13 shows that the proposed antenna is properly designed for in-on communications in the 5.8 GHz ISM band.

To evaluate the performance of the proposed antenna in a practical environment, a Duke anatomical human model is

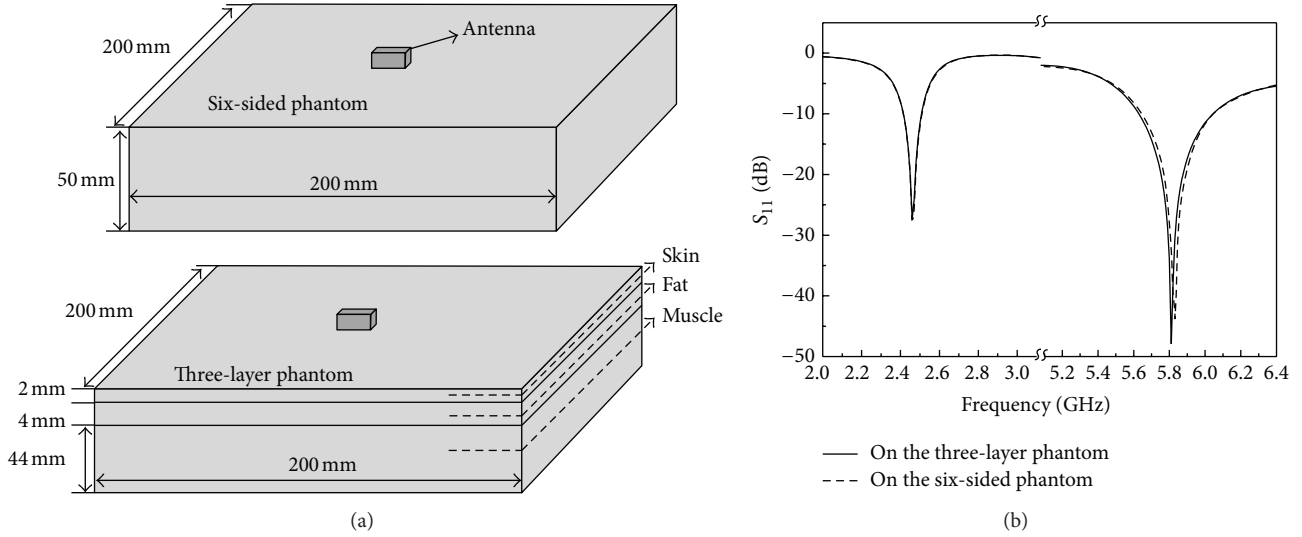


FIGURE 8: Comparison of the two phantom models. (a) Structure of the two phantom models. (b) Simulated S_{11} characteristics of the two phantom models.

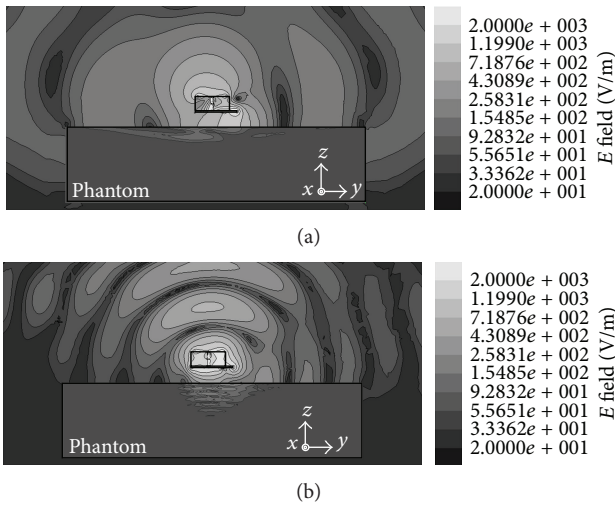


FIGURE 9: Simulated electric-field distribution of the proposed antenna. (a) 2.45 GHz ISM band. (b) 5.8 GHz ISM band.

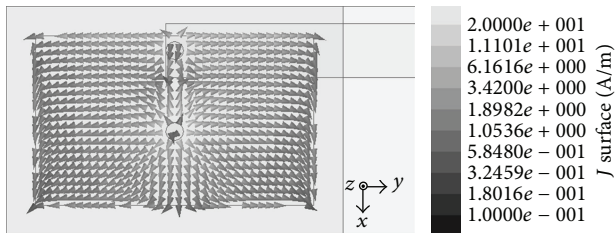


FIGURE 10: Simulated current distribution on the top patch of the antenna at 2.45 GHz.

adopted, as shown in Figure 14 [21]. The implanted microstrip antenna (port 1) is located just under the subcutaneous fat of

the left chest. The proposed antenna (port 2) is placed 10 mm above the left chest surface.

Figure 15 shows the comparison between the simulated S -parameter characteristics of the six-sided phantom shown in Figure 12 and those of the Duke model shown in Figure 14. Overall, the simulated results of the six-sided phantom are in good agreement with those of the Duke model.

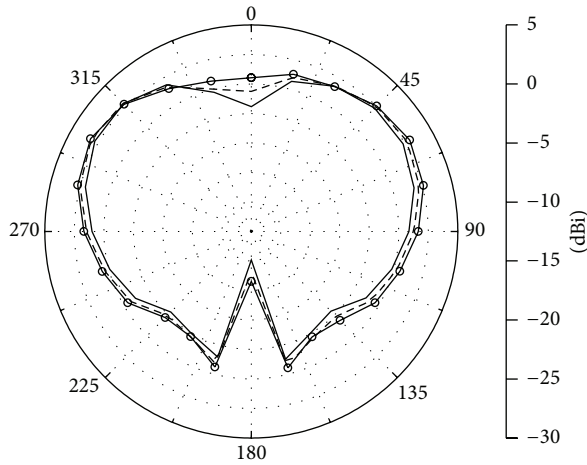
Figure 16 shows the simulated far-field radiation patterns of the proposed antenna with the Duke model at 2.45 GHz in the xz - and yz -planes. The maximum gain of the antenna is 1.5 dBi. The proposed antenna with the Duke model has a monopole-like radiation pattern in the 2.45 GHz ISM band.

Figure 17 shows the simulated average specific absorption rate (SAR) distribution normalized to the maximum SAR (input power: 1 W) of the proposed antenna with the Duke model. The American National Standards Institute requires that the SAR values should be below 1.6 W/kg over a volume of 1 g of tissue. The maximum SAR values are 17.92 W/kg at 2.45 GHz and 134 W/kg at 5.8 GHz (1 g tissue). To satisfy the SAR limitation (1.6 W/kg for partial-body exposure), the input power should be below 89.29 mW at 2.45 GHz and 11.94 mW at 5.8 GHz [22].

The simulation results of this study were obtained using HFSS based on the finite-element method and the SEMCAD X based on the finite-difference time-domain method [23, 24].

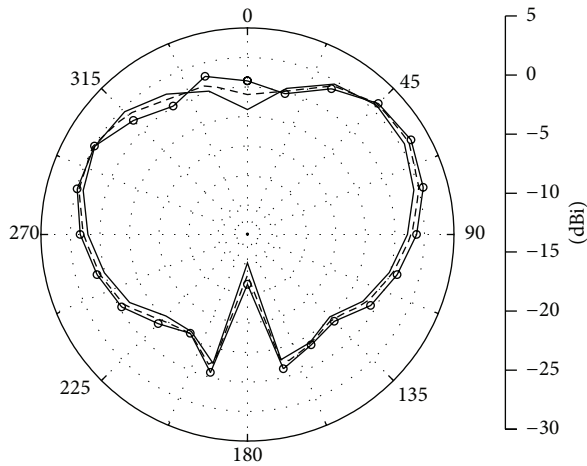
3. Experimental Results

The configurations of the proposed antenna and the fabricated two-third muscle-equivalent phantom (200 mm \times 200 mm \times 70 mm) for the measurement setup are shown in Figure 18. Because the manufactured phantom does not have dispersive permittivity and conductivity, it has only a single value in all frequencies. Therefore, we fabricated phantoms



- Gap = 5 mm
- - - Gap = 10 mm
- Gap = 15 mm

(a)



- Gap = 5 mm
- - - Gap = 10 mm
- Gap = 15 mm

(b)

FIGURE 11: Radiation patterns of the proposed antenna for various gap distances (d) at the 2.45 GHz ISM band. (a) xz -plane. (b) yz -plane.

for 2.45 and 5.8 GHz separately to validate the antenna performance in the two frequency bands. The electrical properties and ingredients of the two-third muscle-equivalent phantoms [7, 18, 25] at the 2.45 and 5.8 GHz ISM bands are summarized in Table 1.

Figure 19 shows the measured and simulated S_{11} characteristics of the proposed antenna on the phantom ($d = 10$ mm). For the measurement, the phantom for 2.45 GHz was used from 2 to 3 GHz and that for the 5.8 GHz was used from 5.2 to 6.4 GHz. The measured 10 dB impedance bandwidths of the antenna were 8.5% (2.37–2.58 GHz) in the 2.45 GHz ISM band and 7.1% (5.6–6.01 GHz) in the 5.8 GHz ISM band.

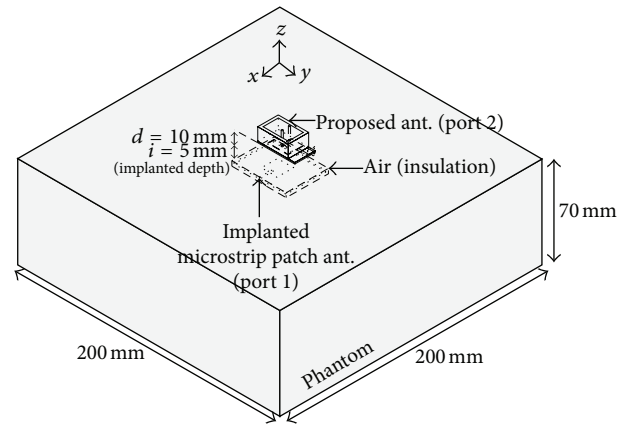


FIGURE 12: Isometric view of the simulation setup for the in-communication between the implanted microstrip patch antenna in the phantom and the proposed antenna on the phantom.

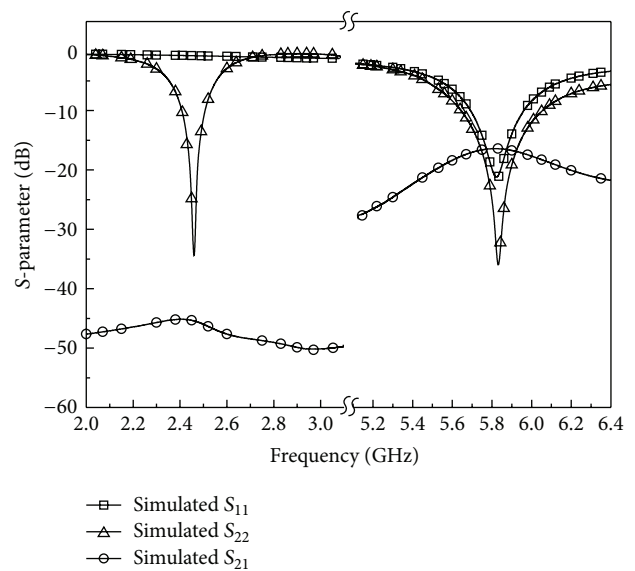


FIGURE 13: Simulated S-parameter characteristics of the in-communication between the implanted microstrip patch antenna in the phantom and the proposed antenna on the phantom (port 1: implanted microstrip antenna; port 2: proposed antenna).

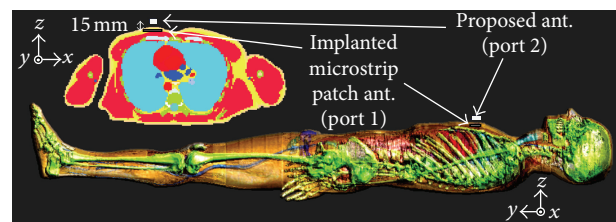


FIGURE 14: Simulation setup with the Duke model for verification of the proposed antenna in practical environment (port 1: implanted microstrip antenna; port 2: proposed antenna).

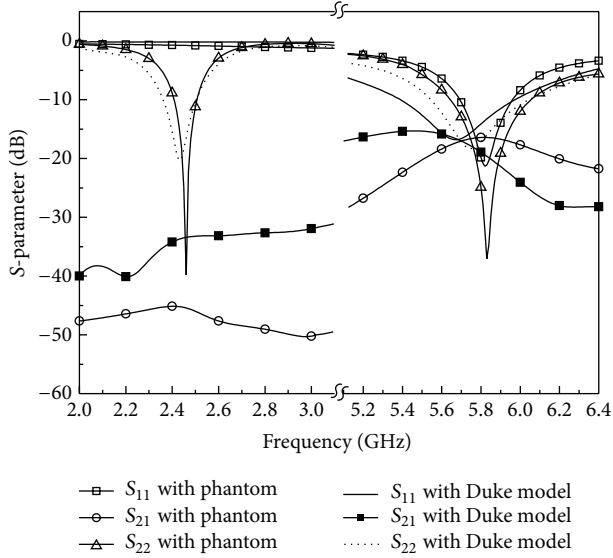


FIGURE 15: Comparison between the simulated S-parameter characteristics of the six-sided phantom and those of the Duke model (port 1: implanted microstrip antenna; port 2: proposed antenna).

TABLE 1: Electrical properties and ingredients of the two-third muscle-equivalent phantoms.

Ingredient	Composition ratio (%)	
	2.45 GHz ISM band ($\epsilon_r = 35.5, \sigma = 1.2 \text{ S/m}$)	2.45 GHz ISM band ($\epsilon_r = 35.5, \sigma = 1.2 \text{ S/m}$)
Deionized water	59.7	74.07
Polyethylene powder	14.92	22.22
Agar	2.98	3.7
Glycerin	20.89	—
TX-151	1.49	—

* Measurement temperature: 26°C.

Overall, the simulated result was in good agreement with the measurement result. The discrepancy between the simulated and measured results may have been due to manufacturing error of the three-layer fabricated antenna and inaccuracy of the phantom size.

Figure 20 shows the simulated and measured radiation patterns of the proposed antenna on the phantom when $d = 10 \text{ mm}$. The measured results agree reasonably well with the simulated results. The proposed antenna has a minimum radiation normal to the phantom surface and maximum radiation tangent to the phantom surface at 2.45 GHz. The measured peak gain of the proposed antenna on the phantom was 1.27 dBi. The measured radiation efficiency of the proposed antenna without the phantom was 61.92% at 2.45 GHz and 71.74% at 5.8 GHz and that of the proposed antenna with the phantom was 36.75% at 2.45 GHz and 75.76% at 5.8 GHz.

In this work, the proposed antenna is designed for the 5.8 GHz ISM band in-on communication with low-depth implantable device such as a pacemaker implanted

in the subcutaneous fat. Therefore, far-field analysis is not necessary to evaluate the in-on communication performance in this region. To verify the simulated result for the in-on communication, a microstrip patch antenna operating in the 5.8 GHz ISM band for implanted device was fabricated, as shown in Figure 21. The manufactured microstrip patch antenna has a unidirectional radiation pattern suitable for in-on communication.

Figure 22 shows the simulated and measured S-parameter characteristics of the in-on communication between the implanted microstrip patch antenna in the phantom and the proposed antenna on the phantom. In the measurement, a polystyrene foam was adopted as insulating air for the implanted antenna. Some discrepancies exist in the S_{21} . However, the overall trend of the measured S-parameters is in good agreement with that of the simulation. All results were obtained using the Agilent E8358A Network Analyzer.

4. Analysis of Body-Movement Effect

4.1. Received Signal Power at Various Antenna Locations. The received signal power on the on-body antennas depends on the antenna locations and body postures. To investigate the body effect on the received signal power, a channel measurement activity was conducted for various on-body antenna locations and human movements in the 2.45 GHz ISM band. The received signal power (S_{21}) at the on-body receiver was measured using a vector network analyzer, and a human body (height = 180 cm and weight = 90 kg) inside an anechoic chamber was used. A transmitter (Tx) antenna was placed on the left chest, and receive (Rx) antennas were placed on the head, chest, stomach, thigh, and arm. Three human movements, namely, standing, walking, and sitting up and down, were considered. For each movement and antenna location, the received power was measured for 10 s.

Table 2 shows the means and variances of the received signal power at various receiver positions and for different body postures. For human movements such as walking and sitting down and up, the signal power variance is larger than that for steady posture such as standing still. The received signal power values measured over 10 s at different Rx antenna positions are plotted in Figure 23. The received signal power is the strongest at the chest antenna, which is closest to the Tx antenna. In contrast, the thigh antenna shows the weakest received signal power because its distance from the Tx antenna is the longest. The proposed antenna shows the received signal power following our expectation under the WBAN settings.

4.2. Channel Capacity for Various Body Movements at Fixed Antenna Location. The channel capacity was also computed to evaluate the measured channels. The channel capacity is given by

$$C = \log_2(1 + \text{SNR}), \quad (1)$$

where SNR is the signal-to-noise ratio, which is determined by the received signal power/noise power. A noise power of -90 dBm was obtained from the measurement.

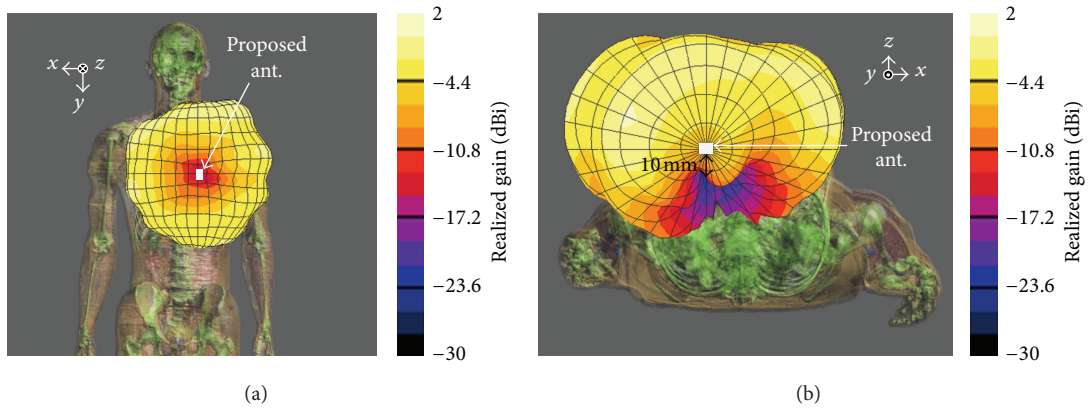


FIGURE 16: Radiation patterns of the proposed antenna with the Duke model at the 2.45 GHz ISM band. (a) xy -plane. (b) xz -plane.

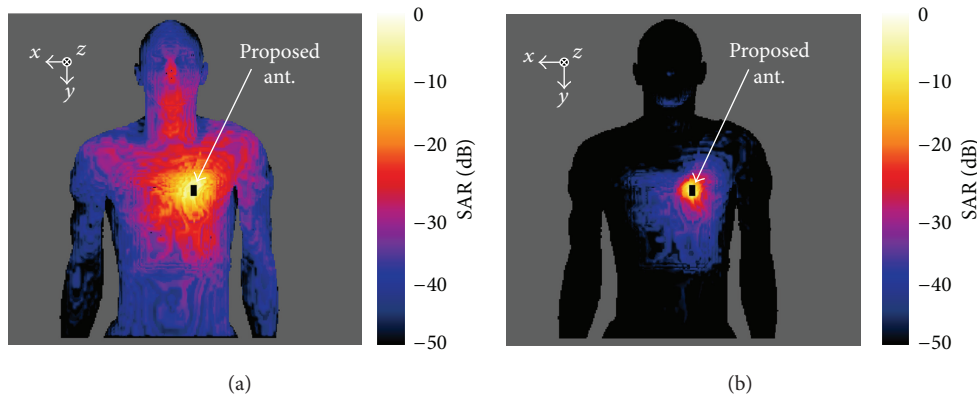


FIGURE 17: Simulated average SAR distribution of the proposed antenna with the Duke model (decibel normalized to the maximum SAR; input power: 1 W). (a) 2.45 GHz (maximum SAR: 17.92 W/kg). (b) 5.8 GHz (maximum SAR: 134 W/kg).

TABLE 2: Received power for various receiver positions and body postures.

	Standing	Walking	Sitting down and up
Arm			
Average	-57.4785	-58.2443	-54.7935
Dispersion	1.0192	6.5225	1.6766
Chest			
Average	-37.8377	-40.1259	-40.9304
Dispersion	0.1022	0.7348	1.0493
Head			
Average	-53.8209	-53.8702	-50.5486
Dispersion	0.7318	9.9121	1.8158
Stomach			
Average	-41.5824	-40.0269	-40.1617
Dispersion	0.0786	0.6043	2.0912
Thigh			
Average	-61.0783	-54.0026	-45.0382
Dispersion	2.8965	3.7319	8.9139

*Unit: dBm.

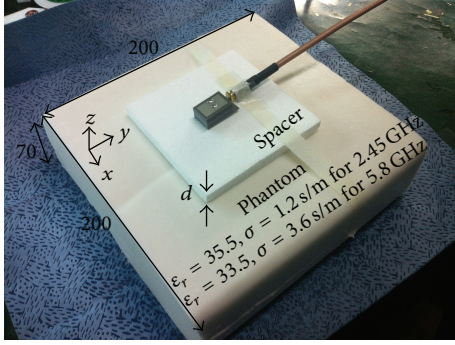


FIGURE 18: Fabricated antenna and two-third muscle-equivalent phantom for the measurement setup ($d = 10$ mm). The phantom for the 2.45 GHz ISM has $\epsilon_r = 35.5$, $\sigma = 1.2$ S/m and that for the 5.8 GHz ISM has $\epsilon_r = 33.2$ and $\sigma = 3.6$ S/m.

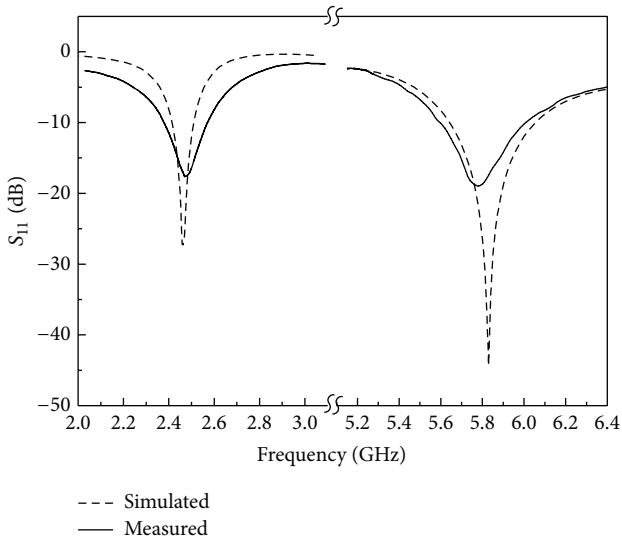


FIGURE 19: Measured and simulated S_{11} characteristics of the proposed antenna on the phantom ($d = 10$ mm).

Figures 24(a) and 24(b) show the cumulative density functions (CDFs) of the measured channel capacities for the three body movements at the chest and thigh. On average, the chest, which receives the strongest signal power, yields the largest channel capacity whereas the thigh, which has a weak received power, shows the smallest channel capacity. Figure 24 shows that, at a fixed antenna position, different human movements result in different channel capacities because the human movements cause variations in the Tx-Rx antenna separation and in the propagation conditions. Figure 24(b) shows that sitting up and down results in better channel capacity than standing still because the sitting movements shorten the Tx-Rx distance.

4.3. Probability Distribution Fitting. The empirical cumulative distribution function (CDF) for each antenna position and body posture was calculated from the normalized data. Several reference theoretical models (Nakagami- m , Rician, Gamma, and Weibull) were compared with the empirical

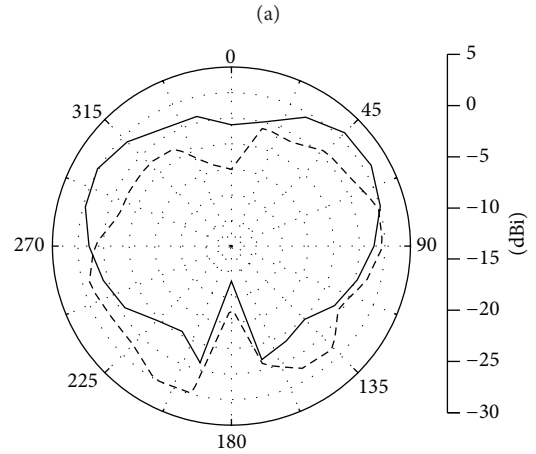
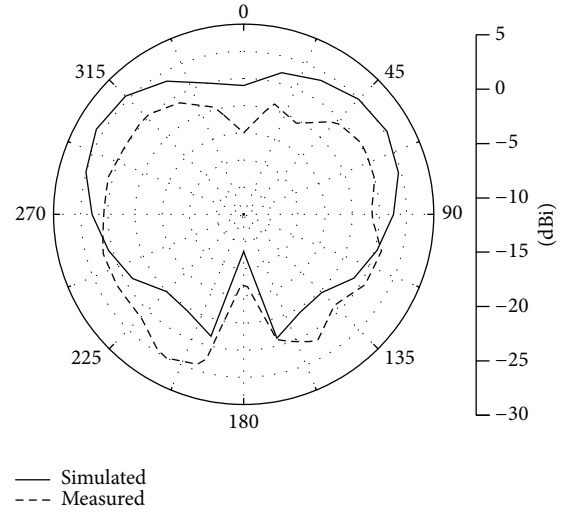


FIGURE 20: Simulated and measured radiation patterns of the proposed antenna on the phantom at 2.45 GHz ($d = 10$ mm). (a) xz -plane. (b) yz -plane.

CDFs using the Kolmogorov-Smirnov fit test (KS test) to determine the best fit distribution. This test calculates the maximal distance between the numerical data and the theoretical model data. The KS statistic is defined as [26]

$$D = \max_x |F_E(x) - F_X(x)|, \quad (2)$$

where F_E is the CDF of the measured data and F_X is the CDF of the theoretical distribution.

The distribution that provides the best fit in each case is the one with the lowest KS statistic. Table 3 shows the best fit model for each case, which fits the single branch envelope. In most cases, the fading models in each scenario follow the Weibull fading models. However, that of the antenna attached to the thigh follows the Nakagami and Gamma fading model. The Rician fading model shows the worst case in all measured data fitting.

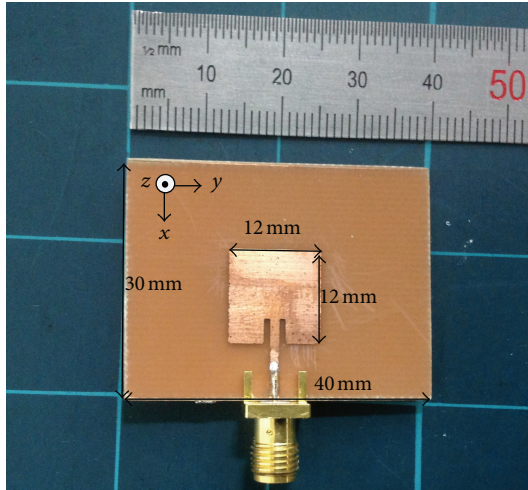


FIGURE 21: Geometry of the microstrip patch antenna for the implanted device operating in the 5.8 GHz ISM band for in-on communication measurement.

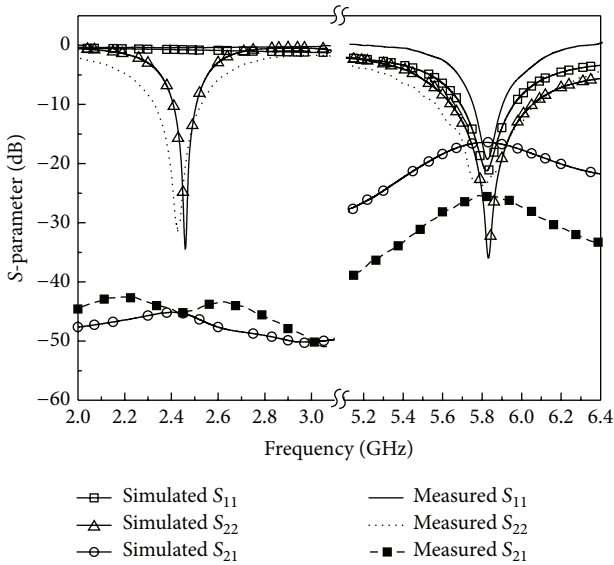


FIGURE 22: Simulated and measured S -parameter characteristics of the in-on communication between the implanted microstrip patch antenna in the phantom and the proposed antenna on the phantom as shown in Figure 10 (port 1: implanted microstrip antenna; port 2: proposed antenna).

5. Conclusion

A dual-band on-body repeater antenna for in-on-on WBAN applications has been proposed. The simulated and measured 10 dB impedance bandwidths were sufficient to cover the required frequency bands (2.45 GHz ISM band (2.4–2.485 GHz) and 5.8 GHz ISM band (5.725–5.825 GHz)). The proposed antenna provides a dipole-like radiation pattern for on-on body communication in the 2.45 GHz ISM band and a directional radiation pattern for the in-on body communication in the 5.8 GHz ISM band. To verify these properties, phantoms for 2.45 and 5.8 GHz were fabricated

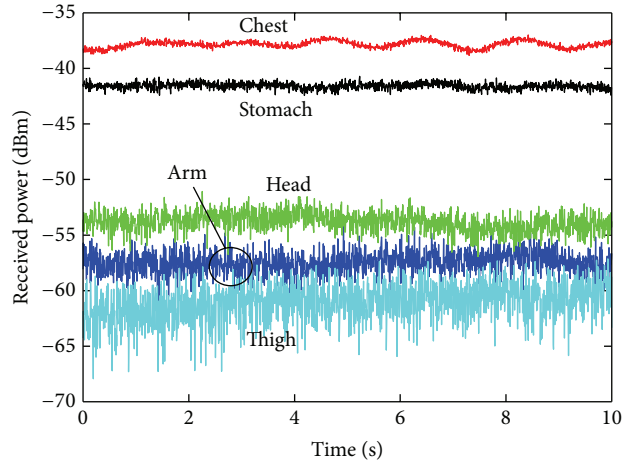
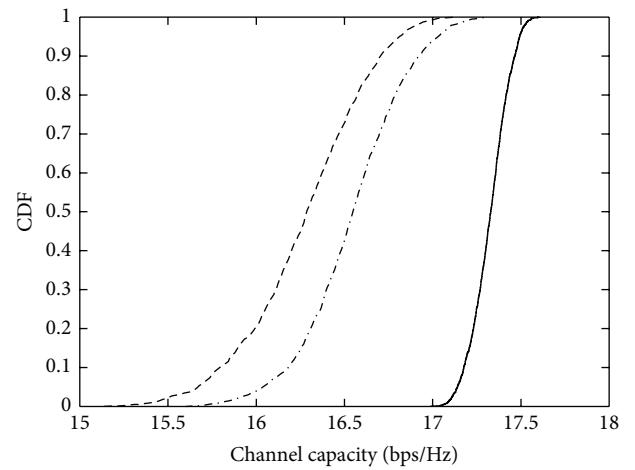
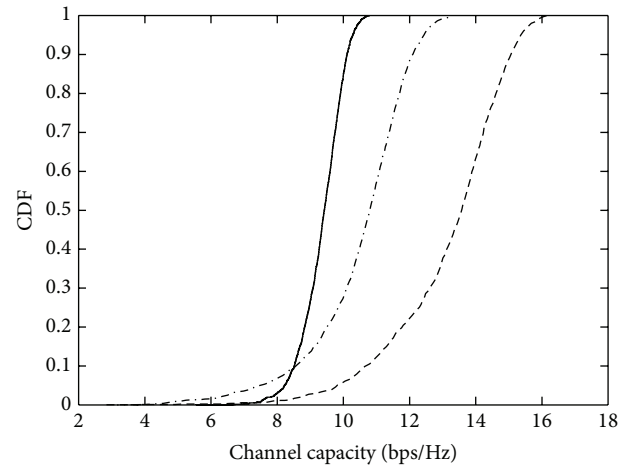


FIGURE 23: Measurement of received signal power comparison at the receiver position in standing posture.



— Standing
 - - - Walking
 - · - · - Sitting up and down

(a) Chest



— Standing
 - - - Walking
 - · - · - Sitting up and down

(b) Thigh

FIGURE 24: CDFs of the measured channel capacity comparison for various body postures for (a) chest and (b) thigh.

TABLE 3: Best fit distribution and estimated parameters for each measurement scenario.

Antenna position and body posture	Best fit	Envelope			
		Nakagami	Rician	Gamma	Weibull
Arm					
Standing	W	0.5926	0.6523	0.5059	0.0403
Walking	G	0.0127	0.0368	0.0039	0.9116
Sitting up and down	W	0.3249	0.3943	0.2461	0.0218
Chest					
Standing	W	0.621	0.621	0.5913	0.0789
Walking	W	0.9942	0.9968	0.9904	0.0039
Sitting up and down	W	0.5332	0.5915	0.4772	0.1124
Head					
Standing	W	0.9643	0.9912	0.9457	0.0246
Walking	W	0.6525	0.8733	0.4515	0.1233
Sitting up and down	W	0.3937	0.4713	0.3244	0.0114
Stomach					
Standing	W	0.9567	0.9428	0.9428	0.002
Walking	N	0.0001	0.0369	0.0245	0.1323
Sitting up and down	G	0.0018	0.002	0.0011	0.2187
Thigh					
Standing	G	0.073	0.1234	0.0413	0.8747
Walking	G	0.8025	0.7979	0.001	0.0024
Sitting up and down	N	0.001	0.009	0.004	0.1834

*W: Weibull; G: Gamma; N: Nakagami.

and used to measure the antenna performance. A channel measurement activity was conducted to investigate the effect of human-body movements and antenna locations. We have demonstrated that the proposed antenna can be effectively deployed on a human body to allow WBAN applications such as in a medical self-monitoring system owing to its dual-band characteristic and desirable field distributions.

Acknowledgments

This research was supported in part by the Korea Communications Commission (KCC), Republic of Korea, under the R&D program supervised by the Korea Communications Agency (KCA) KCA-2013-11911-01109, and in part by the National Research Foundation of Korea (NRF) Grant funded by the Korean government (MEST) (no. 2012-0005655).

References

- [1] P. S. Hall and Y. Hao, *Antennas and Propagation for Body-Centric Wireless Communications*, chapter 1, Artech House, Norwood, Mass, USA, 2006.
- [2] Y. Rahmat-Samii and J. Kim, *Implanted Antennas in Medical Wireless Communications*, chapter 1, Morgan & Claypool Publishers, San Rafael, Calif, USA, 2006.
- [3] M. R. Kamarudin, Y. I. Nechayev, and P. S. Hall, "Performance of antennas in the on-body environment," in *Proceedings of the IEEE Antennas and Propagation Society International Symposium and USNC/URSI Meeting*, vol. 3A, pp. 475–478, Washington, DC, USA, July 2005.
- [4] C. A. Balanis, *Antenna Theory: Analysis and Design*, pp. 27–32, chapter 1, Wiley-Interscience, New York, NY, USA, 3rd edition, 2005.
- [5] P. S. Hall, Y. Hao, Y. I. Nechayev et al., "Antennas and propagation for on-body communication systems," *IEEE Antennas and Propagation Magazine*, vol. 49, no. 3, pp. 41–58, 2007.
- [6] K.-L. Wong and C.-I. Lin, "Characteristics of a 2.4 GHz compact shorted patch antenna in close proximity to a lossy medium," *Microwave and Optical Technology Letters*, vol. 45, no. 6, pp. 480–483, 2005.
- [7] C. H. Lin, K. Saito, M. Takahashi, and K. Ito, "A compact planar inverted-F antenna for 2.45 GHz on-body communications," *IEEE Antennas and Propagation Society*, vol. 60, no. 9, pp. 4422–4426, 2012.
- [8] C. Delaveaud, P. Leveque, and B. Jecko, "New kind of microstrip antenna: the monopolar wire-patch antenna," *IEEE Electronics Letters*, vol. 30, no. 1, pp. 1–2, 1994.
- [9] G. A. Conway and W. G. Scanlon, "Antennas for over-body-surface communication at 2.45 GHz," *IEEE Transactions on Antennas and Propagation*, vol. 57, no. 4, pp. 844–855, 2009.
- [10] J. Liu, Q. Xue, H. Wong, H. W. Lai, and Y. Long, "Design and analysis of a low-profile and broadband microstrip monopolar patch antenna," *IEEE Transactions on Antennas and Propagation*, vol. 61, no. 1, pp. 11–18, 2013.
- [11] A. Al-Zoubi, F. Yang, and A. Kishk, "A broadband center-fed circular patch-ring antenna with a monopole like radiation pattern," *IEEE Transactions on Antennas and Propagation*, vol. 57, no. 3, pp. 789–792, 2009.
- [12] D. Guha and Y. M. M. Antar, "New half-hemispherical dielectric resonator antenna for broadband monopole-type radiation," *IEEE Transactions on Antennas and Propagation*, vol. 54, no. 12, pp. 3621–3628, 2006.

- [13] R. Khouri, P. Ratajczak, P. Brachat, and R. Staraj, "A thin surface-wave antenna using a via-less EBG structure for 2.45 GHz on-body communication systems," in *Proceedings of the 4th European Conference on Antennas and Propagation (EuCAP '10)*, Barcelona, Spain, April 2010.
- [14] F. Yang, Y. Rahmat-Samii, and A. Kishk, "Low-profile patch-fed surface wave antenna with a monopole-like radiation pattern," *IET Microwaves, Antennas and Propagation*, vol. 1, no. 1, pp. 261–266, 2007.
- [15] Z. G. Liu and Y. X. Guo, "Dual band low profile antenna for body centric communications," *IEEE Transactions on Antennas and Propagation*, vol. 61, no. 4, pp. 2282–2285, 2013.
- [16] A. A. Serra, A. R. Guraliuc, P. Nepa, G. Manara, I. Khan, and P. S. Hall, "Dual-polarisation and dual-pattern planar antenna for diversity in body-centric communications," *IET Microwaves, Antennas and Propagation*, vol. 4, no. 1, pp. 106–112, 2010.
- [17] K. Kwon, J. Ha, S. Lee, and J. Choi, "Design of a dual-band on-body antenna for a wireless body area network repeater system," *International Journal of Antennas and Propagation*, vol. 2012, Article ID 350797, 5 pages, 2012.
- [18] C. Gabriel, "4-Cole-Cole analysis on compilation of the dielectric properties of body tissues at RF and microwave frequencies," Brooks Air Force Tech. Rep. AL/OE-TR-1996-0037, 1996, <http://www.fcc.gov/fcc-bin/dielec.sh>.
- [19] W. Hong, B. Liu, Y. Q. Wang et al., "Half mode substrate integrated waveguide: a new guided wave structure for microwave and millimeter wave application," in *Proceedings of the 31st International Conference on Infrared and Millimeter Waves and 14th International Conference on Terahertz Electronics (IRMMW-THz '06)*, p. 219, Shanghai, China, September 2006.
- [20] R. Garg, P. Bhartia, I. Bahl, and A. Ittipiboon, *Microstrip Antenna Design Handbook*, pp. 441–463, chapter 7, Artech House, Norwood, Mass, USA, 2001.
- [21] A. Christ, W. Kainz, E. G. Hahn et al., "The virtual family—development of surface-based anatomical models of two adults and two children for dosimetric simulations," *Physics in Medicine and Biology*, vol. 55, no. 2, pp. N23–N38, 2010.
- [22] "IEEE standard for safety levels with respect to human exposure to radio frequency electromagnetic fields, 3 kHz to 300 GHz," *IEEE Standard C95*, pp. 1–1999, 1999.
- [23] HFSS, "High Frequency Structure Simulator Based on Finite Element Method," v. 15.0, ANSYS Corp., 2013.
- [24] X. Semcad, *A FDTD-Based Electromagnetic Simulator*, version 14.6.9 Bernina, Schmid & Partner Engineering AG, Zurich, Switzerland, 2013.
- [25] S. Lee, W. Seo, K. Kwon, and J. Choi, "The study on implementation of a semi-solid flat phantom with equivalent electrical properties to whole human body at MICS and ISM band," *The Korean Institute of Electromagnetic Engineering & Science*, vol. 23, no. 1, pp. 101–107, 2012.
- [26] A. Michalopoulou, A. A. Alexandridis, K. Peppas et al., "On-body channel statistical analysis based on measurements in an indoor environment at 2.45 GHz," *IET Microwaves Antennas and Propagation*, vol. 6, pp. 636–645, 2012.

Research Article

Electric Field Measurement of the Living Human Body for Biomedical Applications: Phase Measurement of the Electric Field Intensity

Ichiro Hieda¹ and Ki Chang Nam²

¹ National Institute of Advanced Industrial Science and Technology (AIST), Tsukuba 305-8566, Japan

² Yonsei University College of Medicine, Seoul 120-752, Republic of Korea

Correspondence should be addressed to Ichiro Hieda; i-hieda@aist.go.jp

Received 20 June 2013; Revised 30 August 2013; Accepted 8 October 2013

Academic Editor: Yifan Chen

Copyright © 2013 I. Hieda and K. C. Nam. This is an open access article distributed under the Creative Commons Attribution License, which permits unrestricted use, distribution, and reproduction in any medium, provided the original work is properly cited.

The authors are developing a technique for conducting measurements inside the human body by applying a weak electric field at a radio frequency (RF). Low RF power is fed to a small antenna, and a similar antenna located 15–50 cm away measures the electric field intensity. Although the resolution of the method is low, it is simple, safe, cost-effective, and able to be used for biomedical applications. One of the technical issues suggested by the authors' previous studies was that the signal pattern acquired from measurement of a human body was essentially different from that acquired from a phantom. To trace the causes of this difference, the accuracy of the phase measurements was improved. This paper describes the new experimental system that can measure the signal phase and amplitude and reports the results of experiments measuring a human body and a phantom. The results were analyzed and then discussed in terms of their contribution to the phase measurement.

1. Introduction

The authors are developing a technique for conducting measurements inside the human body by applying a weak electric field at radio frequency (RF), typically 1–60 MHz [1, 2].

Technological advancements have led to the development of high-level diagnostic techniques, including X-ray computed tomography (X-ray CT), magnetic resonance imaging (MRI), and positron emission tomography (PET), which have contributed greatly to medical care and welfare. However, such high-level care and large-scale medical equipment represent financial burdens to taxpayers in most developed countries. Moreover, due to these costs, people in developing countries rarely benefit from these high-level diagnostic techniques. From this perspective, simple and easy-to-use equipment utilizing electric impedance and magnetic induction is expected [3–6]. The authors started to apply the radio imaging method, which was originally used for geological survey (RIM), to the measurement of the human body [2, 7,

8]. Later, the evolved technique was classified as an electric field method [9, 10].

There are several studies of biomedical measurements that use an electromagnetic wave. One example is microwave tomography. The basic principle of their projects is similar to our proposal. To obtain finer resolution less than 1 cm, pulse signals and multiple antennas for transmitting and receiving were implemented [11–14]. Because attenuation in the human body at the microwave frequency range is remarkable, an electromagnetic darkroom is necessary to prevent interference of an electromagnetic wave along indirect paths as well as to suppress emission of the microwave to the outside environment.

The authors' method is simple, safe, and cost-effective and leads to the expectation of two goals. One is the extension of the current experimental system, which can be applied to medical screenings such as abdominal fat CT.

Another goal is smaller systems able to be used as wearable sensors or installed at home, such as urine volume sensors and dehydration alarms, for welfare and health care.

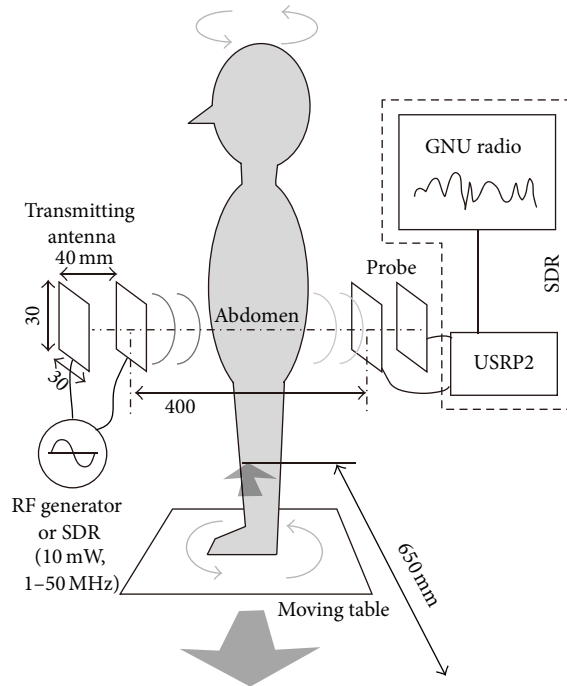


FIGURE 1: Overview of the experiment. A subject stood still on the moving table. The transmitting antenna and the probe were set at the height of the abdomen of the subject. USRP comprised an RF front end and A/D converter that worked as a software-defined radio (SDR) in conjunction with GNU Radio software installed on a PC.

Figure 1 shows an overview of the developed system. A portion of the human body was scanned by a weak electric field at radio frequency (RF), and the measured signals were analyzed to obtain the permittivity that corresponded to the moisture distribution inside the body.

Experiments were performed in previous studies to determine basic characteristics of the method. To support the experimental results, the measurement system was numerically simulated using the finite-difference time-domain (FDTD) method [15–19]. One of the technical issues suggested by these previous studies was that when the human body was measured, the pattern of the electric field intensity differed from that of a phantom [1, 17].

When the system scanned the phantom, an acrylic water tank filled with water, the electric field intensity at the receiving antenna increased due to the high relative permittivity of the water, which was approximately 70. In contrast, human body tissues have a variety of permittivities. The permittivities of tissues containing much moisture, for example, muscles and internal organs, are as high as those of water at room temperature and pressure [20]. Therefore, water was used for the medium of the phantom to simulate a portion of the human body that contains much moisture.

When the system scanned the living human body, however, the electric field intensity decreased. This was caused by RF current leakage through the human body, which had much larger dimensions and a much tighter electrostatic connection to the electric ground than the phantom. It was experimentally confirmed that measurement of signal

strength was simple subtraction of the loss from the increment caused by current leakage and permittivity, respectively [17]. Because the signal attenuation from the current leakage was dominant, the effect of the human body permittivity was buried in the measurement data. Improving the phase measurement capability of the electric field intensity would help to discriminate the effect of permittivity from signal attenuation caused by the current leakage.

In this paper, a new experimental system that can measure the signal phase and amplitude is described. Experiments are also reported where the human body and a phantom were measured by the system. The results were analyzed and discussed in terms of their contribution to the phase measurement.

2. Method

2.1. Experimental System. Figure 2 shows a schematic block diagram of the experimental system. The system comprised transmitting (TX) and receiving (RX) subsystems. Both of the subsystems had a software-defined radio (SDR), an amplifier, an RF transformer, and an antenna.

An SDR is a radio communication system with minimal hardware, and most of the functions are implemented by means of computer software [21, 22]. The experimental system had two hardware peripherals, Ettus Research USRP N200 and USRP2, for transmitting and receiving, respectively [23]. Each peripheral had a high-speed analog-to-digital converter (ADC) and a digital-to-analog converter (DAC). They sent and received digital streaming data to and from personal computers (PCs) via gigabit Ethernet interfaces. GNU Radio, an open source SDR software, was installed on the PCs and was optimized for the USRP series of SDR peripherals [24].

The RX subsystem was the same as that of the previous experimental system [22], except that the reference clock was fed by the external base frequency oscillator instead of the internal clock. The receiving antenna generated a signal in accordance with the electric field intensity, and this signal was fed to USRP2 via both an RF transformer and an amplifier. The received signal was filtered and stored on the computer (PC1) by the SDR software. The USRP N200 series was the successor of the USRP2 series, and both series have the same basic performance and functions. PC1 and PC2 were desktop computers with Intel Core i7 processors.

The previous TX subsystem comprised a battery-powered oscillator and an antenna to simplify the system [25]. The new system added another SDR (SDR2) to the TX subsystem, as shown in Figure 2. A continuous wave (CW) at a certain frequency can be generated by SDR2. In the experiment described in this paper, only a 48 MHz CW was used. The output of the SDR was amplified by the external amplifier and approximately 10 mW of the RF power was fed to the TX antenna. The reference clock of the USRP2 was provided by the same base frequency oscillator as the RX subsystem.

Because the two SDR peripherals (USRP2 and USRP N200) had the same reference clock, their internal oscillators were locked in phase. If the transmitting and receiving

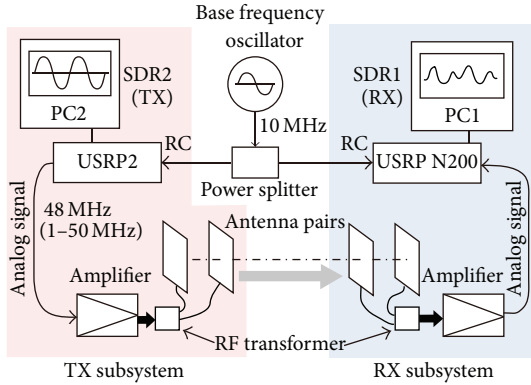


FIGURE 2: Schematic block diagram of the experimental system. The system consisted of TX and RX subsystems and a base frequency oscillator. Both of the subsystems had a PC, a USRP (SDR peripheral), an external amplifier, an RF transformer, and an antenna. Because the two USRPs had the same reference clock, the internal oscillators were locked in phase.

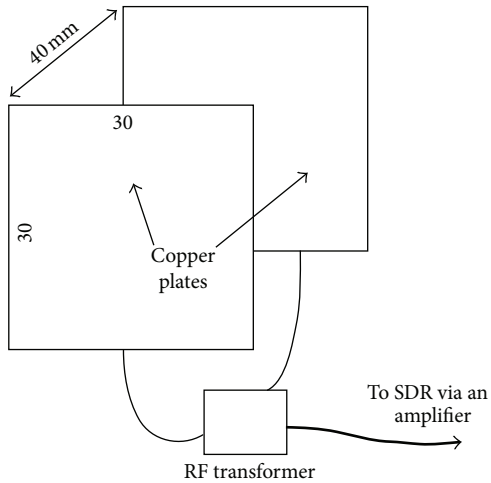


FIGURE 3: Illustration of an antenna. Two square copper plates were set 40 mm apart. The same types of antennas were used for transmitting and receiving.

frequencies were set to the same frequency, the RX SDR could measure not only the amplitude of the signal transmitted by the TX SDR but also the phase of the signal. This was a great advantage of the new system compared to the previous system.

Figure 3 shows the antennas used in the experiment. They were made of thin copper plates measuring 30 mm^2 . The two plates were set parallel 40 mm apart. Antennas of the same type were set 400 mm apart and used for both transmitting and receiving. Because the antennas and RF transformers were optimized to generate and detect electric fields, the emission of electromagnetic waves from the TX antenna was very weak. The reinforced concrete walls and ceilings of the building were able to prevent emission to the outside.

2.1.1. Experiment 1. Figure 4 shows the configuration of the water tank measurement. An acrylic water tank filled with

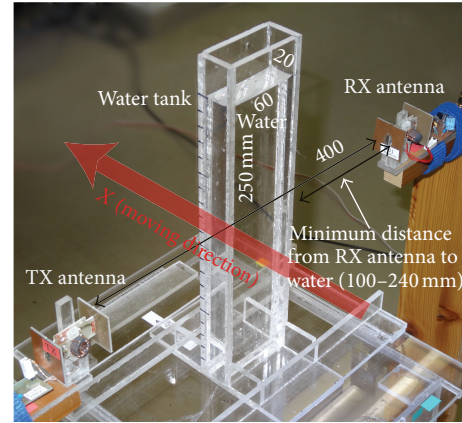


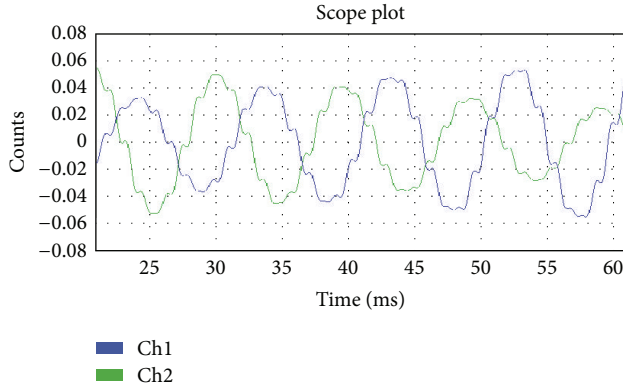
FIGURE 4: Overview of the water measurement. The water tank moved in between the TX and RX antennas so that the water was scanned by the antenna system one dimensionally. The minimum distance from the RX antenna to the inside of the water tank could be configured from 100 to 240 mm.

water was used as the phantom to simulate a portion of the human body. The inside dimensions of the water tank were $20(\text{W}) \times 60(\text{D}) \times 250(\text{H})\text{ mm}$, and the tank was filled with water at room temperature. The relative permittivity of water at room temperature and pressure is approximately 70, which is as high as some human organs, such as muscles and internal organs [20]. The relative permittivity of the acrylic was approximately 4, and the walls of the tank were 5 mm thick. The effect of the walls on the electric field was negligible.

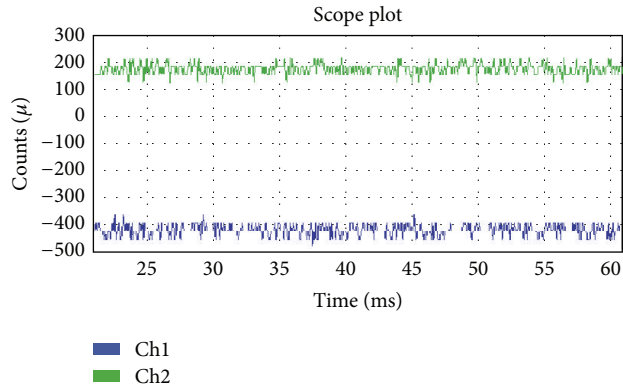
The dimensions of the water tank were much smaller than the actual human body. It was confirmed by experiments and simulation in our previous studies that addition and subtraction of dielectric material in the measured space worked [2, 26]. By changing the position of the water tank, the changes of the electric field intensity were measured. The summation of certain regions of the measurement was equivalent to the result of a large phantom that was as large as the measured region of the small phantom. Moreover, the small tank was convenient to evaluate the effect of a certain region on the measurement result or sensitivity.

The water tank was put on a motor-driven acrylic table. The water tank moved 650 mm in a straight line perpendicular to the centerline of the transmitting and receiving antennas. Signal strength was measured continuously while the water tank moved. The measurement was repeated 10 times for each line.

2.1.2. Experiment 2. Figure 1 shows an overview of Experiment 2. The abdomen of a healthy male subject, 54 years old, 168 cm tall, and weighing 61.5 kg, was measured. The moving table moved straight 650 mm to scan the abdomen of the subject with the antenna pair one dimensionally. The subject stood still on the table facing perpendicular to the moving direction so that the one-dimensional back projection of the abdomen was measured. Both forward and backward measurements were performed. The measurement took approximately two minutes. The authors are planning



(a) TX and RX are not synchronized



(b) TX and RX are synchronized

FIGURE 5: I/Q outputs from the SDR peripheral. The blue and green lines show the I and Q signals, respectively.

to measure a subject from 16 directions to build a two-dimensional image. The measurement takes approximately 30 minutes. It was confirmed by preliminary experiment that 30 minutes was the limit for a normal adult to stand on the moving table calmly. This is the reason that the subject was only measured twice in two minutes.

3. Results and Discussion

Figure 5 shows SDR outputs for a period of 40 ms where (a) TX and RX SDRs used independent internal reference clocks and (b) TX and RX SDR used the same reference clock, respectively. The RX SDR provides I/Q data that had phase information of the time domain signal as well as magnitude [21]. The I/Q data were stored and processed by the computers in the form of a complex number.

Figure 5(a) shows the received signals where the TX and RX SDRs were connected to each other by a coaxial cable. Both of the I/Q signals were sinusoidal waves with a small level of harmonics. From the figure, the base frequency of the waves was calculated as 103 Hz or 2.14 ppm of the fundamental frequency, 48 MHz.

In Figure 5(b), a portion of the received signal in Experiment 1 is shown. The I/Q signals were DC with a small level of random noise. Because the fundamental frequency of the signals was 0 Hz, the TX and RX SDRs were confirmed to be

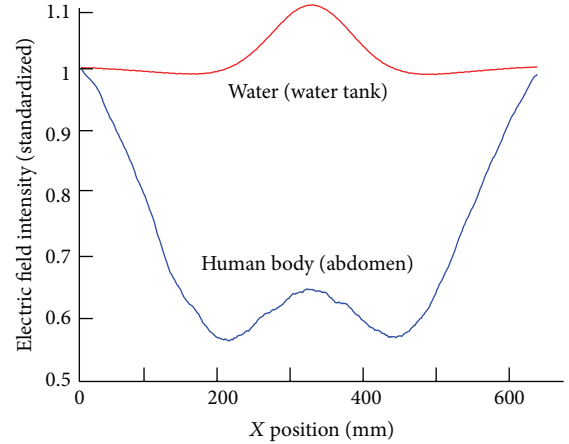


FIGURE 6: Relation between (Y) electric field intensity and (X) distance of the water tank and the living human body from the home position where the data were averaged for the 10 and 2 measurements, respectively. Both of the electric field intensities were standardized by the respective values as the starting point or $X = 0$.

synchronized. When the SDRs were synchronized, the phase difference between TX and RX, θ , was calculated by

$$\theta = \tan^{-1} \frac{Q}{I}, \quad (1)$$

where I and Q were signed amplitudes of the I and Q signals, respectively.

Figure 6 shows the relationships between electric field intensities and phases versus the position of the water tank and the living human body. Each electric field intensity was standardized by the respective value of the starting point, or $X = 0$. The electric field intensities of the water tank and abdomen were averages of 10 and 2 measurements, respectively. The patterns of the signal changes matched the results of previous experiments [1, 22].

As shown in Figure 6, when the water was measured, the electric field intensity increased gradually and made a broad peak. After the peak, the electric field intensity decreased symmetrically. The width of the water in the tank was only 20 mm; however, the skirt of the measured data was as wide as 200 mm. Because the signal changes caused by permittivity of water were steady and reproducible, the data could be used to build reverse filters for the measured data [27–30].

As shown in the same figure, the pattern of the electric field intensity for the living human body was more complex than that of the phantom. The electric field intensity drastically decreased to 55% of the strength at the starting point and then increased to a small peak, as high as 65%. After the electric field intensity decreased to a second trough, it increased up to the starting level. The signal changes were nearly symmetrical. The abdomen of the subject was as wide as 330 mm; however, the electric field intensity was affected by the living body for 650 mm, the total length of the table movement. In the case of the living body measurement, the attenuation of the electric field intensity, which was caused by current flowing to the virtual ground through the human

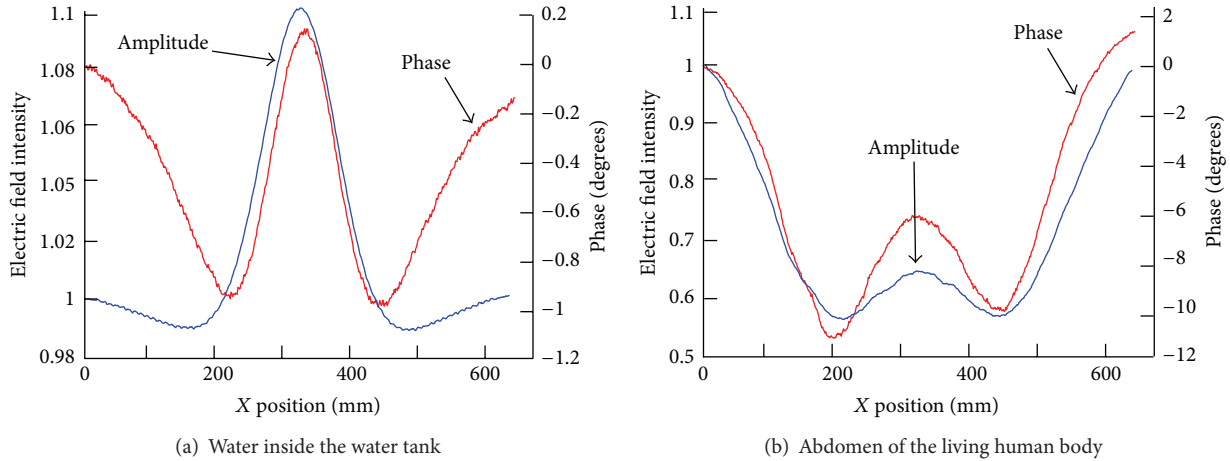


FIGURE 7: Amplitude and phase of the electric field intensity against X position.

body and had larger dimensions and static induction to the ground than the water tank, was dominant [17].

The purpose of the study was to obtain a clue to extract the permittivity-induced signal increase from the attenuation caused by the body current. Consequently, the experimental system was upgraded.

Figures 7(a) and 7(b) show the phase changes of the measured signals that were calculated from the I/Q data of the water tank and the human abdomen measurements, respectively, along with the electric field intensities redrawn from the data in Figure 6. Although the phases were provided, the absolute phase reference of the signals was unable to be obtained by the current system. Therefore, the signal received when the moving table was at the starting point, $X = 0$, was defined as the reference for the measurement. Phases in the figures represent differences between the respective reference phases.

In Figure 7(a), the phase decreased from the starting point and reached -1 degree, where $X = 220$ mm. At that point, the phase increased sharply along with the electric field intensity and recovered to the original value at the center of the moving table path. However, the peak positions of the electric field intensity and the phase were 6 mm apart. After the peaks, both of the values decreased to their previous minimum values. The phase recovered again and returned approximately to the original value.

The phase axis in the figure was magnified to understand the characteristics easily; however, the range of the phase was from zero to -1 degree at most. The electric field intensity increased 10% at the peak.

The measurement was done in the near field of the transmission and receiving antennas. The dielectric material, such as water or the human body, caused irregularity of the electric field. As a result, the electric field intensity at the receiving antenna increased or decreased. The authors also confirmed this effect by FDTD simulation [15].

When the human body was measured by the method, the electric field intensity at the receiving antenna was weakened by the effect of leakage current that flowed to the ground of the environment. This effect was observed in a simplified

experiment [17]. The connection between the human body and the ground of the environment has not been modeled, so the behavior of the current has not been simulated.

The phase changes of the electric field in Figures 7(a) and 7(b) were not significant compared with the changes of the electric field intensity. Moreover, the phase and the respective intensity were interdependent. The phase itself did not work to abstract the effects of the permittivity from the loss caused by the body current.

The experimental system was upgraded and the phase measurement function was verified by the experiment. Notably, the phase patterns of the electric field intensity and the phase of the living body were different from those of the phantom as well as the amplitude of the electric field intensity.

However, it was difficult to discriminate losses caused by the body current from the increase in the electric field intensity by the permittivity of the moisture using the provided data themselves. The phase was important but not sufficient to discriminate them.

Using multiple frequencies may help to discriminate the permittivity's effects from the current losses. The upgraded system can measure amplitude and phase from 1 to 60 MHz, but optimum antenna systems for the measurement frequencies should be built and tuned for each measurement frequency [17].

The phase started changing at the first measurement point. Therefore, it may also be necessary to extend the travel path of the moving table by upgrading the measurement system. Simulation of a total experimental room including the subject body by a large-scale commercial FDTD simulator package should be effective for the investigation of the body current as well.

4. Conclusion

A new experimental system was introduced that could measure the phase and amplitude of the electric field intensity. Using the system, basic measurements were performed using a water tank and a living human body. The phases at a radio frequency, 48 MHz, were confirmed by measurement results

to be properly measured. Because an SDR with software developed by an open source project was used, the system is simple and cost-effective.

The phase of the measured signal was important information to discriminate the signal increase by the permittivity of moisture from the signal decrease by the current losses. However, the phases and the amplitudes were interdependent. Therefore, the development of an additional method, for example, the use of multiple antennas and a wide range of frequencies, is necessary.

References

- [1] I. Hieda and K. C. Nam, "Electric field measurement for biomedical application—characteristics of raw measurement data," in *Proceedings of the International Conference on Biomedical Engineering and Biotechnology*, pp. 789–792, IEEE Computer Society, 2012.
- [2] I. Hieda and K. C. Nam, "2D image construction from low resolution response of a new non-invasive measurement for medical application," *ETRI Journal*, vol. 27, no. 4, pp. 385–393, 2005.
- [3] J. G. Webster, Ed., *Electrical Impedance Tomography*, Adam Hilger, New York, NY, USA, 1990.
- [4] S. Grimnes and O. G. Martinsen, *Bioimpedance and Bioelectricity Basics*, Academic Press, London, UK, 2000.
- [5] H. Scharfetter, H. K. Lackner, and J. Rosell, "Magnetic induction tomography: hardware for multi-frequency measurements in biological tissues," *Physiological Measurement*, vol. 22, no. 1, pp. 131–146, 2001.
- [6] A. Korjnevsky, V. Cherepenin, and S. Sapetsky, "Magnetic induction tomography: experimental realization," *Physiological Measurement*, vol. 21, no. 1, pp. 89–94, 2000.
- [7] G. Rogers, L. Brandt, J. Young, and J. Kot, "The Study of diffusion effect in RIM tomographic imaging," *Exploration Geophysics*, vol. 24, pp. 785–788, 1993.
- [8] J. Young, G. Rogers, S. Thomson, and M. Neil, "Australian development of tomographic radio imaging as a new tool in mining geophysics," *Butsuri-Tansa*, vol. 47, pp. 249–255, 1994.
- [9] T. S. Tuykin and A. V. Korjnevsky, "Electric field tomography system with planar electrode array," in *Proceedings of the 13th International Conference on Electrical Bioimpedance and the 8th Conference on Electrical Impedance Tomography*, vol. 17, pp. 201–204, September 2007.
- [10] Y. V. Gulyaev, A. V. Korjnevsky, T. S. Tuykin, and V. A. Cherepenin, "Visualizing electrically conducting media by electric field tomography," *Journal of Communications Technology and Electronics*, vol. 55, no. 9, pp. 1062–1069, 2010.
- [11] M. Bertero, M. Miyakawa, P. Boccacci, F. Conte, K. Orikasa, and M. Furutani, "Image restoration in chirp-pulse microwave CT (CP-MCT)," *IEEE Transactions on Biomedical Engineering*, vol. 47, no. 5, pp. 690–699, 2000.
- [12] J. D. Shea, P. Kosmas, B. D. van Veen, and S. C. Hagness, "Contrast-enhanced microwave imaging of breast tumors: a computational study using 3D realistic numerical phantoms," *Inverse Problems*, vol. 26, Article ID 074009, 2010.
- [13] L. Lizzi, P. Rocca, A. Massa, T. Fujimoto, and T. Takenaka, "Synthesis of a wideband antenna array for microwave imaging applications," in *Proceedings of the 5th European Conference on Antennas and Propagation (EUCAP '11)*, pp. 1938–1941, April 2011.
- [14] K. Suzuki and Y. Kuwahara, "Microwave mammography using multi-static UWB radar," in *Proceedings of the IEEE International Symposium on Antennas and Propagation and USNC/URSI National Radio Science Meeting (APSURSI '09)*, June 2009.
- [15] I. Hieda and K. C. Nam, "FDTD simulation of radio imaging method for biomedical application," in *Proceedings of the 4th Kuala Lumpur International Conference on Biomedical Engineering (Biomed '08)*, pp. 566–569, Springer, Kuala Lumpur, Malaysia, June 2008.
- [16] I. Hieda and K. C. Nam, "Improvement on signal strength detection of radio imaging method for biomedical application," in *Proceedings of the 13th International Conference on Biomedical Engineering (ICBME '08)*, vol. 23, pp. 523–526, Springer, Singapore, 2008.
- [17] I. Hieda and K. C. Nam, "The frequency dependence of the effect of the human body conductivity in the radio imaging method for medical application," in *Proceedings of the 6th World Congress of Biomechanics (WCB '10)*, pp. 1562–1565, Singapore, August 2010.
- [18] A. Taflove and S. C. Hagness, *Computational Electrodynamics, The Finite-Difference Time-Domain Method*, Artech House, London, UK, 2 edition, 2000.
- [19] R. Lytle, "The numeric python EM project," *IEEE Antennas and Propagation Magazine*, vol. 44, no. 6, p. 146, 2002 (Japanese).
- [20] M. Miyakawa, "Noninvasive measurement of temperature profiles inside dielectric materials," *Bulletin of the Electrotechnical Laboratory*, vol. 45, no. 9-10, pp. 419–435, 1981.
- [21] E. Grayver, *Implementing Software Defined Radio*, Springer, New York, NY, USA, 2012.
- [22] I. Hieda and K. C. Nam, "Electric field measurement for biomedical application using GNU radio," in *Proceedings of the 5th Kuala Lumpur International Conference on Biomedical Engineering (BIOMED '11)*, pp. 300–304, June 2011.
- [23] "Ettus research," <http://www.ettus.com/>.
- [24] "GNU radio," <http://gnuradio.org/>.
- [25] I. Hieda and K. C. Nam, "Improvement of the measurement quality of radio imaging method for biomedical application," in *Proceedings of the World Congress on Medical Physics and Biomedical Engineering (WC '09)*, pp. 128–131, Springer, September 2009.
- [26] I. Hieda, K. C. Nam, and A. Takahashi, "Basic characteristics of the radio imaging method for biomedical applications," *Medical Engineering and Physics*, vol. 26, no. 5, pp. 431–437, 2004.
- [27] I. Hieda, "Preliminary study of 2D image construction by radio imaging method (RIM) for medical application," in *Proceedings of the Kuala Lumpur International Conference on Biomedical Engineering (IFMBE '04)*, vol. 7, pp. 91–94, Kuala Lumpur, Malaysia, September 2004.
- [28] K. C. Nam and I. Hieda, "Dielectric measurement using radio imaging method for tomography," in *Proceedings of the 13th International Conference on Electrical Bioimpedance and the 8th Conference on Electrical Impedance Tomography (ICEBI '07)*, pp. 472–475, September 2007.
- [29] T. Yahagi, "A deterministic approach to optimal linear digital equalizers," *IEEE Transactions on Acoustics, Speech, and Signal Processing*, vol. 31, no. 2, pp. 491–500, 1983.
- [30] T. Yahagi, *Theory of Digital Signal Processing 2*, Corona Publishing, Tokyo, Japan, 1985.

Research Article

A Feasibility Study for Microwave Breast Cancer Detection Using Contrast-Agent-Loaded Bacterial Microbots

Yifan Chen,¹ Panagiotis Kosmas,² and Sylvain Martel³

¹ Department of Electrical and Electronic Engineering, South University of Science and Technology of China, Shenzhen 518055, China

² School of Natural and Mathematical Sciences, King's College London, London WC2R 2LS, UK

³ Department of Computer Engineering, Ecole Polytechnique de Montreal, Montreal, Canada H3T 1J4

Correspondence should be addressed to Yifan Chen; chen.yf@sustc.edu.cn

Received 25 June 2013; Accepted 24 September 2013

Academic Editor: Soon Yim Tan

Copyright © 2013 Yifan Chen et al. This is an open access article distributed under the Creative Commons Attribution License, which permits unrestricted use, distribution, and reproduction in any medium, provided the original work is properly cited.

We propose a new approach to microwave breast tumor sensing and diagnosis based on the use of biocompatible flagellated magnetotactic bacteria (MTB) adapted to operate in human microvasculature. It has been verified experimentally by Martel et al. that externally generated magnetic gradients could be applied to guide the MTB along preplanned routes inside the human body, and a nanoload could be attached to these bacterial microbots. Motivated by these useful properties, we suggest loading a nanoscale microwave contrast agent such as carbon nanotubes (CNTs) or ferroelectric nanoparticles (FNPs) onto the MTB in order to modify the dielectric properties of tissues near the agent-loaded bacteria. Subsequently, we propose a novel differential microwave imaging (DMI) technique to track simultaneously multiple swarms of MTB microbots injected into the breast. We also present innovative strategies to detect and localize a breast tissue malignancy and estimate its size via this DMI-trackable bacterial microrobotic system. Finally, we use an anatomically realistic numerical breast phantom as a platform to demonstrate the feasibility of this tumor diagnostic method.

1. Introduction

In recent years, there have been considerable efforts in applying microwave technology for early-stage breast cancer detection [1]. This imaging modality attempts to discriminate breast tissues based on their dielectric properties, which are sensitive to physiological or pathological conditions such as water content, temperature, and vascularization. However, the effectiveness of microwave medical imaging is considerably influenced by clutter interference due to healthy tissue inhomogeneities [2]. This problem can be possibly solved by using a contrast agent such as carbon nanotubes (CNTs) [3] or ferroelectric nanoparticles (FNPs) [4] to change the tumor tissue dielectric values. These agents can be transported selectively to cancer cells via systemic administration for specific and noninvasive diagnosis of tissue malignancies within specified regions-of-interest (ROI). These contrast media can also be employed in medical therapeutic applications such as microwave hyperthermia treatment [3].

However, contrast-enhanced microwave cancer theranostics is compromised by currently available targeting techniques, which have limited efficacy due to intratumoral penetration limitations and the presence of quiescent cells within tumors [5]. As a result, only a small amount of contrast agent is able to enter cancer cells. Recent advance in micro-nano biorobotics has promised a potential remedy for this problem through the prospect of utilizing biocompatible flagellated magnetotactic bacteria (MTB) with nanometer-sized magnetosomes acting like computer-controlled medical microbots. Their swimming directions and displacement speeds can be regulated by an externally applied magnetic field [6, 7] to deliver effectively a nanoload such as contrast agents to a tumoral region in the human body, offering new possibilities for breast cancer detection in microwave tomographic [8] and radar-based [9] approaches. A tactic for MTB-oriented microwave breast cancer detection was suggested in [10], where each time a single swarm of MTB microbots loaded with a nanoscale contrast agent is injected

into the breast from a predefined injection site. The microbots will navigate towards the direction of an externally exerted magnetic gradient and its movement could potentially be tracked by using the differential microwave imaging (DMI) algorithm proposed in [11]. In theory, when a particular microbot trajectory would meet a tumor, the contrast agent will be discharged from the microbots and attached to cancer cell receptors. Subsequently, these miniature biorobots will no longer be trackable by the DMI system, which only detects difference in the tissue dielectric properties caused by the agent. Therefore, a DMI footprint “sink” inside breast would emerge at the tumor location where the contrast agent accumulates eventually.

The current work extends the results in [10] by considering multiple agglomerations of MTB, which are injected concurrently into breast at each round of operation to reduce the diagnostic time. Our previous DMI algorithm [11] is only applicable to the location estimation of the nearest microbot swarm. Consequently, in order to track multiple swarms, the antennas of the DMI apparatus should be divided into several groups. Each group only tracks its nearest swarm. By enforcing the constraint that DMI footprints should be nearly aligned with the *a priori* known magnetic field, the average dielectric properties of breast can be approximated and the microbot swarms are tracked. Furthermore, as a significant extension to [12], we provide a comprehensive discussion on the main characteristics of the MTB as an ideal contrast-agent transporter and propose to deploy them to target possible tumor locations from different angles in order to reduce false alarms and possibly estimate the tumor size via registration of multiple final footprints around the tumor border.

It is worth noting that the proposed technique for detection of tumors is an extrapolation of laboratory-verified techniques and is applied to the problem of breast cancer sensing. The current work represents an early-stage exploration of this approach.

The remainder of the paper is organized as follows. In Section 2, we highlight some key properties of the controllable MTB actuators, which have been demonstrated experimentally by Martel et al. [6, 7]. We also present the general principle of tumor sensing and diagnosis. In Section 3, we describe possible schemes to detect and localize a breast tissue malignancy and estimate its size through the DMI-trackable bacterial propulsion-and-steering platform. In Section 4, we study the feasibility of the proposed strategies using an anatomically realistic breast model from the University of Wisconsin Computational Electromagnetics (UWCEM) Laboratory’s Breast Phantom Repository [13]. Finally, we conclude with discussion on the potential and future extension of our approach in Section 5.

2. Bacterial Microbots for Direct Tumor Targeting

2.1. Main Characteristics of MTB. A flagellated MTB can be considered as a sophisticated cargo carrier with an embedded control interface, which comprises the following components as illustrated in Figure 1: (i) a steering wheel controlling

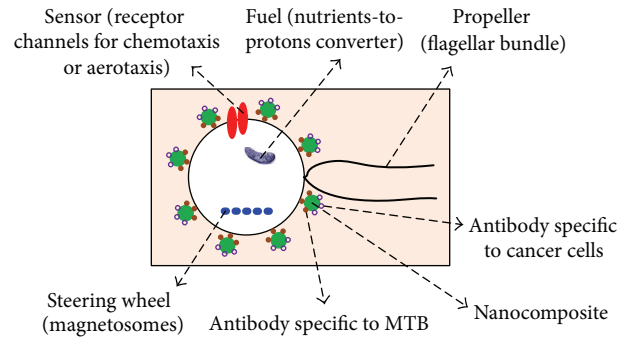


FIGURE 1: Key functional elements of MTB.

remotely the direction in which the MTB move (i.e., a chain of magnetosomes imparting to the MTB a magnetic moment so that the bacterium can align itself to an external magnetic field); (ii) propellers as the propulsion engines accelerating the MTB to move towards a targeted destination (i.e., two flagellar bundles allowing the bacterium to swim in a medium); (iii) a fuel unit powering all the components by scavenging energy from external sources (i.e., a nutrients-to-protons converter); and (iv) sensors acting as the interface between the environment and the MTB (i.e., receptor channels for chemotaxis or aerotaxis to detect nutrient gradients).

As shown in the previous works by Martel et al. [6, 7, 14–17], MTB exhibit the following desirable properties making them ideal controllable bacterial actuators for direct tumor sensing.

2.1.1. Speed and Size. Magnetotactic cocci cells (e.g., the MC-1 bacteria) can achieve an average velocity of $200 \mu\text{m/s}$ in human blood with a peak velocity of $300 \mu\text{m/s}$. This is much faster than many other flagellated bacteria ($30 \mu\text{m/s}$) and the synthetic artificial flagella in the form of nanocoils actuated by a rotating magnetic field ($4.6 \mu\text{m/s}$). The maximum velocity could be maintained even when the MTB were loaded with an average of 70 liposomes with an overall diameter exceeding 150 nm , suggesting the possibility of attaching a wide variety of nanoscale elements to the surface of its cell. The cell of the MC-1 MTB is spherical in shape with a diameter of $\sim 2 \mu\text{m}$ being approximately half the diameter of the smallest capillaries in human, making it ideal for transiting in the tiniest blood vessels.

2.1.2. Propulsion and Steering. The two flagellar bundles of the MC-1 MTB provide a thrust force exceeding 4 pN , which is much higher than other flagellated bacteria ($0.3\text{--}0.5 \text{ pN}$). When subject to a magnetic field higher than 4 Gauss, the directional motions of the MTB were mainly influenced by magnetotaxis (i.e., aligned to magnetic field lines) as compared to chemotaxis (i.e., moving towards or away from a chemical source) and aerotaxis (i.e., moving towards or away from air or oxygen), thus fully remotely controllable using appropriate electronic hardware and software.

2.1.3. Byproducts of Bacterial Degradation. The degradation byproducts of the nonpathogenic bacteria could have

a cytotoxic effect at high concentration, which imposes a limit on the amount of MTB that could be present in the human body at any time. Preliminary results showed that the cell viability was higher than 90% for 80 μL of bacteria solution (5×10^4 cells/200 μL in cell culture solution) in a 200 μL well, indicating the noncytotoxic effect of the bacteria at this concentration.

On the other hand, initial experiments conducted in human blood at 37° showed that the velocity V (in $\mu\text{m/s}$) at a time t (expressed in minutes) after the beginning of operations of the MC-1 MTB decreased according to

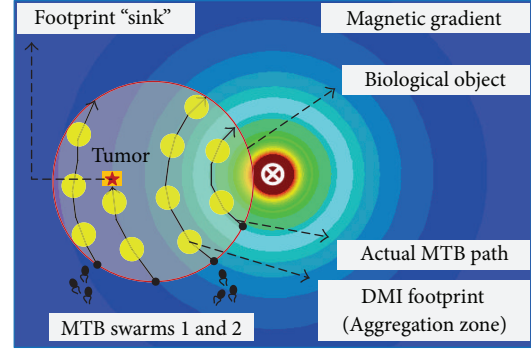
$$V = 0.09t^2 - 8.10t + V_0, \quad 0 \leq t \leq 40 \text{ min}, \quad (1)$$

where $V_0 \approx 200 \mu\text{m/s}$ is the initial average velocity of the MTB prior to being injected into blood. The MC-1 MTB would remain effective for at least 40 minutes, and the decrease in speed was probably caused by the relatively high temperature of blood. This is beneficial from the perspective of biocompatibility and safe *in vivo* operations but limits the time at which the MC-1 MTB could operate. As a rough estimate, the average distance that could be traveled by an effective MC-1 MTB in the human body is given by $\int_0^{40} V \cdot 60dt \approx 21 \text{ cm}$, which is sufficient for the application of breast cancer theranostics.

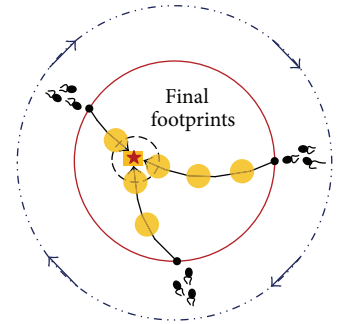
2.1.4. Loading and Targeting. The delivery of a contrast agent to a tumoral lesion requires transitions through capillary sections of human microvasculature. The loading strategy depicted in Figure 1 can utilize antibodies specific to MC-1 cells or another effective method based on chemical bonding (see, e.g., [6]). The nanocomposites such as CNTs or FNPs can be functionalized by means of proper molecular groups such as peptides or antibodies, which are able to bind to cancerous cell receptors.

In order to deliver sufficient amounts of contrast agent to a tumor, a cluster of MC-1 MTB can be deployed simultaneously. It has been demonstrated that an agglomeration of MC-1 cells could be controlled like a unified organism to swim along a predetermined path by an external computer [14]. Finally, it has been shown using an *in vitro* model that MTB guided by magnetic fields could penetrate inside a multicellular tumor spheroid. As many tumors contain vasculogenic mimicry [18], these channels should help MTB to be evenly distributed inside a tumor.

2.1.5. Aggregation of MTB. A relatively weak magnetic gradient could be generated towards an *aggregation zone*, whose size can easily be in the millimeter range. The boundary of the aggregation zone is equivalent to approximately 0.5 Gauss with the center at 0 Gauss. When outside the aggregation zone, the bacteria follow the line of magnetic field. When inside the zone, the MTB are no longer influenced by magnetotaxis and begin random motions. If the MTB exit the aggregation zone, the magnetic field forces the MTB to move back to the zone by magnetotaxis. To improve targeting effectiveness, various magnetic field modulation modes have been developed depending on the characteristics of the



(a)



(b)

FIGURE 2: Illustration of (a) cancer detection and (b) examination with multiswarm MTB microbots.

angiogenesis network, that is, the capillary network feeding the tumor or the surrounding tissue. Once targeting has been completed, imaging could be performed to assess targeting efficacy and to confirm the region being affected. If needed, the operation can be repeated towards another targeted area by setting the aggregation zone accordingly.

2.2. Cancer Detection and Diagnosis with MTB Microbots. We illustrate the rationale for cancer detection and diagnosis with multiswarm MTB microbots in Figure 2(a), where two clumps of MTB are used as an example. Consider that these MTB are loaded with a microwave agent and injected simultaneously into the human body from two separate injection sites. An external source creates a magnetic field by means of a wire or coils placed close to the biological object under examination. As shown in Figure 2(a), we assume that the resulting magnetic field lines are concentric circles, which determine the direction in which the MTB will align. Apart from magnetotaxis, the MTB paths are mainly constrained by microvasculature networks in the breast. Hence, the movement of MTB is not directly affected by the heterogeneity within the breast.

We extend the DMI algorithm proposed in [11] to multiple targets as to be discussed in Section 3.2. This method is then utilized to track the motions of these two agglomerations of microbots by detecting and localizing the change in tissue dielectric properties in the targeted MTB aggregation zones

as illustrated in Figure 2(a). Consequently, the measured DMI footprints corresponding to these aggregation zones result in snapshots of the actual MTB paths as illustrated in Figure 2(a). If a swarm of MTB microbots fails to detect a tumor (i.e., the corresponding microbot path does not cross the tumor), it will keep navigating towards the magnetic gradient until being maneuvered out of the human body. On the other hand, if the swarm senses a tumor, the contrast agent will be removed from the swarm and bound to cancer cell receptors. After load discharging, this swarm will become invisible to the DMI system, which only tracks variation in tissue dielectric properties caused by the agent. Hence, the location where the contrast agent finally accumulates will give rise to a “sink” on the preplanned MTB pathway as shown in Figure 2(a). Multiple tissue malignancies will result in several DMI footprint “sinks.” Hence, tumors can be detected via this *seeing-is-sensing* principle.

On the other hand, we could inject MTB to target a detected and localized tumor from various directions as depicted in Figure 2(b). This can be achieved by using several magnetic field sources using, for example, direct current (dc) sources placed at different locations. These fields would guide MTB along distinct pathways to reach cancer cells from different angles. In this way, the final footprints immediately before a “sink” is observed would be scattered around the tumor edge. The tumor size which is related to the stage of breast cancer can thus be estimated via registration of all the final footmarks as demonstrated in Figure 2(b). This additional information will also help reduce false alarms for possible tumor locations. Hence, a tumor could be examined via this *seeing-is-examination* principle.

In the next section, we present possible strategies for the implementation of these approaches.

3. Strategies for Breast Cancer Detection, Localization, and Size Estimation

3.1. Proposed System Architecture and Protocol. To elaborate on our approaches, we consider a “heterogeneously dense” numerical phantom from the UWCEM breast model repository [13], which also includes one tumor having the median dielectric properties of malignant breast tissue [2]. Similar to [8, 11], we employ the forty-element dipole antenna array arranged over five circular rings as shown in Figure 3(a). We plan to implement two-dimensional (2D) tumor sensing along the cross-sectional planes of the rings using three-dimensional (3D) DMI data. For illustrative purpose, we focus on the third cross-sectional plane from the top, which slices through the tumor. The corresponding dielectric profile is shown in Figure 3(b). We apply the monostatic data obtained at the eight antennas of the third ring for tumor sensing. It is assumed that the presence of a contrast agent in a tissue region will substantially alter its dielectric properties [3]. As outlined in Section 2.2, our aim is to use the DMI algorithm to track the MTB swarms by sensing the induced changes in the surrounding tissue dielectric values. An important side result is the estimation of the breast average properties.

A block diagram representing the system architecture of breast tumor detection and diagnosis with multiswarm MTB microbots is shown in Figure 4. The basic sequence of events is detailed as follows.

3.1.1. Initialization. Prior to the injection of contrast-agent-loaded microbots, we consecutively transmit ultra-wideband (UWB) probing waveforms from each antenna element as shown in Figure 3(b) and record the signals reflected from the breast at each element. These backscatter responses for the agent-free breast will be used for benchmarking during the DMI procedure at a later step.

3.1.2. Propulsion and Steering. We design the in-body microbot routes based on the breast geometry as well as the ROI in its interior and identify the corresponding injection sites on the breast surface. The ROIs may be acquired by using some preprocessing procedures (e.g., a noninvasive tomographic approach). The better the ROIs can be defined, the better the MTB paths can be planned. From this perspective, the system performance also depends on having a good-quality initial-stage imaging system. The path planning should ensure that the entire ROI where cancers may be present is covered with sufficiently small intervals between neighboring paths to reduce the probability of miss. To reduce sensing time, we inject multiple swarms of agent-loaded microbots into the breast. Note that we do not produce the magnetic field in our simulations but assume that its effect is to guide the swarms along concentric magnetic field lines generated at one of the eight antennas for a specific interval t_{ps} until they reach the targeted aggregation zones as illustrated in Figure 3(b). During traveling to the aggregation zone, the microbots are not detected because they swim at different velocities and as such they disperse, making the density too low for tracking.

3.1.3. Tracking. Subsequently, we switch the system operational mode from “propulsion-and-steering” to “tracking.” In order to set two aggregation zones simultaneously, we employ the following time-multiplexing scheme at a high frequency: $T_{\mathcal{M}_1} \rightarrow T_{\mathcal{M}_2} \rightarrow T_{\mathcal{A}_1} \rightarrow T_{\mathcal{M}_1} \rightarrow T_{\mathcal{M}_2} \rightarrow T_{\mathcal{A}_2} \rightarrow \dots$. During $T_{\mathcal{M}_1}$ and $T_{\mathcal{M}_2}$, two magnetic gradients are generated to set the two aggregation zones. Furthermore, during $T_{\mathcal{A}_i}$ ($i = 1, 2, \dots, 8$), the waveform used in the initialization phase is retransmitted from the i th antenna element, and the corresponding backscatter response is recorded. We then apply the DMI algorithm to track multiple swarms within their respective aggregation zones. The size of the aggregation zones is in the range of 2 mm, which is much smaller than the cancerous lesion to be detected.

3.1.4. Decisionmaking. We then confirm whether the tumor sensing is completed, given the microbot footmarks and subject to a number of criteria as listed in Figure 4. We need to check whether the swarms of microbots are still present in the breast, whether a DMI footprint “sink” has been observed, and whether all the preplanned paths have been completed. If all the answers are confirmative, we declare that tissue anomalies have been positively detected. Otherwise,

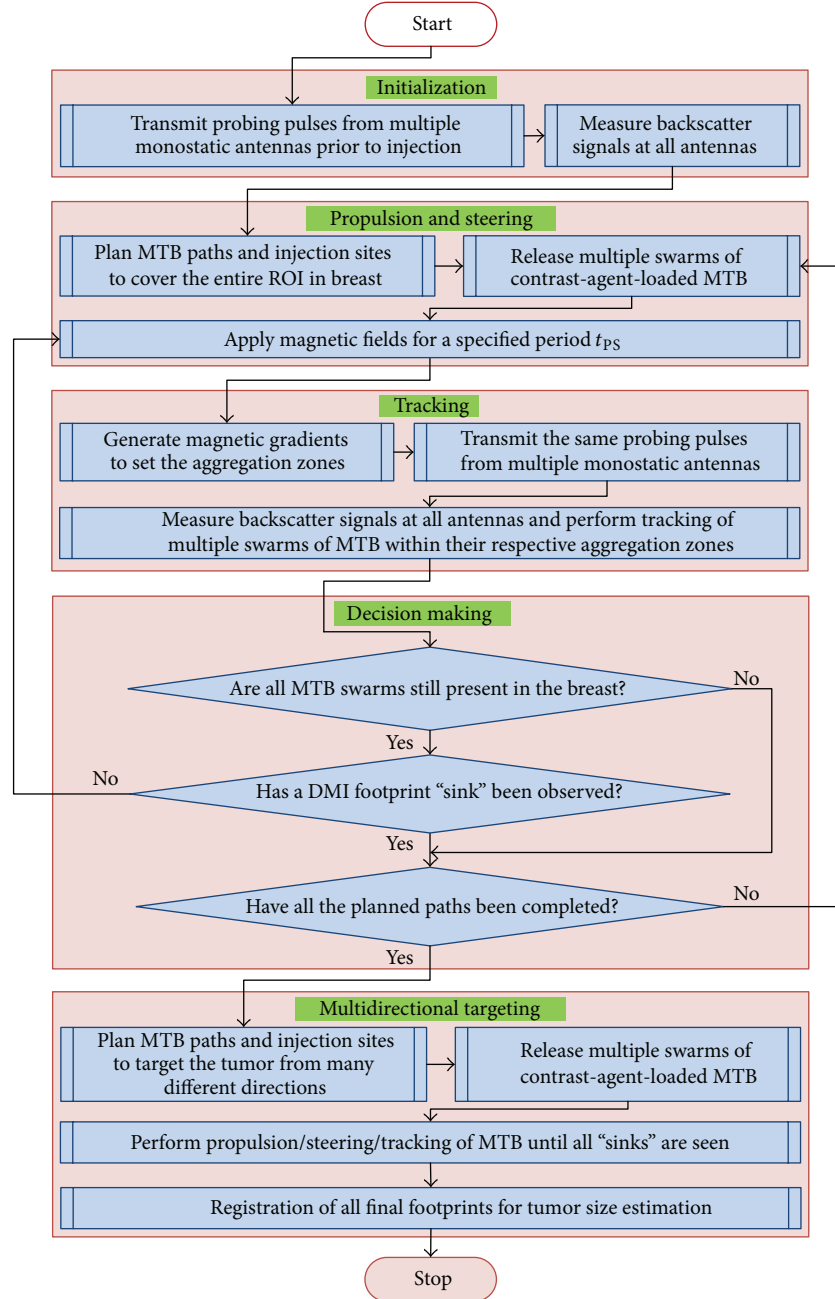


FIGURE 4: Flowchart representing the system architecture of breast tumor detection and diagnosis with multiswarm MTB microbots.

This additional step also helps reduce false alarms for tumor detection and localization by exploiting the microbot path diversity.

3.2. Tracking of Multiple Swarms of MTB Microbots. In this section, we present a novel DMI algorithm to detect multiple local dielectric variations due to multiswarm contrast-agent-loaded MTB microbots. We can summarize the principles of the algorithm as follows. A microwave contrast agent such as CNTs or FNP loaded onto multiple aggregations of MTB changes the local dielectric properties of the tissue regions where the MTB are present. We can extract

the difference between the backscatter responses before and after the injection of MTB over time. We then formulate the problem from the perspective of signal model selection (differential signal corrupted by noise versus noise alone) and apply the information theoretic criterion such as the Akaike information criterion or the minimum description length to reliably estimate the locations of the induced dielectric changes [11].

We consider a cluttered breast medium as shown in Figure 5. Two swarms of MTB microbots are present in the interference-prone biological environment with a large number of normal breast tissue inhomogeneities. Consider

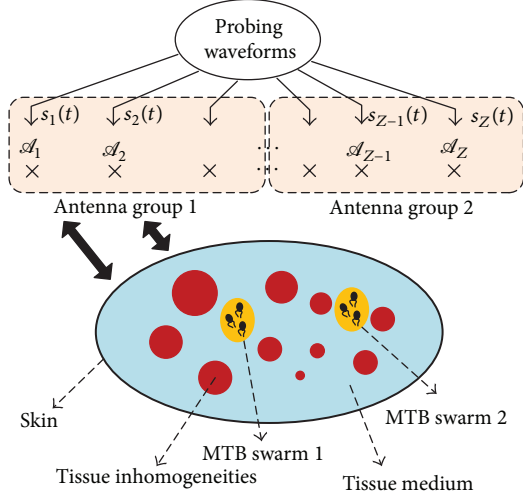


FIGURE 5: An interference-prone breast channel where two agent-loaded MTB swarms are present in the cluttered breast with tissue inhomogeneities. A radar system containing multiple spatially diverse monostatic antenna elements is deployed for tracking the swarms.

a radar system comprising multiple monostatic antenna elements, $\mathcal{A}_1, \mathcal{A}_2, \dots, \mathcal{A}_Z$. Each antenna represents both a source and a sensor of the electromagnetic signals. We will use the subscript z in all the following analyses to indicate the quantities associated with antenna \mathcal{A}_z ($z = 1, 2, \dots, Z$). Let $s_z(\cdot)$ and $o_z(\cdot)$ denote, respectively, the discrete-time transmitted and received signals by \mathcal{A}_z . The following general relationship can be obtained:

$$o_z(m) = \sum_{l=0}^{L_z-1} h_z(l) s_z(m-l) + u_z(m), \quad (2)$$

where $h_z(\cdot)$ is the discrete channel response, $u_z(\cdot)$ is the additive white Gaussian noise (AWGN), and L_z denotes the order of the discrete channel. Equation (2) can be rewritten in the matrix form as

$$\mathbf{o}_z = \mathbf{H}_z \mathbf{s}_z + \mathbf{u}_z, \quad (3)$$

where

$$\mathbf{o}_z = [o_z((n-1)(L_z + M_z - 1) + 1) \cdots o_z(n(L_z + M_z - 1))]^T,$$

$$\mathbf{H}_z = \begin{bmatrix} & & & h_z(0) \\ & & h_z(0) & h_z(1) \\ & \vdots & \vdots & \vdots \\ h_z(0) & h_z(1) & \cdots & h_z(M_z - 1) \\ h_z(1) & h_z(2) & \cdots & h_z(M_z) \\ \vdots & \vdots & \vdots & \vdots \\ h_z(L_z - 2) & h_z(L_z - 1) & & \end{bmatrix},$$

$$\mathbf{s}_z = [s_z(nM_z) \cdots s_z((n-1)M_z + 1)]^T,$$

$$\mathbf{u}_z = [u_z((n-1)(L_z + M_z - 1) + 1) \cdots u_z(n(L_z + M_z - 1))]^T. \quad (4)$$

In (4), $n = 1, 2, \dots, N$ is the index of each observation. \mathbf{o}_z , \mathbf{H}_z , \mathbf{s}_z , and \mathbf{u}_z are the $(L_z + M_z - 1) \times 1$ observation vector, the $(L_z + M_z - 1) \times M_z$ channel matrix, the $M_z \times 1$ source signal vector, and the $(L_z + M_z - 1) \times 1$ noise vector, respectively. The symbol T denotes matrix transpose.

Suppose that the delay taps introduced by these two swarms of agent-attached microbots are $\ell_{1,z}$ and $\ell_{2,z}$ ($0 < \ell_{1,z}, \ell_{2,z} \leq L_z - 1$). The presence of contrast media in the breast will distort the biological channel response by inducing changes in the tissue dielectric properties. We note that only late responses with delays greater than $\mathcal{L}_z = \min\{\ell_{1,z}, \ell_{2,z}\}$ will be affected. Hence, the new channel matrix after injection of MTB is

$$\tilde{\mathbf{H}}_z = \mathbf{H}_z + \Delta \mathbf{H}_z, \quad (5)$$

where the (i, j) th ($i = 1, 2, \dots, L_z + M_z - 1$; $j = 1, 2, \dots, M_z$) entry of the perturbation matrix $\Delta \mathbf{H}_z$ is expressed as

$$\Delta \mathbf{H}_z [i, j] = \begin{cases} 0; & \text{if } \mathbf{H}_z [i, j] = 0 \\ 0; & \text{if } \mathbf{H}_z [i, j] = h_z(l) \text{ and } l < \mathcal{L}_z \\ \Delta h_z(l); & \text{if } \mathbf{H}_z [i, j] = h_z(l) \text{ and } l \geq \mathcal{L}_z. \end{cases} \quad (6)$$

In (6), $\Delta h_z(l)$ is a nonzero term summarizing the overall perturbation effect introduced to the l th tap of the biological channel.

Subsequently, we can split all antennas into two groups as shown in Figure 5. For each member in antenna group k ($k = 1, 2$), $\mathcal{L}_z = \ell_{k,z}$, and each group only detects its nearest microbot swarm. As a result, we can apply readily the information-theoretic-criteria-based DMI algorithm in [11] for single-target localization, where the time-of-arrival (TOA) of the backscatter from the swarm, \mathcal{L}_z , is estimated. If the microbot paths are planned such that the two swarms are well separated in the breast at all time instants, it is straightforward to perform antenna grouping, knowing the locations of the injection sites and the dc source.

3.3. TOA Data Fusion for Unknown Average Tissue Dielectric Properties. To estimate the cancer location, the TOAs measured at different antennas can be combined by using the data fusion method proposed in [19]. This algorithm, however, requires knowledge about the average tissue dielectric properties, which is very difficult to obtain in a real-life clinical setting. The current tumor sensing strategy offers an interesting way to overcome the above challenge by estimating both the average wave propagation speed and the swarm location in the breast. We assume that an antenna \mathcal{A}_{z_k} ($k = 1, 2$) is tracking the k th microbot swarm. \mathcal{A}_{z_k} is located at (x_{z_k}, y_{z_k}) and measures a TOA $\tau_{z_k} = \mathcal{L}_{z_k} T_0$, where T_0 is the sampling time. The TOA τ_{z_k} defines a circle centered at \mathcal{A}_{z_k} with radius $r_{z_k} = v\tau_{z_k}/2$, where v is the average speed of electromagnetic waves in the breast medium and is related to

the mean tissue permittivity ε_b and conductivity σ_b through the following relationship:

$$v = \frac{1}{\sqrt{(\mu_0 \varepsilon_b / 2) \left[\sqrt{1 + (\sigma_b / \omega \varepsilon_b)^2} + 1 \right]}}. \quad (7)$$

As knowledge of the TOA estimation error statistics is not available, we locate the k th microbot swarm by minimizing the sum of square of the distances from the swarm to the points of intersection of the range circles closest to it. The objective function is given by

$$\hat{\mathbf{x}}_k = \arg \min_{\mathbf{x}_k} \left\{ \sum_{j_k=1}^{J_k} \|\mathbf{x}_k - \bar{\mathbf{x}}_{j_k}\|^2 \right\}. \quad (8)$$

The parameter J_k is the total number of intersection points. $\mathbf{x}_k = [\mathbf{x}_{k,0}^T, \delta_1, \dots, \delta_{Z_k}]^T$, where $\mathbf{x}_{k,0} = [x_k, y_k]^T$ is the true position of the k th swarm, δ_{z_k} represents the value of distance measurement error between \mathcal{A}_{z_k} and the swarm, and Z_k is the cardinality of antenna group k . $\bar{\mathbf{x}}_{j_k} = [\bar{\mathbf{x}}_{0,j_k}^T, 0, \dots, 0]^T$, where $\bar{\mathbf{x}}_{0,j_k} = [\bar{x}_{j_k}, \bar{y}_{j_k}]^T$ is the j_k th intersection.

Let $\mathbf{c}_k = (1/J_k) \sum_{j_k=1}^{J_k} \bar{\mathbf{x}}_{0,j_k}$ be the center of all intersection points, and let $d_{z_k}(\mathbf{c}_k) = \sqrt{(x_{z_k} - x_{c_k})^2 + (y_{z_k} - y_{c_k})^2}$ be the distance between \mathcal{A}_{z_k} and $\mathbf{c}_k = [x_{c_k}, y_{c_k}]^T$. Given an average speed of waves v , an optimum noniterative solution of (8) can be written as [19]

$$\hat{\mathbf{x}}_k(v) = \mathbf{\Omega}_k^T (\mathbf{\Omega}_k \mathbf{\Omega}_k^T)^{-1} (\mathbf{r}_k - \mathbf{d}_k) + \frac{1}{J_k} \sum_{j_k=1}^{J_k} \bar{\mathbf{x}}_{j_k}, \quad (9)$$

where

$$(i) \mathbf{\Omega}_k = \begin{bmatrix} (x_{c_k} - x_1)/d_1(\mathbf{c}_k) & (y_{c_k} - y_1)/d_1(\mathbf{c}_k) & 1 & \dots & 0 \\ \vdots & \vdots & \vdots & \ddots & \vdots \\ (x_{c_k} - x_{Z_k})/d_{Z_k}(\mathbf{c}_k) & (y_{c_k} - y_{Z_k})/d_{Z_k}(\mathbf{c}_k) & 0 & \dots & 1 \end{bmatrix},$$

(ii) $\mathbf{r}_k = [r_1, \dots, r_{Z_k}]^T$ is the range measurements vector; and

(iii) $\mathbf{d}_k = [d_1(\mathbf{c}_k), \dots, d_{Z_k}(\mathbf{c}_k)]^T$ is the distance vector.

The detailed derivation of (9) can be found in [20].

Finally, we enforce the constraint that DMI footprints should be roughly aligned with the theoretical circular magnetic field with radius R generated by a dc source located at $\mathbf{x}_{dc} = [x_{dc}, y_{dc}]^T$. As a result, the average speed v is estimated to be

$$v^* = \arg \min_v \left\| \|\hat{\mathbf{x}}_k(v) - \mathbf{x}_{dc}\| - R \right\| \quad (10)$$

and the corresponding swarm footprint is given by $\hat{\mathbf{x}}_k(v^*)$.

4. Simulation Results

We use several numerical examples to elaborate on the aforementioned cancer detection and diagnosis methods. Specifically, we simulate possible movements of the swarms due to

the presumed magnetic field and test the ability of the DMI algorithm for tracking the microbot trajectories and sensing the tumor. Figure 3 provides the layout of the microbots-assisted diagnostic system as discussed in Section 3. The injection sites are spaced on the circumference of the cross-section of the numerical phantom shown in Figure 3(b), which is also illustrated in Figure 6(a) (marked with circles). Figure 6(a) also shows the preplanned microbot paths covering uniformly the two ROIs in the breast interior. The gap between two neighboring pathways is ~ 5 mm, which gives rise to the resolution of the specific survey plan. Two microbot swarms are injected into the breast simultaneously, where their injection sites are spaced apart during the whole sensing process to ensure reliable tracking as discussed in Section 3.2. We assume that each swarm of microbots follows a directional random walk during the propulsion-and-steering stage. Thus, each step size fluctuates according to an exponential probability density function (pdf) with a mean value β . Furthermore, the direction at each step is uniformly distributed between $[\varphi - \theta, \varphi + \theta]$. The parameter φ is the average direction towards the magnetic gradient and θ characterizes the effect of directional disturbance due to other gradients such as chemotaxis and aerotaxis as well as random microvasculature structures. Finally, we assume that the microbots in the aggregation zones follow an isotropic random walk with the same step size distribution as the one used in the tracking stage, which has been demonstrated experimentally [6, 7, 14–17].

The initial velocities of both swarms are assumed to be $200 \mu\text{m/s}$, which decrease with time after being injected into the breast according to (1). The duration for the propulsion-and-steering phase is $t_{PS} = 2$ min. To synthesize the effect of contrast-agent-loaded microbots on the tissue dielectric properties, we adopt CNTs as the agent to modify the dielectric properties for one $2 \times 2 \times 2 \text{ mm}^3$ cubic voxel inside the breast phantom. We assume that the relative permittivity and conductivity of this voxel are 22% and 70% higher than the median properties of malignant breast tissue, following the measurement data in [8].

Each dipole antenna in Figure 6(a) is driven with a modulated Gaussian pulse having a bandwidth covering 0.5 to 3.5 GHz, and the backscatter signal is recorded at the same antenna (monostatic configuration). The signal-to-noise ratio (SNR) used in our simulation study is 10 dB.

Figure 6(b) shows a typical simulated sensing process ($\theta = 30^\circ$, $\beta = 100 \mu\text{m}$) and plots the associated DMI footprints. Samples of the exact locations of microbots during the tracking phase are marked with triangles, and the corresponding location estimates are marked with squares. For example, consider two swarms injected simultaneously from the 1st and the 4th injection sites. These two agglomerations of microbots were directed by the magnetic fields to swim for 2 min and reach the first aggregation zones where the tracking was performed. Once the tracking is completed, the system mode was switched back to propulsion-and-steering. The swarms continued navigating and the DMI algorithm presented in Section 3.2 was applied to locate the microbots for the earlier tracking cycle. The same steps were repeated

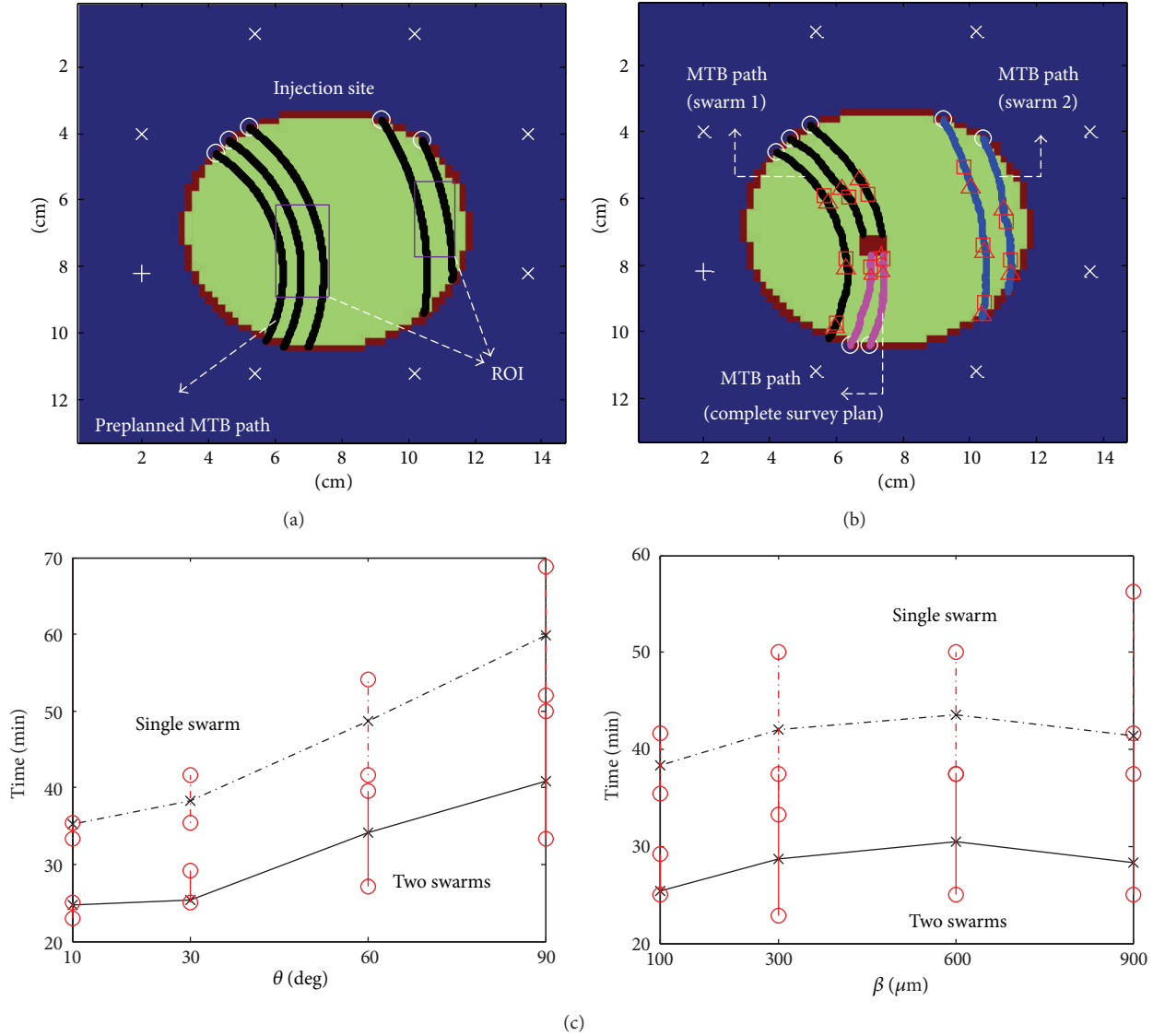


FIGURE 6: (a) Preplanned MTB paths for the system setup in Figure 3(b). (b) Simulated DMI footprints. The MTB injection sites are marked with “o.” The actual and estimated positions of the MTB during the tracking phase are marked with “ Δ ” and “ \square ,” respectively. The estimated final destination of contrast agent (i.e., DMI footprint “sink”) is marked with “ \star .” (c) Sensing time versus angular spread θ and mean step size β of the directional random walk for single- and two-swarm administration. The fixed parameter values are $\beta = 100 \mu\text{m}$ in the former and $\theta = 30^\circ$ in the latter. The markers “x” and “o” correspond to the sensing time mean and dispersion, respectively.

periodically. When any of the two swarms left the breast, we injected a new agglomeration of microbots from the next injection site, and so on. The overall good agreement between the estimated and exact microbot locations demonstrates the feasibility of the proposed DMI algorithm for tracking the CNTs-loaded MTB microbots. Ideally, a DMI footprint “sink” indicating the cancer location will be recorded, as described in Section 3. Finally, two additional microbot injections at the bottom of the breast are required to complete the original path plan shown in Figure 6(a).

The angular spread θ and the mean step size β of the random walk process will affect the cancer diagnostic time, which is an important system performance metric. Figure 6(c) shows the mean, maximum, and minimum tumor

sensing times for various θ and β by carrying out ten independent simulations of the microbot tracking process. Apparently, by exploiting two swarms of microbots in parallel, remarkable reduction in the time spent in completing the breast examination is achieved as compared to the single-swarm case. Moreover, the mean and dispersion of the sensing time increase with the angular spread θ , while the average sensing duration is not affected by different β values though its dispersion increases with β in general.

Finally, Figure 7(a) illustrates a typical multidirectional tumor targeting process based on the strategy presented in Section 3.1. For each dc source, only one injection site is designated in order to send an MTB swarm to target the tumor location from one particular direction. We also reduce

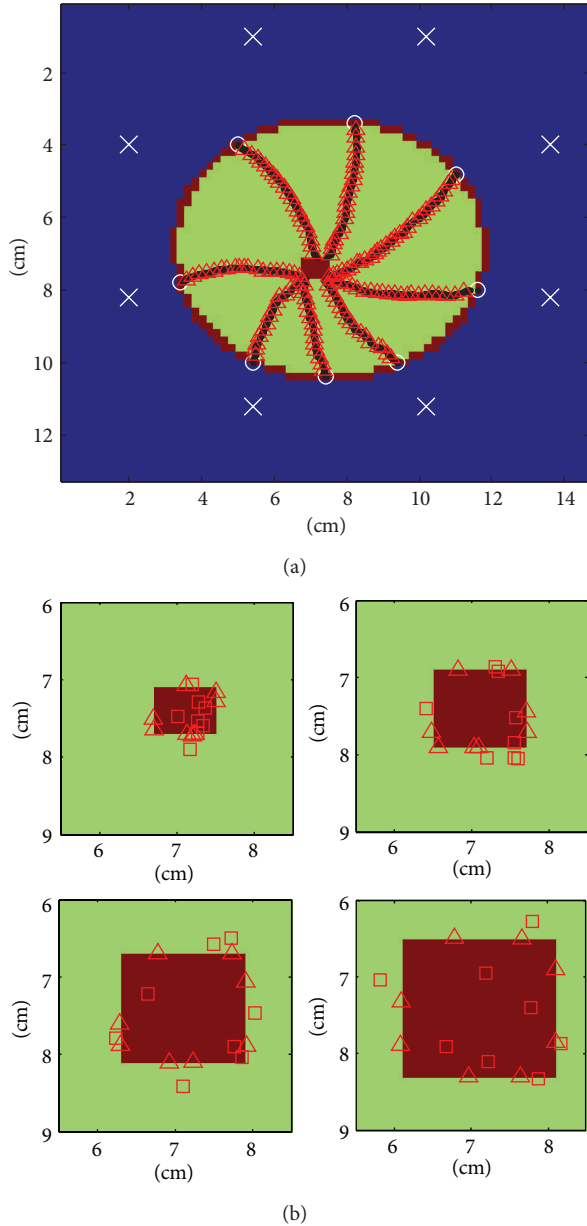


FIGURE 7: (a) Multidirectional tumor targeting. (b) Simulated DMI footprints for four tumors with different sizes. The actual and estimated final MTB footprints are marked with “ Δ ” and “ \square ”, respectively.

the propulsion-and-steering period to 10 s to ensure a more frequent tracking process. Subsequently, Figure 7(b) demonstrates the final footprints of MTB swarms for four tumors with varying sizes. As can be seen from this figure, the locations of these footprints correlate well with the size of the tumor, which demonstrates the potential of the proposed method for tumor size estimation.

5. Conclusion

This preliminary study presented a novel scheme for microwave breast cancer detection and diagnosis with the use of

multiswarm bacterial microbots. The proposed technique is more accurate and is inherently integrated with the follow-up drug delivery and cancer treatment as compared to other noninvasive imaging modalities such as X-ray, magnetic resonance imaging (MRI), ultrasound scan, and microwave imaging. However, it is minimally invasive due to the injection procedure of MTB. Moreover, compared to MRI-guided tumor targeting based on MTB [14], the current approach is much cheaper by replacing the expensive MRI equipment with the low-cost microwave system.

Several key assumptions must be verified for these tactics to be clinically feasible. Firstly, the efficiency of the MTB as controlled trackable propulsion and steering systems, as well as the ability of our proposed DMI algorithm to detect the microbot swarms based on the effect of their contrast agent cargos inside the tissue should be confirmed. The complex permittivity change due to the agent-attached swarms will depend on many factors and must be studied further; the key issue for the feasibility of our approach is that they induce a change in the dielectric properties which can be detected by our DMI technique. Secondly, due to the physiological environment (microvasculature, tissue environment, etc.), it is more likely that the maximum density of microbots in the aggregation zone will be lower than the one achieved in free space such as in water. As such, the sensitivity of the DMI system for tracking microbots in the aggregation zone should be validated experimentally. Finally, the immune response of MTB will be investigated further (e.g., development of mutation of the same specie of MTB for repeated operation within a short duration).

There are many ways for improving and expanding the capabilities of the proposed system. For example, to better plan the swarm trajectories and ensure a good coverage of the breast interior, *a priori* information could be used from a preprocessing step of microwave tomography using the same configuration. In addition, further postprocessing using the differential backscatter data could infer additional information about the lesion morphology and avoid false detection [9], which could occur, for example, if the agent is falsely unloaded. Multimodality imaging including MRI will also be considered. Finally, microwave hyperthermia treatment could be performed once the tissue malignancy is localized and the contrast agent is successfully transported to the tumor site thereby improving its heating response [3].

Conflict of Interests

The authors declare that there is no conflict of interests regarding the publication of this paper.

Acknowledgment

This research was partly supported by 2013 Guangdong Natural Science Funds for Distinguished Young Scholar (Project ID: S2013050014223).

References

- [1] N. K. Nikolova, “Microwave imaging for breast cancer,” *IEEE Microwave Magazine*, vol. 12, no. 7, pp. 78–94, 2011.

- [2] M. Lazebnik, D. Popovic, L. McCartney et al., "A large-scale study of the ultrawideband microwave dielectric properties of normal, benign and malignant breast tissues obtained from cancer surgeries," *Physics in Medicine and Biology*, vol. 52, no. 20, pp. 6093–6115, 2007.
- [3] A. Mashal, B. Sitharaman, X. Li et al., "Toward carbon-nanotube-based theranostic agents for microwave detection and treatment of breast cancer: enhanced dielectric and heating response of tissue-mimicking materials," *IEEE Transactions on Biomedical Engineering*, vol. 57, no. 8, pp. 1831–1834, 2010.
- [4] S. Semenov, N. Pham, and S. Egot-Lemaire, "Ferroelectric nanoparticles for contrast enhancement microwave tomography: feasibility assessment for detection of lung cancer," in *Proceedings of the World Congress on Medical Physics and Biomedical Engineering*, pp. 311–313, Munich, Germany, September 2009.
- [5] A. I. Minchinton and I. F. Tannock, "Drug penetration in solid tumours," *Nature Reviews Cancer*, vol. 6, pp. 583–592, 2006.
- [6] S. Martel, M. Mohammadi, O. Felfoul, Z. L. Zhao Lu, and P. Pouponneau, "Flagellated magnetotactic bacteria as controlled MRI-trackable propulsion and steering systems for medical nanorobots operating in the human microvasculature," *International Journal of Robotics Research*, vol. 28, no. 4, pp. 571–582, 2009.
- [7] N. Mokrani, O. Felfoul, F. A. Zarreh et al., "Magnetotactic bacteria penetration into multicellular tumor spheroids for targeted therapy," in *Proceedings of the 32nd Annual International Conference of the IEEE Engineering in Medicine and Biology Society (EMBC '10)*, pp. 4371–4374, Buenos Aires, Argentina, September 2010.
- [8] J. D. Shea, P. Kosmas et al., "Contrast-enhanced microwave imaging of breast tumors: a computational study using 3D realistic numerical phantoms," *Inverse Problems*, vol. 26, Article ID 074009, 2010.
- [9] Y. Chen, I. J. Craddock, and P. Kosmas, "Feasibility study of lesion classification via contrast-agent-aided UWB breast imaging," *IEEE Transactions on Biomedical Engineering*, vol. 57, no. 5, pp. 1003–1007, 2010.
- [10] P. Kosmas and Y. Chen, "Possibilities for microwave breast tumor sensing via contrast-agent-loaded nanorobots," in *Proceedings of the 6th European Conference on Antennas and Propagation (EUCAP '12)*, Prague, Czech Republic, March 2012.
- [11] Y. Chen and P. Kosmas, "Detection and localization of tissue malignancy using contrast-enhanced microwave imaging: exploring information theoretic criteria," *IEEE Transactions on Biomedical Engineering*, vol. 59, no. 3, pp. 766–776, 2012.
- [12] Y. Chen and P. Kosmas, "Microwave breast tumor sensing and targeting using multiswarm contrast-agent-loaded bacterial nanorobots," in *Proceedings of the International Conference on Electromagnetics in Advanced Applications (ICEAA '12)*, Cape Town, South Africa, September 2012.
- [13] E. Zastrow, S. K. Davis, M. Lazebnik, F. Kelcz, B. D. Van Veen, and S. C. Hagness, "Development of anatomically realistic numerical breast phantoms with accurate dielectric properties for modeling microwave interactions with the human breast," *IEEE Transactions on Biomedical Engineering*, vol. 55, pp. 2792–2800, 2008.
- [14] S. Martel, O. Felfoul, J.-B. Mathieu et al., "MRI-based medical nanorobotic platform for the control of magnetic nanoparticles and flagellated bacteria for target interventions in human capillaries," *International Journal of Robotics Research*, vol. 28, no. 9, pp. 1169–1182, 2009.
- [15] S. Martel, O. Felfoul, M. Mohammadi, and J. B. Mathieu, "Interventional procedure based on nanorobots propelled and steered by flagellated magnetotactic bacteria for direct targeting of tumors in the human body (IEEE EMBC '08)," in *Proceedings of the Annual International Conference of the IEEE Engineering in Medicine and Biology Society*, Vancouver, Canada, August 2008.
- [16] S. Martel, O. Felfoul, and M. Mohammadi, "Flagellated bacterial nanorobots for medical interventions in the human body," in *Proceedings of the 2nd Biennial IEEE/RAS-EMBS International Conference on Biomedical Robotics and Biomechanics (BioRob '08)*, pp. 264–269, October 2008.
- [17] C. C. Tremblay, J. Jean, L. Marchand et al., "Robotic platform for real-time tracking of a single fast swimming bacterium," in *Proceedings of the International Symposium on Optomechatronic Technologies (ISOT '10)*, Toronto, Canada, October 2010.
- [18] R. Folberg, M. J. C. Hendrix, and A. J. Maniotis, "Vasculogenic mimicry and tumor angiogenesis," *The American Journal of Pathology*, vol. 156, no. 2, pp. 361–381, 2000.
- [19] Y. Chen, E. Gunawan, K. S. Low, S.-C. Wang, C. B. Soh, and L. L. Thi, "Time of arrival data fusion method for two-dimensional ultrawideband breast cancer detection," *IEEE Transactions on Antennas and Propagation*, vol. 55, no. 10, pp. 2852–2865, 2007.
- [20] W. Wei, X. Jin-Yu, and Z. Zhong-Liang, "A new NLOS error mitigation algorithm in location estimation," *IEEE Transactions on Vehicular Technology*, vol. 54, no. 6, pp. 2048–2053, 2005.